Film thickness build-up in highly loaded lubricated contacts under Zero Entrainment Velocity condition

Bilel Meziane

N°d'ordre NNT : 2020LYSEI005

THESE de DOCTORAT DE L'UNIVERSITE DE LYON
opérée au sein de
l'INSA Lyon

Ecole Doctorale N° 162
Mécanique, Energétique, Génie civil, Acoustique (MEGA)

Spécialité/discipline de doctorat :
Génie Mécanique

Soutenue publiquement le 06/02/2020, par :
Bilel Meziane

Film thickness build-up in highly loaded lubricated contacts under Zero Entrainment Velocity condition

---

Devant le jury composé de :

Seemann, Wolfgang	Professeur/Karlsruhe Institute of Technology	Rapporteur
Brunetière, Noël	DR CNRS/Université de Poitiers	Rapporteur
Morales-Espejel, Guillermo	Principal Scientist-HdR/SKF	Examinateur
Cayer-Barrioz, Juliette	DR CNRS/École Centrale de Lyon	Examinatrice
Raisin, Jonathan	Docteur/Total	Examinateur
Fillot, Nicolas	Maître de Conférences-HdR/INSA Lyon	Directeur de thèse

Département FEDORA – INSA Lyon - Ecoles Doctorales – Quinquennal 2016-2020

SIGLE	ECOLE DOCTORALE	NOM ET COORDONNEES DU RESPONSABLE
CHIMIE	**CHIMIE DE LYON** http://www.edchimie-lyon.fr Sec. : Renée EL MELHEM Bât. Blaise PASCAL, 3e étage secretariat@edchimie-lyon.fr INSA : R. GOURDON	M. Stéphane DANIELE Institut de recherches sur la catalyse et l'environnement de Lyon IRCELYON-UMR 5256 Équipe CDFA 2 Avenue Albert EINSTEIN 69 626 Villeurbanne CEDEX directeur@edchimie-lyon.fr
E.E.A.	**ÉLECTRONIQUE, ÉLECTROTECHNIQUE, AUTOMATIQUE** http://edeea.ec-lyon.fr Sec. : M.C. HAVGOUDOUKIAN ecole-doctorale.eea@ec-lyon.fr	M. Gérard SCORLETTI École Centrale de Lyon 36 Avenue Guy DE COLLONGUE 69 134 Écully Tél : 04.72.18.60.97 Fax 04.78.43.37.17 gerard.scorletti@ec-lyon.fr
E2M2	**ÉVOLUTION, ÉCOSYSTÈME, MICROBIOLOGIE, MODÉLISATION** http://e2m2.universite-lyon.fr Sec. : Sylvie ROBERJOT Bât. Atrium, UCB Lyon 1 Tél : 04.72.44.83.62 INSA : H. CHARLES secretariat.e2m2@univ-lyon1.fr	M. Philippe NORMAND UMR 5557 Lab. d'Ecologie Microbienne Université Claude Bernard Lyon 1 Bâtiment Mendel 43, boulevard du 11 Novembre 1918 69 622 Villeurbanne CEDEX philippe.normand@univ-lyon1.fr
EDISS	**INTERDISCIPLINAIRE SCIENCES-SANTÉ** http://www.ediss-lyon.fr Sec. : Sylvie ROBERJOT Bât. Atrium, UCB Lyon 1 Tél : 04.72.44.83.62 INSA : M. LAGARDE secretariat.ediss@univ-lyon1.fr	Mme Emmanuelle CANET-SOULAS INSERM U1060, CarMeN lab, Univ. Lyon 1 Bâtiment IMBL 11 Avenue Jean CAPELLE INSA de Lyon 69 621 Villeurbanne Tél : 04.72.68.49.09 Fax : 04.72.68.49.16 emmanuelle.canet@univ-lyon1.fr
INFOMATHS	**INFORMATIQUE ET MATHÉMATIQUES** http://edinfomaths.universite-lyon.fr Sec. : Renée EL MELHEM Bât. Blaise PASCAL, 3e étage Tél : 04.72.43.80.46 infomaths@univ-lyon1.fr	M. Luca ZAMBONI Bât. Braconnier 43 Boulevard du 11 novembre 1918 69 622 Villeurbanne CEDEX Tél : 04.26.23.45.52 zamboni@maths.univ-lyon1.fr
Matériaux	**MATÉRIAUX DE LYON** http://ed34.universite-lyon.fr Sec. : Stéphanie CAUVIN Tél : 04.72.43.71.70 Bât. Direction ed.materiaux@insa-lyon.fr	M. Jean-Yves BUFFIÈRE INSA de Lyon MATEIS - Bât. Saint-Exupéry 7 Avenue Jean CAPELLE 69 621 Villeurbanne CEDEX Tél : 04.72.43.71.70 Fax : 04.72.43.85.28 jean-yves.buffiere@insa-lyon.fr
MEGA	**MÉCANIQUE, ÉNERGÉTIQUE, GÉNIE CIVIL, ACOUSTIQUE** http://edmega.universite-lyon.fr Sec. : Stéphanie CAUVIN Tél : 04.72.43.71.70 Bât. Direction mega@insa-lyon.fr	M. Jocelyn BONJOUR INSA de Lyon Laboratoire CETHIL Bâtiment Sadi-Carnot 9, rue de la Physique 69 621 Villeurbanne CEDEX jocelyn.bonjour@insa-lyon.fr
ScSo	**ScSo*** http://ed483.univ-lyon2.fr Sec. : Véronique GUICHARD INSA : J.Y. TOUSSAINT Tél : 04.78.69.72.76 veronique.cervantes@univ-lyon2.fr	M. Christian MONTES Université Lyon 2 86 Rue Pasteur 69 365 Lyon CEDEX 07 christian.montes@univ-lyon2.fr

*ScSo : Histoire, Géographie, Aménagement, Urbanisme, Archéologie, Science politique, Sociologie, Anthropologie

Résumé

Génération d'épaisseurs de films dans les contacts lubrifiés hautement chargés soumis à une condition de Vitesse d'Entrainement Nulle

Les contacts lubrifiés sous forte charge sont souvent étudiés dans des conditions de roulement/glissement. Dans ces cas, l'entrainement du lubrifiant dans un coin d'huile explique la présence d'un film séparateur. Cependant, il existe un certain nombre d'applications dans lesquelles les surfaces en contact ont des vitesses égales et opposées. Cela correspond à une vitesse d'entrainement (définie comme la moyenne des vitesses des deux surfaces) nulle. Dans ce cas, les modèles prédictifs de la littérature ne peuvent plus s'appliquer. Dans ce mémoire de thèse, les phénomènes physiques conduisant à une génération de film séparateur à vitesse d'entrainement nulle sont étudiés. Un modèle éléments finis prenant en compte les aspects thermiques et transitoires est mis en œuvre pour determiner les quantités locales. En régime stationnaire, les résultats numériques sont comparés avec un très bon accord à un jeu de données issu d'une campagne d'expérimentations dédiée. Cette approche duale permet de quantifier l'influence de la charge, de la vitesse des surfaces et de la température externe sur l'épaisseur de film à vitesse d'entrainement nulle. Les contacts sont ensuite étudiés sous une charge variable, ce qui montre l'influence relative des phénomènes thermiques et transitoires pouvant générer une épaisseur de film. En fonction du ratio entre le temps caractéristique de chargement et le temps caractéristique d'échauffement, ces effets peuvent montrer une synergie bénéfique pour le contact.

Mots-clés : Lubrification TEHD, Vitesse d'Entrainement Nulle, *squeeze*, *viscosity wedge*

Abstract

Film thickness build-up in highly loaded lubricated contacts under Zero Entrainment Velocity condition

Highly loaded lubricated contacts are often studied in rolling/sliding conditions. In those cases, the entrainment of lubricant in a so-called "oil wedge" explains the existence of a separating film thickness. However, in a number of industrial applications, the contact is subjected to opposite surface velocities. In such cases, there is a Zero Entrainment Velocity (defined as the average velocity of the two surfaces) of the fluid. The film thickness prediction formulae developed in the literature for rolling contacts are unusable. In this thesis, the physical phenomena leading to a film build-up under Zero Entrainment Velocity condition are elucidated. A finite element model is used in order to facilitate in-situ measurements. It aims to describe the behaviour of the contact in thermal and transient conditions. In the stationary regime, the numerical values are compared with a very good agreement to a set of results obtained via a tailored experimental campaign. This dual approach enables a quantitative description of the influence of the contact load, surface velocities and external temperature on the film thickness under ZEV condition. Then, the relative influence of the thermal and squeeze effects is studied. Depending on the ratio between the characteristic loading time and the characteristic thermal time, these two effects can show a beneficial synergy for the contact.

Keywords: TEHL, ZEV, Squeeze, Viscosity wedge

Remerciements

Il m'apparaît évident de tout d'abord remercier mon directeur de thèse, Nicolas Fillot, pour son aide et sa présence tout au long du travail de thèse. J'ai fait face à une multitude de problèmes scientifiques, techniques et humains pendant ces trois ans et demi ; et tu as su me guider à chaque étape.

Je tiens ensuite à exprimer ma gratitude envers l'équipe de travail de SKF, avec à sa tête Guillermo Morales-Espejel. Tes interventions régulières et éclairées ont permis de définir un cadre précis à ce travail de thèse. Au même titre, je remercie également Franziska Meyer, Jonas Stahl, Armando Felix-Quiñonez et Lars-Erik Stacke.

Merci à tous les membres du jury d'avoir porté un intérêt à mon travail. Je tiens notamment à remercier à nouveau les rapporteurs de ma thèse : Wolfgang Seemann et Noël Brunetière. Votre contribution m'a permis de perfectionner mon manuscrit.

Cette thèse a été rendue possible par l'existence de la chair « Lubricated Interfaces for the Future », dont la première itération a été codirigée par Philippe Vergne. Merci d'avoir contribué à mon travail en apportant ton expertise tant sur le plan expérimental que rédactionnel. Il me semble naturel d'étendre ces remerciements à tous les membres de l'équipe TMI qui ont directement participé à la réalisation des essais expérimentaux. Merci donc à Nicolas Deveaux sans qui il n'y aurait tout simplement pas eu d'essais, Lionel Lafarge, Nathalie Bouscharain et David Philippon.

Merci à tous les amis du laboratoire, avec qui j'ai partagé des discussions mémorables. Une pensée émue pour Hugo, sa famille et tous ceux qui ont été impactés par son départ.

Merci aussi à tous les copains qui me supportent depuis toutes ces années. Je crois bel et bien que le niveau de mes blagues ne progressera jamais.

Enfin, merci à tous les membres de ma famille. Maman et Papa, vous m'avez inspiré la volonté de poursuivre des études scientifiques. Vous avez toujours su m'aider de la plus grande des manières, et je serai éternellement reconnaissant pour tout ce que vous m'avez donné. Ines et Esma, merci de m'avoir encouragé tout ce temps (et d'avoir participé à nos argumentations légendaires). J'ai la chance d'avoir une grande et belle famille, et je chérirai toujours votre présence.

En hommage à tonton Ali ; je saurai garder la tête haute.

Table of contents

Résumé 3

Abstract 3

Remerciements 5

Table of contents 7

Nomenclature 11

Résumé étendu 15

General introduction 39

Chapter 1. Introduction 41

1.1 History of the lubricated contact 42

1.2 Hertz theory 44

1.3 Elastohydrodynamic lubrication in rolling contacts: illustration on rolling element bearings 46

1.4 Other mechanisms for a load bearing capacity 50

1.4.1 Thermal effect: viscosity wedge 51

1.4.2 Transient effect: squeeze 52

1.4.3 Wall slip 55

1.5 Objectives and methodology 55

Chapter 2. Numerical and experimental approach 57

2.1 Numerical simulations 58

2.1.1 Modelling 58

2.1.2 Computational techniques 67

2.2 Experimental apparatus 69

2.2.1 Description of the test-rig 69

2.2.2 Film thickness measurements 72
2.2.3 Observed values of film thickness 73
2.3 Model validation and hypothesis discussion 74
2.3.1 Model validation in transient isothermal conditions 74
2.3.2 Experimental validation of the 2D model in stationary ZEV condition 76
2.3.3 Discussion on the 1D hypothesis 77
2.3.4 Discussion on the material properties of the solids 78
2.4 Conclusion 80
Chapter 3. Stationary TEHL ZEV contact 81
3.1 Local description of the viscosity wedge phenomenon 82
3.1.1 Antisymmetric configuration 82
3.1.2 Asymmetric configuration 88
3.2 Influence of the operating conditions 89
3.2.1 Influence of the velocity 89
3.2.2 Influence of the velocity for various contact loads 92
3.2.3 Influence of the velocity for various external temperatures 95
3.3 Conclusion 97
Chapter 4. Squeeze and thermal effects in wide ZEV contacts subjected to varying loads 99
4.1 Framework 100
4.1.1 Loading process 100
4.1.2 Initial state 102
4.2 Case A : Stationary thermal wedge 102
4.3 Case B : Isothermal squeeze 106
4.3.1 Squeeze from the literature 106
4.3.2 Film thickness variation 107
4.4 Case C : Squeeze and thermal wedge competing in film thickness build-up 109
4.4.1 Reference calculation 109

4.4.2 Influence of the characteristic thermal-transient ratio 110
4.5 Conclusion 113
Conclusion and perspectives 115
Conclusion 115
Recommendations for future work 117
Bibliography 119
Appendix 128
Résumé 139
Abstract 139

Nomenclature

Superscripts

Name	Description
$1D$	Line contact model (cylindrical)
$2D$	Point contact model (elliptic)
A	Stationary thermal conditions
B	Transient isothermal conditions
C	Transient thermal conditions

Subscripts

Name	Description
1	Solid 1
2	Solid 2
f	Fluid domain
m	Minimum (film thickness)
min	Minimum (overtime)
x	Along the x-axis
y	Along the y-axis
z	Along the z-axis

Other

Name	Description
$\bar{}$	Dimensionless value of a parameter
Δ	Difference between the value at $z = h$ with the value at $z = 0$

Parameters and variables – Roman alphabet

Name	Unit	Description
a	m	Main dry contact radius(Hertz)
a_v	K^{-1}	Parameter for the Murnaghan density formula
a_{CY}	$-$	Parameter for the Carreau-Yasuda non-Newtonian viscosity formula
A_1	K	Coefficient for the WLF viscosity correlation
A_2	Pa^{-1}	Coefficient for the WLF viscosity correlation
B_1	Pa^{-1}	Coefficient for the WLF viscosity correlation
B_2	$-$	Coefficient for the WLF viscosity correlation
$\bar{c}\|_{\Omega}$	$-$	Relative contribution to the total load bearing capacity
$\boldsymbol{C}$	$-$	Compliance matrix
C_1	$-$	Coefficient for the WLF viscosity correlation
C_2	$-$	Coefficient for the WLF viscosity correlation
C_f	$-$	Friction coefficient
C_p	$J.kg^{-1}.K^{-1}$	Heat capacity
D	$-$	Geometrical ellipticity ratio
E	Pa	Young's modulus (Elasticity ratio)
E'	Pa	Reduced Young's modulus
E_{eq}	Pa	Young's modulus of the equivalent solid
F	$-$	Variable for the WLF viscosity correlation
g	m	Rigid solid geometry (Geometrical term)
g_{h_m}	m	Geometrical component of the film thickness at the location of minimum film thickness
G	$-$	Dimensionless material parameter (Dowson-Higginson)
G_{CY}	Pa	Parameter for the Carreau-Yasuda non-Newtonian viscosity formula
h	m	Film thickness
h_0	m	Rigid body separation
h_c	m	Central film thickness
h_m	m	Minimum film thickness
h^*	m	Average film thickness
h_m^+	m	Higher local minimum film thickness
h_m^-	m	Lower local minimum film thickness
$h_{m,sa}^u$	m	Parameter in the semi-analytical prediction of h_m (variable velocity, other constant)
$h_{m,sa}^{u,w}$	m	Parameter in the semi-analytical prediction of h_m (variable velocity and load, other constant)
I_1	$m^2.s^1.kg^{-1}$	Integral term in the Generalised Reynolds equation
I_z	$m^3.s^1.kg^{-1}$	Integral term in the Generalised Reynolds equation

k	$W.m^{-1}.K^{-1}$	Thermal conductivity
k_{ell}	$-$	Reduced ellipticity modulus
K_{00}	$-$	Parameter for the Murnaghan density formula
K_M	$-$	Parameter for the Murnaghan density formula
K'_M	$-$	Parameter for the Murnaghan density formula
L	$-$	Dimensionless Moes parameter
m	kg	Mass of an elemental fluid particle
M_1	$-$	Dimensionless Moes parameter
n_{CY}	$-$	Parameter for the Carreau-Yasuda non-Newtonian viscosity formula
p	Pa	Pressure
p_h	Pa	Dry contact maximum pressure(Hertz)
P_c^{1D}	$W.m^{-1}$	Total heat source per unit length through compression
P_f^{1D}	$W.m^{-1}$	Total heat source per unit length
P_s^{1D}	$W.m^{-1}$	Total heat source per unit length through shearing
Q	$W.m^{-3}$	Total heat source
Q_c	$W.m^{-3}$	Compression heat source
Q_s	$W.m^{-3}$	Shear heat source
R	m	Radius
R_d	$-$	Coefficient of determination
S_a	m	Average surface roughness
SRR	$-$	Slide to roll ratio
t	s	Time
$t_{Loading}$	s	Loading time
t_{Final}	s	Final time of study
T	K	Temperature
T_0	K	External temperature
T_g	K	Glass transition temperature
T_{g0}	K	Glass transition temperature at ambient pressure
T_R	K	Reference temperature
u	$m.s^{-1}$	Velocity
u_e	$m.s^{-1}$	Entrainment velocity
u_s	$m.s^{-1}$	Sliding velocity
$u_{m,sa}^{u}$	$m.s^{-1}$	Parameter in the semi-analytical prediction of h_m (variable velocity, other constant)
$u_{m,sa}^{u,w}$	$m.s^{-1}$	Parameter in the semi-analytical prediction of h_m (variable velocity and load, other constant)
U	$-$	Dimensionless speed parameter (Dowson-Higginson)
U_δ	m	Elastic displacement component along $\vec{x}$
$\overrightarrow{\boldsymbol{U_\delta}}$	m	Elastic displacement vector
V_δ	m	Elastic displacement component along $\vec{y}$

w^{1D}	$N.m^{-1}$	Load per unit length
w_i^{1D}	$N.m^{-1}$	Initial load per unit length
w_f^{1D}	$N.m^{-1}$	Final load per unit length
w^{2D}	N	Load
$w_{m,sa}^{u,w}$	$N.m^{-1}$	Parameter in the semi-analytical prediction of h_m (variable velocity and load, other constant)
W_1	$-$	Dimensionless load parameter (Dowson-Higginson)
W_δ	m	Elastic displacement component along $\vec{z}$

Parameters and variables – Greek alphabet

Name	Unit	Description
α	Pa^{-1}	Pressure-viscosity coefficient
α^*	Pa^{-1}	Reciprocal asymptotic isoviscous pressure-viscosity coefficient
$\alpha_{m,sa}^{u,w}$	$-$	Parameter in the semi-analytical prediction of h_m (variable velocity and load, other constant)
β_k	K^{-1}	Parameter for the Murnaghan density formula
$\dot{\gamma}$	s^{-1}	Shear rate
δ	m	Elastic surface displacement
δ_{h_m}	m	Elastic surface displacement at the location of minimum film
$\varepsilon_{elastic}$	$-$	Strain tensor
ϵ_{ell}	$-$	Elliptic integral
η	$Pa.s$	Dynamic viscosity
η_G	$Pa.s$	Viscosity at glass transition
v	$-$	Poisson coefficient
v_{eq}	$-$	Poisson coefficient of the equivalent solid
$\sigma_{elastic}$	$-$	Stress tensor
σ_s	m	Surface roughness
ρ	$kg.m^{-3}$	Density
ρ_R	$kg.m^{-3}$	Reference density
ρ^*	$kg.m^{-3}$	Generalised density
$\left(\frac{\rho}{\eta}\right)_e$	$m.s$	Generalised density/viscosity ratio
τ	Pa	Shear stress
τ_e	Pa	Shear stress norm
Ω	$-$	Domain of calculation

Résumé étendu

1. Introduction

La lubrification est souvent employée afin de réduire les pertes énergétiques dans les systèmes mécaniques, ainsi que pour augmenter la durée de vie des composants. Les surfaces en contact entrainent le lubrifiant (gaz, liquide ou graisse) dans la zone de contact, générant une épaisseur de film séparatrice. La courbe de Stribeck (Figure i-1) met en évidence trois comportements des contacts lubrifiés.

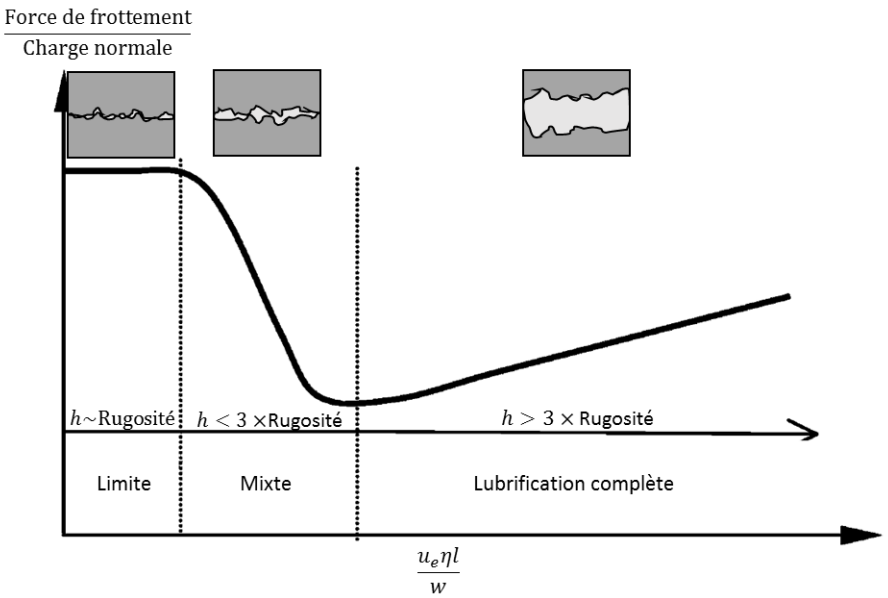

Figure i-1 – Courbe de Stribeck (issue de [1]*) avec l une longueur caractéristique du contact, w la charge appliquée, u_e la vitesse d'entrainement en glissement pur, η la viscosité dynamique et h l'épaisseur de film séparant les surfaces.*

Dans les régimes limites et mixtes, des frottements secs entre les rugosités des surfaces en contact se produisent. En revanche, le régime de lubrification complète est synonyme d'une séparation totale des surfaces par le lubrifiant, qui supporte alors la totalité de la charge appliquée. Dans les cas à forte charge, il est nécessaire de prendre en compte la déformation élastique des solides en contact ([2]–[5]). Le régime de lubrification est alors appelé lubrification élastohydrodynamique (EHD). Il existe des contacts EHD entre les éléments roulants et chacune des bagues (Marqués A et B dans la Figure i-2) des roulements qui sont utilisés pour assurer le guidage en rotation des machines.

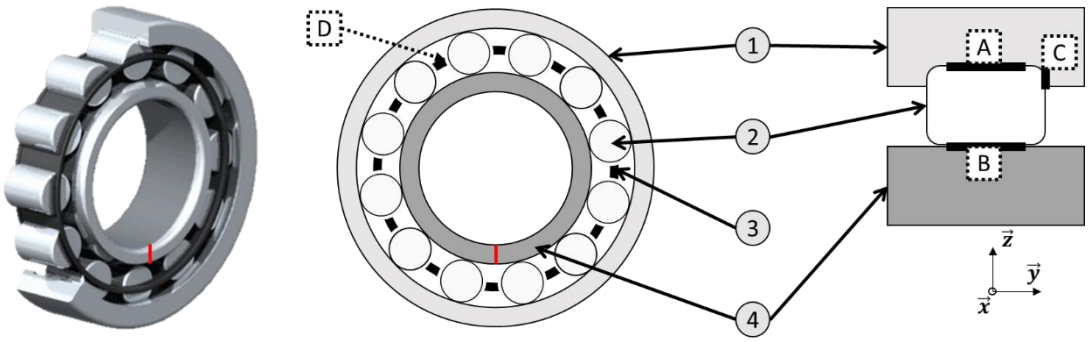

Figure i-2 – Sur la gauche : Roulement à rouleaux. Au centre : Vue de côté du même roulement. Sur la droite : Vue tangentielle partielle du roulement à proximité d'un élément roulant.

Dans ces contacts, les vitesses tangentielles des surfaces sont sensiblement égales : on parle de roulement pur. Différents auteurs ont proposé des modèles de prédiction d'épaisseur de film séparant les solides en contact. Dans ces formules, l'épaisseur de film est proportionnelle à la vitesse d'entrainement (définie comme la moyenne des vitesses des deux surfaces) à une puissance donnée ([4]–[12]). Il est possible d'enlever la cage afin de remplir l'espace disponible avec des éléments roulants (Figure i-3).

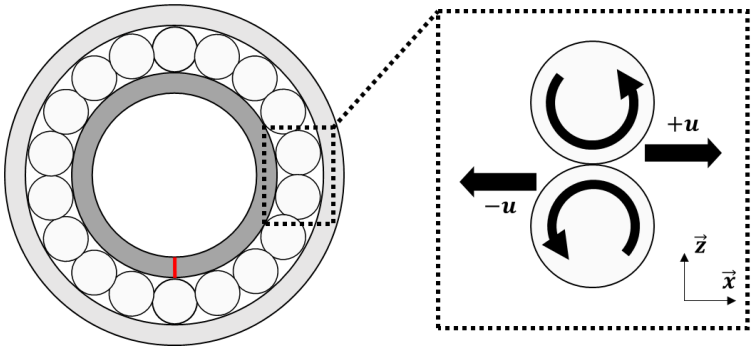

Figure i-3 – Sur la gauche : Vue de côté d'un roulement sans cage. Sur la gauche : Contact entre deux éléments roulants.

Dans ce cas, des contacts entre éléments roulants successifs se produisent. Ceux-ci sont marqués par une vitesse d'entrainement nulle, avec des surfaces se déplaçant avec des vitesses tangentielles égales mais opposées en sens. Les formules semi-analytiques décrites précédemment deviennent alors inutilisables. Néanmoins, ces contacts sont capables de supporter une charge en régime de lubrification EHD ([13]–[16]). Trois effets peuvent expliquer la génération d'un film séparateur à vitesse d'entrainement nulle.

a) Puisque les surfaces en contact se déplacent avec des vitesses tangentielles opposées, alors le contact est soumis à un intense cisaillement. Par conséquent, le fluide s'échauffe au centre du contact. De part et d'autre du contact, du fluide froid entre et du fluide chaud s'échappe. Ce gradient de température implique un gradient de viscosité, expliquant la génération d'une pression supportant la charge. Cet effet thermique est nommé *« viscosity wedge »*[17]. Par la suite, la prise en compte des effets thermiques dans l'étude des contacts lubrifiés se réfère aux contacts TEHD.
b) La dynamique du roulement sans cage implique des mouvements de va-et-vient entre les éléments roulants. Le chargement soudain de la zone de contact provoque le

piégeage d'une partie du lubrifiant entre les deux surfaces. Ceci permet de supporter la charge temporairement. Cet effet transitoire est nommé *« squeeze »*[18].

c) L'entrainement d'un fluide par des parois solides est conditionné par les propriétés d'adhésion entre ces dernières[19]. Pour des couples solide/fluide à faible adhésion, un glissement du fluide aux parois est possible. Dans les contacts à vitesse d'entrainement nulle, il est alors possible que l'une des interfaces solide/fluide soit soumise à un glissement, ce qui modifie la vitesse d'entrainement effective et conduit à une génération de pression.

L'étude présentée dans ce document se porte sur les contacts acier/acier que l'on trouve pour deux éléments roulants d'un roulement sans cage. Ainsi, à cause de la rugosité des surfaces en jeu, les effets de glissement aux parois ne seront pas étudiés. L'objectif de ce travail est de développer une approche quantitative permettant d'évaluer les effets de *« viscosity wedge »* et de *« squeeze »* sur l'épaisseur minimale de film séparant deux rouleaux en contact à une vitesse d'entrainement nulle.

2. Approche numérique et expérimentale

Modélisation numérique

Le modèle numérique par éléments finis présenté ici fait suite aux travaux de Raisin[20] et Wheeler[21]. Les équations sont toutes écrites en considérant le contact entre un tonneau (2D) et un plan. Dans les cas où le solide est considéré comme un cylindre à base circulaire infiniment long, tous les termes et dérivées dans la direction axiale sont annulés (1D). Le temps est dénoté par le paramètre t. Le domaine de résolution des équations de l'EHD est représenté sur la Figure i-4.

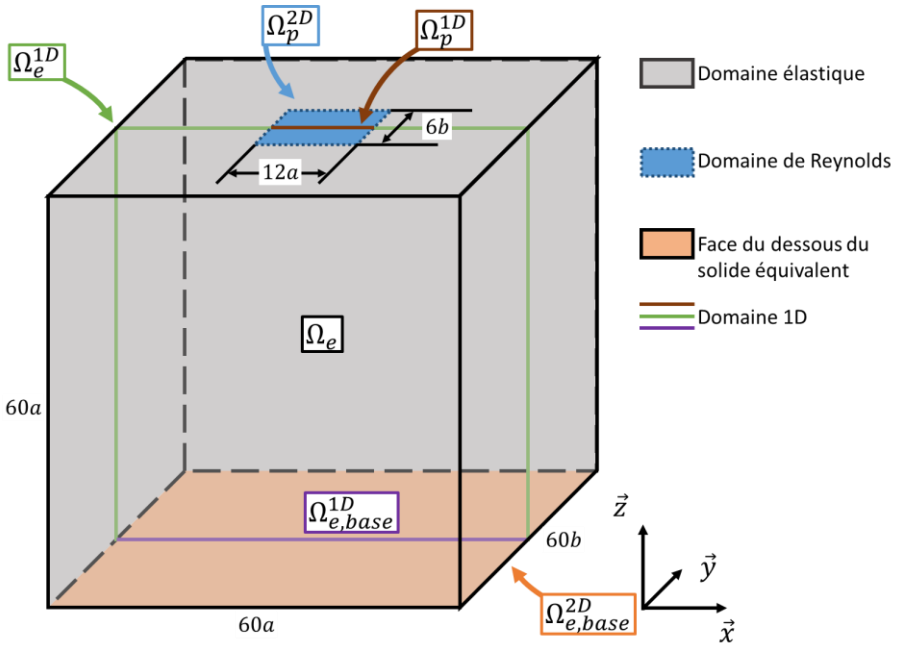

Figure i-4 – Domaines de résolution des équations de l'EHD.

L'épaisseur de film h séparant les solides s'écrit comme dans eq. i-1.

$$h(x,y,t) = h_0(t) + \underbrace{\frac{x^2}{2R_{eq,x}^{2D}} + \frac{y^2}{2R_{eq,y}^{2D}}}_{g(x,y)} + \delta(x,y,t) \qquad \textit{eq. i-1}$$

avec h_0 la séparation rigide des solides, δ le déplacement élastique des surfaces et $R_{eq,x}^{2D}$ et $R_{eq,y}^{2D}$ les rayons équivalents du contact selon x et y respectivement (voir eq. i-2).

$$\frac{1}{R_{eq,x}^{2D}} = \frac{1}{R_{1,x}^{2D}} + \frac{1}{R_{2,x}^{2D}}$$
$$\frac{1}{R_{eq,y}^{2D}} = \frac{1}{R_{1,y}^{2D}} + \frac{1}{R_{2,y}^{2D}} \qquad \textit{eq. i-2}$$

avec $R_{1,x}^{2D}$, $R_{1,y}^{2D}$, $R_{2,x}^{2D}$ et $R_{2,y}^{2D}$ les rayons de courbure des solides 1 et 2 selon x et y.

Le film fluide est considéré mince, ce qui implique une pression constante dans l'épaisseur. Les effets d'inertie et de tension de surfaces sont négligeables par rapport aux efforts visqueux. L'écoulement est considéré laminaire. Aucun glissement aux parois n'est considéré. Ainsi, l'équation de Navier-Stokes (eq. i-3) est écrite sous une forme simplifiée : l'équation de Reynolds Généralisée (eq. i-4) sur le domaine Ω_p. Aux limites du domaine, une pression nulle est imposée ($p = 0$).

$$\vec{\nabla} p = \frac{\partial}{\partial z}(\overrightarrow{\tau_z}) \qquad \textit{eq. i-3}$$

$$\vec{\nabla}.\left(\left(\frac{\rho}{\eta}\right)_e \vec{\nabla} p\right) - \vec{\nabla}.\overrightarrow{\rho^*} - \frac{\partial \rho_e}{\partial t} = 0 \qquad \textit{eq. i-4}$$

avec $\rho_e = \int_0^h \rho dz$, $\rho_e' = \int_0^h \left(\rho \int_0^z \frac{dz'}{\eta}\right) dz$, $\rho_e'' = \int_0^h \left(\rho \int_0^z \frac{z' dz'}{\eta}\right) dz$ et $\left(\frac{\rho}{\eta}\right)_e = \frac{\eta_e}{\eta_e'}\rho_e' - \rho_e''$, $\overrightarrow{\rho^*} = \begin{pmatrix} \rho_e' \eta_e (u_2 - u_1) + \rho_e u_1 \\ 0 \end{pmatrix}$.

La masse volumique ρ (eq. i-5, Murnaghan et al.[22]) et la viscosité dynamique η (eq. i-6, WLF[23]) des fluides demandent une modélisation précise. Ces deux variables dépendent de la température et de la pression et peuvent varier dans l'épaisseur (z) du fluide. Dans le cas où le fluide est non-Newtonien (eq. i-7, Carreau-Yasuda[24]), il convient d'inclure la dépendance de sa viscosité avec la norme de la contrainte de cisaillement τ_e.

$$\rho(p,T) = \rho_R \frac{1}{\left(1 + \frac{K_M'}{K_M} p\right)^{-\frac{1}{K_M'}}} \frac{1}{1 + a_v(T_0 - T_R)} \qquad \textit{eq. i-5}$$

avec $K_M = K_{00} e^{-\beta_K T}$, et β_k le paramètre de température-masse volumique.

$$\eta(p,T) = \eta_G \left(\frac{-2.303\ C_1 (T - T_g) F}{C_2 + (T - T_g) F} \right) \qquad \textit{eq. i-6}$$

avec $T_g(p) = T_{g0} + A_1 \ln(1 + A_2 p)$ et $F(p) = (1 + B_1 p)^{B_2}$

A_1, A_2, B_1, B_2 ainsi que C_1 et C_2 sont les paramètres du modèle. η_G est la viscosité à la transition vitreuse et T_{g0} est la température à la transition vitreuse et à pression ambiante.

$$\eta(p,T,\tau_e) = \frac{\eta(p,T)}{\left(1 + \left(\frac{\tau_e}{G_{CY}}\right)^{a_{CY}}\right)^{\frac{\frac{1}{n_{CY}} - 1}{a_{CY}}}} \qquad \textit{eq. i-7}$$

avec $\tau_e = \sqrt{{\tau_{zx}}^2 + {\tau_{zy}}^2}$

$\tau_{zx} = \eta \frac{\partial u_{fx}}{\partial z}$ et $\tau_{zy} = \eta \frac{\partial u_{fy}}{\partial z}$ sont les contraintes de cisaillement selon les axes x et y. u_{fx} et u_{fy} sont les termes locaux de vitesse du fluide.

Le déplacement élastique des surfaces est calculé en résolvant l'eq. i-8 sur le solide équivalent (noté Ω_e sur la Figure i-4). La pression donnée par l'équation de Reynolds Généralisée est imposée sur le domaine élastique ($\boldsymbol{\sigma_{elastic}} = -p\vec{z}$). Sous ce même domaine, une condition d'encastrement est mise en place ($\overrightarrow{\boldsymbol{U_\delta}} = \vec{0}$).

$$\nabla . \boldsymbol{\sigma_{elastic}} = 0 \qquad \textit{eq. i-8}$$

avec $\boldsymbol{\sigma_{elastic}} = \boldsymbol{C\varepsilon_{elastic}}(\overrightarrow{\boldsymbol{U_\delta}})$ et $\overrightarrow{\boldsymbol{U_\delta}} = \{U_\delta,\ V_\delta,\ W_\delta\}$ le vecteur des déplacements élastiques. $\boldsymbol{C}$ est la matrice de compliance et $\boldsymbol{\varepsilon_{elastic}}$ le tenseur des contraintes classiquement établit pour le calcul de déformation élastique de solides isotropes. A partir du champ des déplacements, il est possible de calculer $\delta = |W_\delta|_{\Omega_p}$.

L'équation d'équilibre de la charge permet d'identifier la séparation rigide des solides :

$$\iint_{\Omega_p^{2D}} p\ dxdy = w^{2D} \text{ ou } \int_{\Omega_p^{1D}} p dx = w^{1D} \qquad \textit{eq. i-9}$$

La température dans les solides et dans le fluide est calculée en résolvant l'équation de l'énergie (eq. i-10). La température initiale et sur toutes les frontières pour lesquelles de la matière entre dans le domaine est notée T_0. Un flux de chaleur constant est écrit entre chaque surface et le fluide ($k_f \frac{\partial T}{\partial z}\Big|_{z=0^+} = k_1 \frac{\partial T}{\partial z}\Big|_{z=0^-}$ et $k_2 \frac{\partial T}{\partial z}\Big|_{z=h^+} = k_f \frac{\partial T}{\partial z}\Big|_{z=h^-}$).

$$-\nabla(k_i \nabla T) + \rho_i C_{pi}(\vec{u}_i \nabla T + \frac{\partial T}{\partial t}) = Q_i \qquad \textit{eq. i-10}$$

avec k la conductivité thermique du solide i et C_p sa capacité thermique. La source de chaleur totale Q_i est définie dans le fluide.

$$Q_i = \begin{cases} 0 & \text{for } i = \{1,2\} \\ Q_s + Q_c = \eta\left(\nabla\vec{u}_f\right)^2 - \dfrac{T}{\rho}\dfrac{\partial\rho}{\partial T}\left(\vec{u}_f.\vec{\nabla}p\right) & \text{for } i = f \end{cases} \qquad \textit{eq. i-11}$$

avec Q_s et Q_c les sources de chaleur par cisaillement et compression respectivement.

Dispositif expérimental

Devant le manque de résultats expérimentaux permettant de confronter le modèle pour des géométries elliptiques, une campagne d'essais est mise en place sur le tribomètre Jerotrib[25]. Un tonneau ($R_{2,x}^{2D} = 0{,}013\ m$ et $R_{2,y}^{2D} = 0{,}330\ m$) en acier est chargé sous un disque en saphir choisi pour sa transparence, permettant ainsi la mesure de l'épaisseur de film par interférométrie. Le saphir présente une similarité thermique avec l'acier ; l'hypothèse selon laquelle ce contact est semblable à un contact acier/acier est donc émise et discutée ci-après. Les surfaces sont polies de sorte à ce qu'elles présentent chacune une rugosité inférieure à $5\ nm$. Le lubrifiant est projeté de part et d'autre du contact à l'aide d'une pompe péristaltique. Un système de circulation du lubrifiant est mis en place, afin de contrôler sa température dans un bain externe. Les propriétés des solides et du lubrifiant (Shell T9) sont donnés dans le Tableau i-1 et le

$C_{pf}\ [J.kg^{-1}.K^{-1}]$	1900	C_2	14.1596
$k_f\ [W.m^{-1}.K^{-1}]$	0.118	A_1	188.95
$\rho_R\ [kg.m^{-3}]$	872	$A_2\ [Pa^{-1}]$	0.533×10^{-9}
$T_R\ [K]$	298	$B_1\ [Pa^{-1}]$	7.37×10^{-9}
$K_{00}\ [Pa]$	9.234×10^9	B_2	-0.6171
$K_M{}'$	10.545	$T_{g0}\ [K]$	204.68
$a_v\ [K^{-1}]$	7.734×10^{-4}	$p_0\ [Pa]$	0
$\beta_k\ [K^{-1}]$	6.09×10^{-3}	a_{CY}	5
$\eta_g\ [Pa.s]$	1×10^{12}	n_{CY}	0.35
C_1	15.9035	$G_{CY}\ [Pa]$	7×10^6

Tableau i-2 respectivement.

	Acier	Saphir
$E\ [Pa]$	210×10^9	360×10^9
υ	0,3	0,34
$\rho\ [kg.m^{-3}]$	7850	4000
$Cp\ [J.kg^{-1}.K^{-1}]$	470	750
$k\ [W.m^{-1}.K^{-1}]$	46	40

Tableau i-1 – Propriétés thermoélastiques de l'acier et du saphir ([26], [27]*).*

$C_{pf}\ [J.kg^{-1}.K^{-1}]$	1900	C_2	14.1596
$k_f\ [W.m^{-1}.K^{-1}]$	0.118	A_1	188.95
$\rho_R\ [kg.m^{-3}]$	872	$A_2\ [Pa^{-1}]$	0.533×10^{-9}
$T_R\ [K]$	298	$B_1\ [Pa^{-1}]$	7.37×10^{-9}
$K_{00}\ [Pa]$	9.234×10^{9}	B_2	-0.6171
$K_M{}'$	10.545	$T_{g0}\ [K]$	204.68
$a_v\ [K^{-1}]$	7.734×10^{-4}	$p_0\ [Pa]$	0
$\beta_k\ [K^{-1}]$	6.09×10^{-3}	a_{CY}	5
$\eta_g\ [Pa.s]$	1×10^{12}	n_{CY}	0.35
C_1	15.9035	$G_{CY}\ [Pa]$	7×10^{6}

Tableau i-2 – Propriétés du fluide ([26], [28]*).*

Le principe d'interférométrie est utilisé pour mesurer l'épaisseur de film par méthode optique (voir Molimard[29] et Wheeler et al.[26]). 50 cas de mesures sont conduits (voir Tableau i-3), avec pour chaque cas 6 interférogrammes utilisés afin de déterminer les épaisseurs de film.

$T_0\ (K)$	$u(m/s)$	$\mathrm{w}^{2\mathrm{D}}(N)$	$p_h(GPa)$	Equivalent $\mathrm{w}^{1\mathrm{D}}(N.m^{-1})$	Nombre de cas
293,15	{1,77; 1,99; 2,26; 2,51; 2,81; 3,16; 3,54; 3,97; 4,46; 5,00; 5,61; 6,30; 7,06; 7,92}	30	0,390	$4{,}14 \times 10^{4}$	14
293,15		50	0,462	$5{,}82 \times 10^{4}$	14
293,15		100	0,582	$9{,}24 \times 10^{4}$	14
308,15	{3,16; 3,97; 5,00; 6,30; 7,92}	50	0,462	$5{,}82 \times 10^{4}$	5
323,15	{5,00; 6,30; 7,92}	50	0,462	$5{,}82 \times 10^{4}$	3

Tableau i-3 – Jeu de mesures pour le disque en saphir.

Un exemple d'interférogramme est montré dans la Figure i-5. La zone d'intérêt permettant de comparer les versions 1D et 2D du modèle se situe le long du tireté. Par la suite, l'épaisseur minimale $\mathrm{h_m}$ désignera la valeur moyenne de l'épaisseur mesurée en C et D.

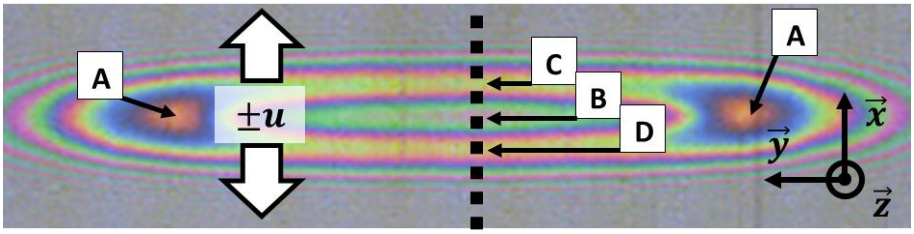

Figure i-5 – Interférogramme obtenu avec un disque en saphir (Grossissement $\times 10$*,* $u = 5\ m/s$*,* $w^{2D} = 50\ N$ *et* $T_0 = 293{,}15\ K$*).*

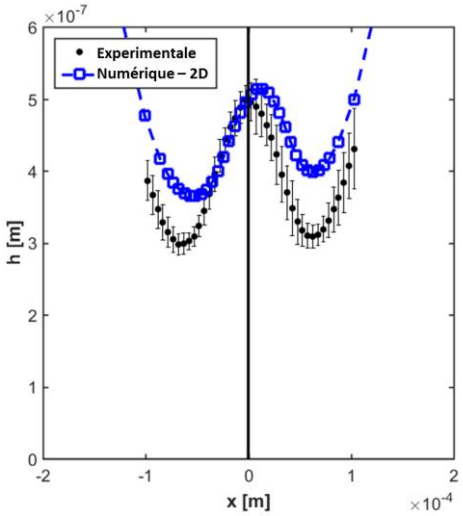

Figure i-6 – Profil d'épaisseur de film dans le cas de référence ($u = 5\ m/s$, $w^{2D} = 50\ N$ et $T_0 = 293.15\ K$). La moyenne obtenue sur 6 interférogrammes est représentée, les barres verticales représentant trois fois l'écart type.

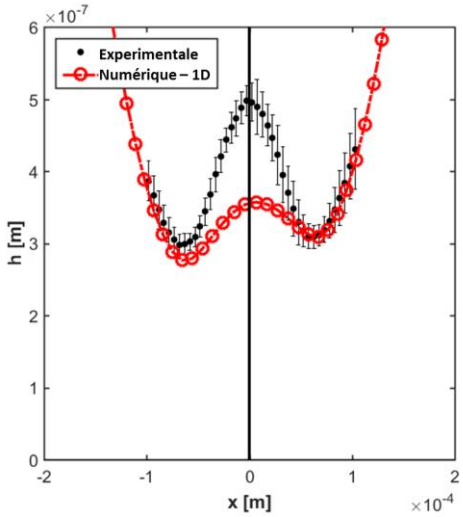

Figure i-7 – Profil d'épaisseur de film dans le cas de référence ($u = 5\ m/s$, $w^{2D} = 50\ N$ et $T_0 = 293.15\ K$). La moyenne obtenue sur 6 interférogrammes est représentée, les barres verticales représentant trois fois l'écart type.

La procédure expérimentale permet de confronter le modèle en conditions stationnaires thermiques. Dans un cas de référence ($u = 5\ m/s$, $w = 50\ N$ et $T_0 = 293.15\ K$) représenté sur la Figure i-6, le modèle 2D prédit l'épaisseur centrale de film avec un écart relatif de 2.8%. Pour l'épaisseur minimale, cet écart est de 23.9%.

Avec la géométrie du contact, il est possible de supposer une équivalence entre la ligne centrale du modèle 2D et le modèle 1D[30]. Il est alors possible de comparer les résultats expérimentaux au modèle, comme dans la Figure i-7. Dans ce cas, il y a une différence relative de 28.3% pour l'épaisseur centrale, et de 3.3% pour l'épaisseur minimale. Ce modèle est exclusivement utilisé par la suite.

Les essais étant effectués avec un disque en saphir, il convient de comparer le cas acier/saphir au cas acier/acier. Les calculs dans les deux cas, et pour les conditions de références, sont représentés sur la Figure i-8. Il existe une différence relative de 7.82% entre les valeurs d'épaisseur centrale, et de 0.63% pour l'épaisseur minimale. L'asymétrie observée pour l'acier/saphir s'explique par la dissimilarité thermique entre les matériaux.

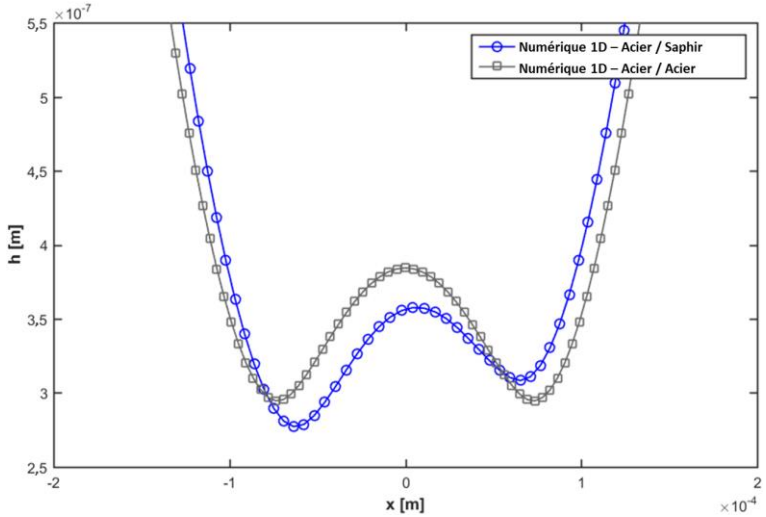

Figure i-8 – Profil d'épaisseur de film dans le cas 1D de référence ($u = 5\ m/s$, $w^{1D} = 5.82 \times 10^4\ N.m^{-1}$ et $T_0 = 293.15\ K$) pour différents couples de matériaux en contact.

En conclusion, un modèle numérique par éléments finis permet de calculer la pression, l'épaisseur de film et le champ de température dans un contact EHD soumis à des conditions transitoires et une vitesse d'entrainement nulle. Une campagne d'essais a permis la validation du modèle en conditions stationnaires. L'utilisation du modèle en hypothèse 1D permet une bonne approximation de l'épaisseur minimale de film séparant les solides. De plus, les résultats pour le couple acier/saphir sont très proches du cas acier/acier.

3. Contact TEHD à vitesse d'entrainement nulle en condition stationnaire

Description du phénomène de « viscosity wedge »

Le modèle 1D est utilisé afin de mesurer les quantités locales et ainsi comprendre les physiques mises en œuvre. Les solides sont fait en acier (Tableau i-1), et le fluide est le même qu'auparavant (

$C_{pf}\ [J.kg^{-1}.K^{-1}]$	1900	C_2	14.1596
$k_f\ [W.m^{-1}.K^{-1}]$	0.118	A_1	188.95
$\rho_R\ [kg.m^{-3}]$	872	$A_2\ [Pa^{-1}]$	0.533×10^{-9}
$T_R\ [K]$	298	$B_1\ [Pa^{-1}]$	7.37×10^{-9}
$K_{00}\ [Pa]$	9.234×10^{9}	B_2	-0.6171
$K_M{}'$	10.545	$T_{g0}\ [K]$	204.68
$a_v\ [K^{-1}]$	7.734×10^{-4}	$p_0\ [Pa]$	0
$\beta_k\ [K^{-1}]$	6.09×10^{-3}	a_{CY}	5
$\eta_g\ [Pa.s]$	1×10^{12}	n_{CY}	0.35
C_1	15.9035	$G_{CY}\ [Pa]$	7×10^{6}

Tableau i-2). Différentes répartitions sont représentées sur la Figure i-9. Par la suite, $T_0 = 293.15$ K, $R^{1D} = 0.0128\ m$, $u = 2\ m.s^{-1}$ et $w^{1D} = 58198\ N.m^{-1}$.

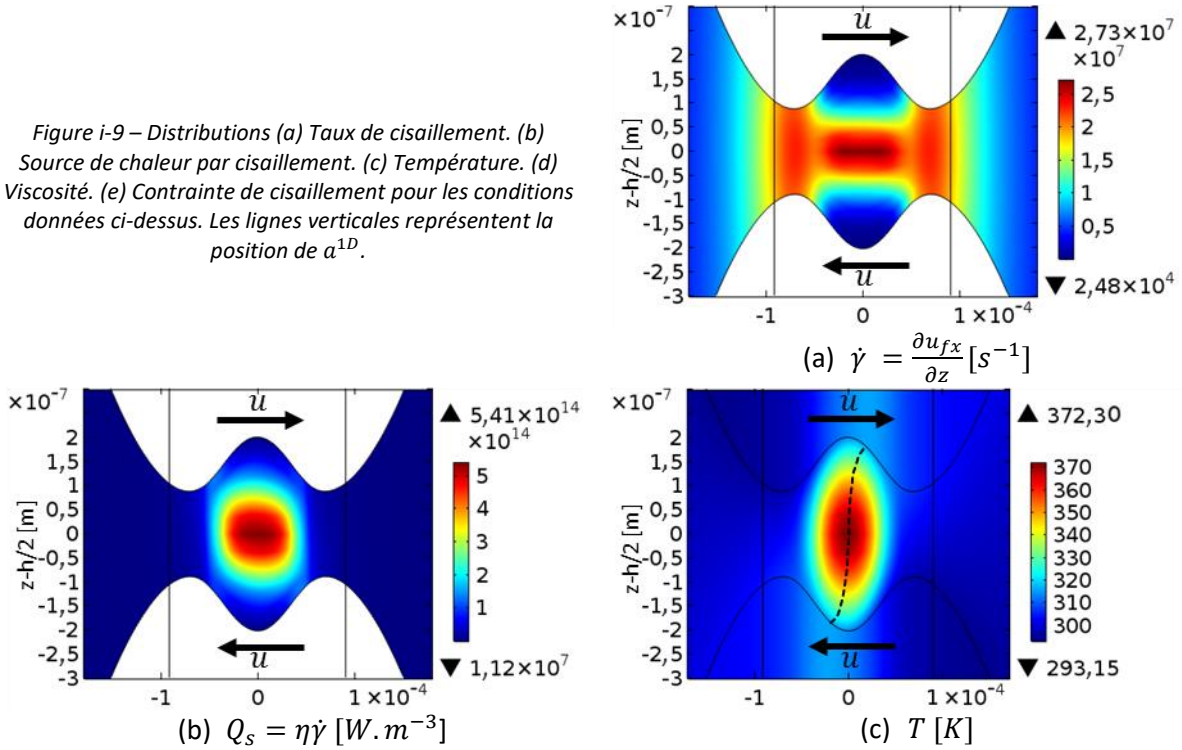

Figure i-9 – Distributions (a) Taux de cisaillement. (b) Source de chaleur par cisaillement. (c) Température. (d) Viscosité. (e) Contrainte de cisaillement pour les conditions données ci-dessus. Les lignes verticales représentent la position de a^{1D}.

(a) $\dot{\gamma} = \frac{\partial u_{fx}}{\partial z}\ [s^{-1}]$

(b) $Q_s = \eta\dot{\gamma}\ [W.m^{-3}]$

(c) $T\ [K]$

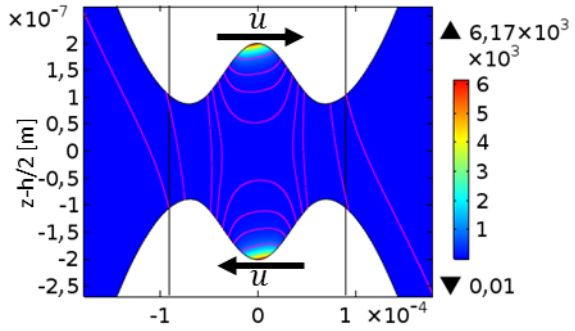

(d) $\eta\ [Pa.s]$ – Isovaleurs en rose $\{0{,}018\ ;\ 0{,}026\ ;\ 0{,}5\ ;\ 2\ ;\ 10\ ;50\ ;\ 200\ ;\ 1000\}\ Pa.s$

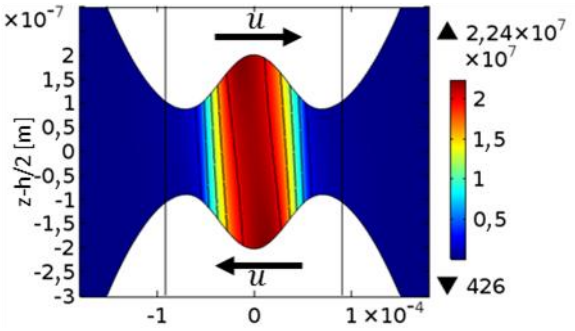

(e) $\tau_{zx}\ [Pa]$ – 5 Isovaleurs en noir

La puissance dissipée par compression représente moins de $0{,}01\%$ de la puissance totale dissipée. Ainsi, il est possible de considérer le cisaillement comme seule source de chaleur dans le système. Le profil de cisaillement est donc représenté (Figure i-9(a)). Sa valeur est maximale au centre du contact ($2{,}73 \times 10^7\ s^{-1}$). Des valeurs élevées sont aussi observées aux lieux des épaisseurs minimales.

La génération de chaleur par cisaillement est le produit du taux de cisaillement par la viscosité. Les fortes pressions au centre de ces contacts impliquent de fortes valeurs de viscosité au même lieu. Ainsi, la valeur maximale de la source de chaleur par cisaillement (Figure i-9(b)) se trouve au centre du contact ($5{,}41 \times 10^{14}\ W.m^{-3}$).

La distribution de température est représentée sur la Figure i-9(c). La nature antisymétrique du contact implique une vitesse nulle en son centre. Le terme de transport de l'équation de l'énergie devient alors lui aussi nul. De plus, les conditions aux limites sur la température aux frontières extérieures du domaine conduisent à la conduction de chaleur du centre du contact vers l'extérieur. La ligne noire indique la position du maximum de température selon chacune des lignes l telles que $z = \chi h$ pour $\chi \in [0,1]$. Ainsi, la température maximale se trouve au centre du contact ($372{,}3\ K$). Les solides se déplaçant, le fluide proche des parois se déplace lui aussi. Ainsi, du fluide à haute température se retrouve vers les sorties du contact. Des gradients verticaux de température peuvent alors être observés entre les lignes $z = h$ et $z = 0$ (eq. i-12, Figure i-10). Leur valeur maximale se trouvant à $x = \pm 0{,}52a^{1D}$. Les valeurs maximales de viscosité se trouvent aux lieux de fortes pressions et faibles températures. Cela correspond environ aux coordonnées $(0{,}0)$ et $(0, h)$ dans la Figure i-9(d).

$$\Delta T(x) = T(x,h) - T(x,0) \qquad \textit{eq. i-12}$$

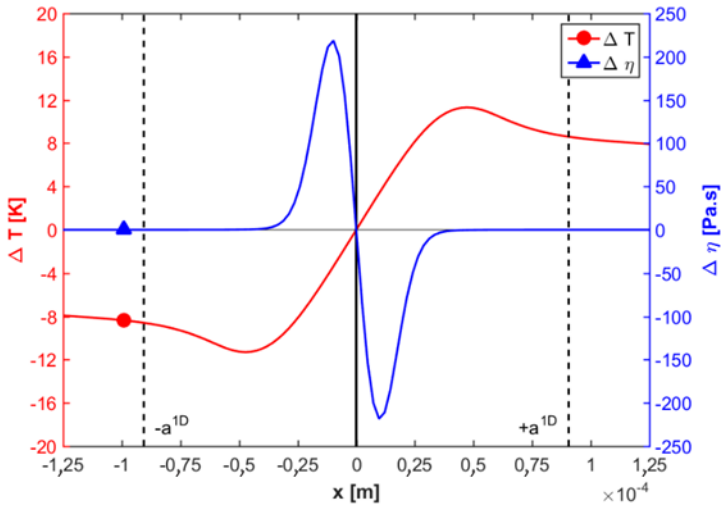

Figure i-10 – Différences de température et de viscosité entre les deux interfaces à $2\ m.s^{-1}$.

Seuls les gradients de températures (hypothèse des films minces) peuvent provoquer des gradients de viscosité (eq. i-13, Figure i-10), qui trouvent leur maximum plus proche du centre.

$$\Delta\eta(x) = \eta(x,h) - \eta(x,0) \qquad \textit{eq. i-13}$$

Le produit du taux de cisaillement par la viscosité est la contrainte de cisaillement (Figure i-9(e)). Selon l'hypothèse des films minces $\frac{\partial p}{\partial x}$ ne varie pas selon z. Ainsi, sa moyenne vaut :

$$\frac{\partial p}{\partial x} = \frac{1}{h}\int_0^h \frac{\partial p}{\partial x} dz \qquad \textit{eq. i-14}$$

En combinant eq. i-3 et eq. i-14, et en développant le terme de contrainte de cisaillement il est possible d'écrire le gradient de pression comme une fonction de la contrainte de cisaillement et de l'épaisseur de film (eq. i-15). Le gradient vertical de cette contrainte entraine la génération de pression dans le contact.

$$\frac{\partial p}{\partial x} = \frac{1}{h}\int_0^h \frac{\partial p}{\partial x} dz = \frac{1}{h}\int_0^h \frac{\partial(\eta\dot{\gamma})}{\partial z} dz = \frac{(\eta\dot{\gamma})_h - (\eta\dot{\gamma})_0}{h} = \frac{\Delta(\eta\dot{\gamma})}{h} \qquad \textit{eq. i-15}$$

Le gradient en x de pression ainsi que le profil de pression sont représentés sur la Figure i-11.

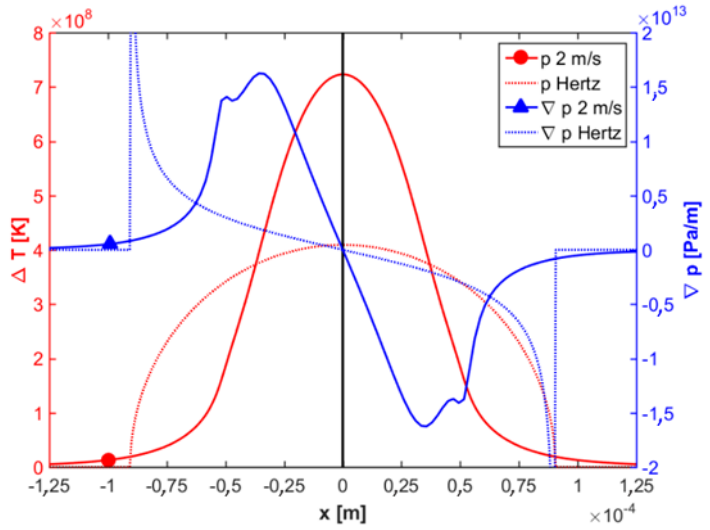

Figure i-11 – Pression et gradient de pression à $2\ m.s^{-1}$ et la référence du contact sec défini par Hertz.

Les profils de Hertz (correspondant au contact sec) servent de référence. Dans ce cas, le gradient de pression maximal se trouve à $x = \pm 0{,}4a^{1D}$. Cela signifie une pression relativement faible à $\pm a^{1D} > |x| > \pm 0{,}4a^{1D}$. Afin que le contact puisse supporter la charge totale, cela conduit à une pression centrale $1{,}77$ fois plus importante que la définition faite par Hertz dans le contact sec, ce qui explique la présence du volume de fluide appelé *« dimple » au centre du contact*.

Les liens entre les différents paramètres et variables du système sont illustrés sur la Figure i-12. Il est possible d'identifier comment les paramètres de contrôle interviennent dans le problème. De plus, le comportement complexe des contacts à Vitesse d'Entrainement Nulle se retrouve grâce au nombre conséquent de variable couplées.

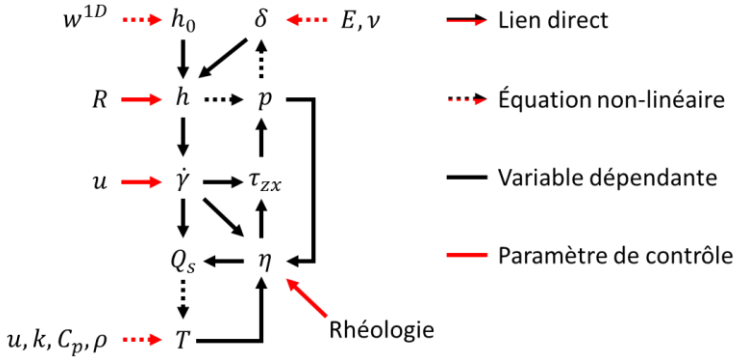

Figure i-12 – Différents liens entre les paramètres de contrôle et les variables dépendantes dans les contacts à vitesse d'entrainement nulle.

Pour conclure, le fluide au centre du contact se réchauffe à cause du fort cisaillement. Les surfaces en mouvement entraînent le fluide chaud en dehors du contact, ce qui induit des différences de température dans l'épaisseur, et par extension, de viscosité. Ces dernières sont amplifiées au centre du contact où la pression est plus élevée. C'est donc plus proche du centre du contact (comparé au contact de Hertz) que se trouve la plus forte génération de

pression. Afin de respecter l'équilibre de la charge, cela conduit à de fortes pressions centrales, responsables d'un fort déplacement élastique central, expliquant la forme particulière de ces contacts.

Influence des conditions opératoires

Le lien complexe entre les paramètres de contrôle et l'état du système a été établi. L'étude duale numérique/expérimentale permet d'apprécier les effets de certains de ces paramètres de contrôle. Dans un premier temps, l'influence de la vitesse sur l'épaisseur minimale de film est étudiée, pour une charge $w^{2D} = 50\ N$ (ce qui correspond à $w^{1D} = 58\ kN.m^{-1}$) et une température extérieure $T_0 = 293{,}15\ K$. Les variations des valeurs numériques et expérimentales des épaisseurs centrales et minimales de film sont tracées sur la Figure i-13.

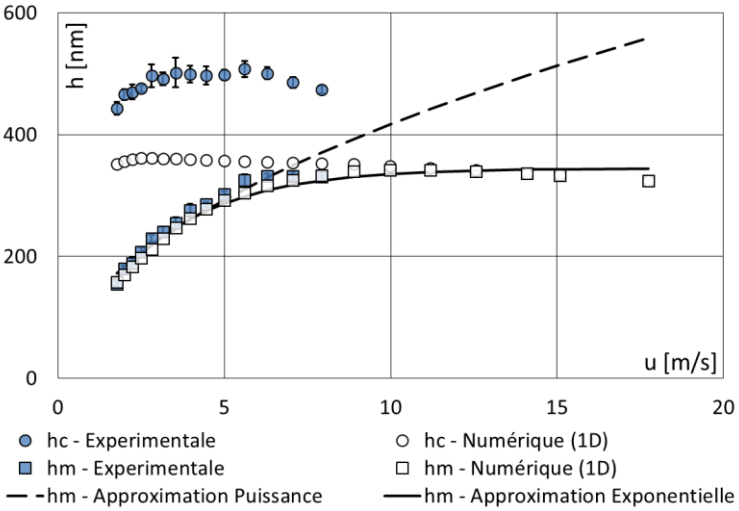

Figure i-13 – Variation de l'épaisseur centrale et minimale de film avec la vitesse, $w^{1D} = 5{,}82 \times 10^4\ N.m^{-1}$ et $T_0 = 293{,}15\ K$. Trois fois l'écart type est indiqué en noir pour les résultats expérimentaux.

Il existe entre $0{,}3\%$ et $11{,}6\%$ d'écart sur les valeurs d'épaisseur minimale de film. Les résultats montrent une croissance de l'épaisseur minimale de film avec la vitesse, jusqu'à environ $u = 10\ m/s$ où un plateau maximal est atteint. La différence de température entre le disque en saphir et le tonneau en acier est représentée sur la Figure i-14.

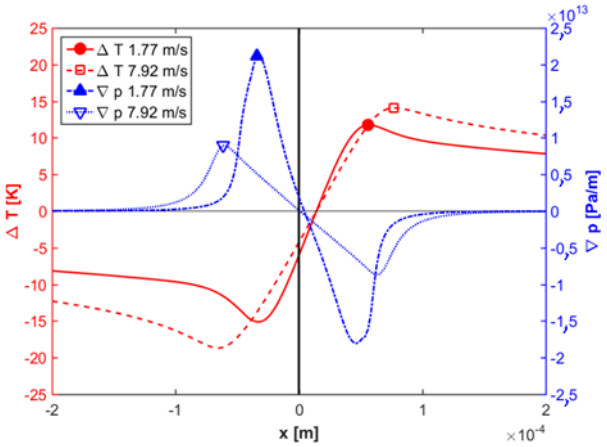

Figure i-14 – Différences de température (en rouge, axe de gauche) entre les deux interfaces et gradient de pression (en bleu, axe de droite) dans le fluide à $w^{1D} = 5{,}82 \times 10^4\ N.m^{-1}$ et $T_0 = 293{,}15\ K$, pour deux vitesses différentes.

Pour $u = 1{,}77\ m.s^{-1}$ et $u = 7{,}92\ m.s^{-1}$, la différence maximale de température se trouve à $x = -34\ \mu m$ et $x = -65\ \mu m$ respectivement. Cela s'explique par une augmentation du terme de convection dans l'équation de l'énergie. Ainsi, le gradient maximal de pression se trouve plus éloigné du centre à grande vitesse. A $1{,}77\ m.s^{-1}$ le maximum se situe à $x = -34\ \mu m$, tandis qu'à $7{,}92\ m.s^{-1}$ il se trouve à $x = -62\ \mu m$. L'augmentation de l'épaisseur de film est donc liée à une génération plus étendue de pression. Afin de décrire le plateau observé à hautes vitesses, l'approximation suivante est introduite (eq. i-16).

$$h_{m,sa} = h^u_{m,sa} \times (1 - \exp(-u/u^u_{m,sa})) \qquad \textit{eq. i-16}$$

avec $h^u_{m,sa} = 345\ nm$ et $u^u_{m,sa} = 2{,}8\ m.s^{-1}$, qui représentent respectivement le plateau à haute vitesse et l'inverse de la constante de décroissance exponentielle. Ces valeurs dépendent des autres paramètres du système. Ainsi, une description plus complète demanderait une étude paramétrique beaucoup plus large. La différence relative maximum entre cette formule et les résultats numériques est de $5{,}7\%$. Pour les résultats expérimentaux, cette différence relative maximale est de $8{,}2\%$.

L'influence de la vitesse sur l'épaisseur minimale de film est représentée sur la Figure i-15 pour trois différentes charges.

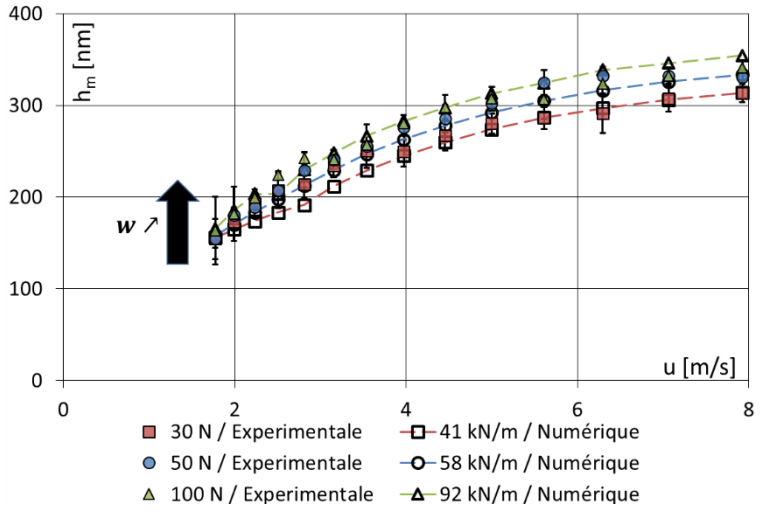

Figure i-15 – Variation de l'épaisseur minimale de film avec la vitesse pour différentes charges à $T_0 = 293{,}15\ K$. Trois fois l'écart type est indiqué en noir pour les résultats expérimentaux.

La différence relative entre les résultats numériques et expérimentaux est entre $0{,}3\%$ et $15{,}5\%$. Une augmentation de la charge conduit à une légère augmentation de l'épaisseur minimale de film. Ce comportement diffère de celui observé en roulement/glissement. Il est possible de compléter la formule de prédiction précédemment établie, en incluant la dépendance de $h^u_{m,sa}$ et $u^u_{m,sa}$ avec la charge. Des calculs complémentaires permettent d'étendre le cadre d'étude. La variation de $h^u_{m,sa}$ et $u^u_{m,sa}$ avec la charge est tracée dans la Figure i-16.

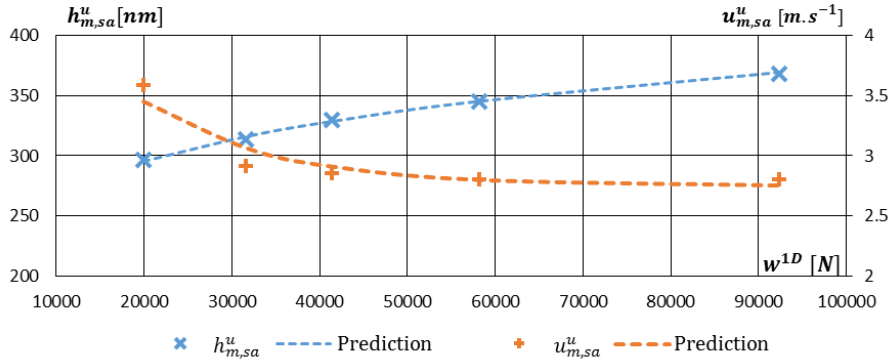

Figure i-16 – Valeurs de $h^u_{m,sa}$ et $u^u_{m,sa}$ en fonction de la charge.

La formule semi-analytique prenant en compte l'influence de la charge et de la vitesse est donnée dans les eq. i-17 à eq. i-18.

$$h^u_{m,sa} = h^{u,w}_{m,sa} \times (w^{1D})^{\alpha^{u,w}_{m,sa}} \qquad \textit{eq. i-17}$$

$$u^u_{m,sa} = u^{u,w}_{m,sa} \times \left(1 + \exp\left(-\frac{w^{1D}}{w^{u,w}_{m,sa}}\right)\right) \qquad \textit{eq. i-18}$$

avec w^{1D} en $N.m^{-1}$. De plus, $h^{u,w}_{m,sa} = 69{,}8\ nm$, $\alpha^{u,w}_{m,sa} = 0{,}146$, $u^{u,w}_{m,sa} = 2{,}74\ m.s^{-1}$ et $w^{u,w}_{m,sa} = 14695\ N.m^{-1}$. Le modèle est confronté aux résultats numériques et expérimentaux dans la Figure i-18.

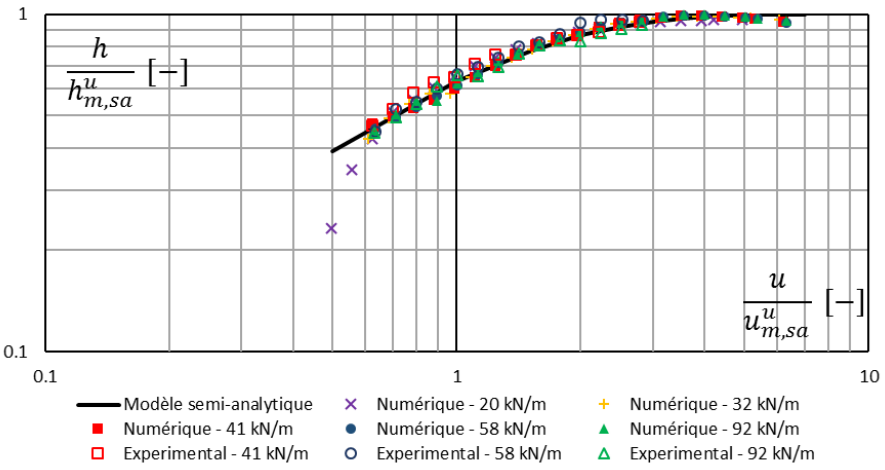

Figure i-17 – Ratio de l'épaisseur de film sur $h^u_{m,sa}$ en fonction du ratio de la vitesse sur $u^u_{m,sa}$.

Le coefficient de détermination pour le jeu de données expérimentales est ${R_d}^2 = 0{,}96$. Il est ${R_d}^2 = 0{,}98$ pour le jeu de données numériques. Il est important de noter le fait que cette formule a été établie avec le lubrifiant Shell T9, pour deux surfaces en acier, avec $R^{1D}_{eq} = 0{,}0128\ m$ et $T_0 = 293{,}15\ K$.

Le dispositif expérimental permet aussi d'étudier l'influence de la température externe sur l'épaisseur minimale de film. Les valeurs sont représentées sur la Figure i-18 pour trois températures externes ($T_0 \in \{293{,}15; 308{,}15; 323{,}15\}\ K$).

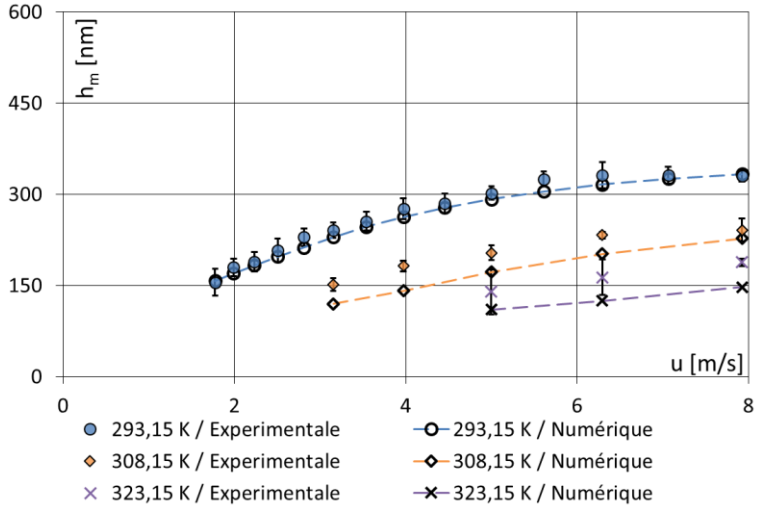

Figure i-18 – Variation de l'épaisseur minimale de film avec la vitesse pour différentes charges à $w^{1D} = 5{,}82 \times 10^4\ N.m^{-1}$. *Trois fois l'écart type est indiqué en noir pour les résultats expérimentaux.*

Pour chaque valeur de température, la différence relative maximale entre la prédiction du modèle et la valeur mesurée est de $11{,}6\%$, $22{,}2\%$ et $23{,}5\%$ respectivement. La diminution de l'épaisseur minimale de film s'explique par la présence de gradients de température moins importants.

En conclusion, le modèle permet de comprendre les liens entre les différentes variables du système et donc d'expliquer le phénomène de « *viscosity wedge* ». Une approche duale numérique/expérimentale permet d'apprécier l'influence de la vitesse, de la charge et de la température externe sur l'épaisseur minimale de film. Une augmentation de la vitesse provoque une augmentation de l'épaisseur de film minimale, jusqu'à un plateau. Par ailleurs, une augmentation de la charge provoque une faible augmentation de cette épaisseur. Enfin, une augmentation de la température externe provoque la diminution de l'épaisseur de film. Une approximation de l'épaisseur minimale de film est donnée par une formule semi-analytique reproduisant le plateau à fortes vitesses.

4. Contacts à vitesse d'entrainement nulle soumis à une variation de chargement

Comme vu précédemment, l'effet de *« viscosity wedge »* n'est pas le seul permettant d'expliquer la présence d'un film séparateur à Vitesse d'Entrainement Nulle. L'effet de *« squeeze »* est donc étudié dans ce chapitre. Après avoir décrit le cadre d'étude, il convient d'étudier les effets de *« viscosity wedge »* et de *« squeeze »* indépendamment, avant de s'attacher au comportement du contact lorsque les deux effets sont considérés.

Le contact étudié suppose deux solides en acier séparés par le lubrifiant Shell T9 (voir Tableau i-1 et

$C_{pf}\ [J.kg^{-1}.K^{-1}]$	1900	C_2	14.1596
$k_f\ [W.m^{-1}.K^{-1}]$	0.118	A_1	188.95
$\rho_R\ [kg.m^{-3}]$	872	$A_2\ [Pa^{-1}]$	0.533×10^{-9}
$T_R\ [K]$	298	$B_1\ [Pa^{-1}]$	7.37×10^{-9}
$K_{00}\ [Pa]$	9.234×10^{9}	B_2	-0.6171
$K_M{}'$	10.545	$T_{g0}\ [K]$	204.68
$a_v\ [K^{-1}]$	7.734×10^{-4}	$p_0\ [Pa]$	0
$\beta_k\ [K^{-1}]$	6.09×10^{-3}	a_{CY}	5
$\eta_g\ [Pa.s]$	1×10^{12}	n_{CY}	0.35
C_1	15.9035	$G_{CY}\ [Pa]$	7×10^{6}

Tableau i-2). L'inertie des solides en contact n'est pas considérée. De plus, le contact est contrôlé en faisant varier la charge linéairement, comme décrit dans l'eq. i-19. Le reste des données est présent dans le Tableau i-4.

$$\frac{w^{1D}(t)}{w_f^{1D}} = \begin{cases} 0{,}67 \times 10^{-3} + (1 - 0{,}67 \times 10^{-3})\dfrac{t}{t_{Loading}} & \text{pour } t < t_{Loading} \\ 1 & \text{pour } t_{Loading} \leq t < t_{Final} \end{cases} \qquad \textit{eq. i-19}$$

avec $t_{Final} = 100 \times t_{Loading}$ choisit de sorte que l'état quasi-statique soit atteint dans tous les cas de calcul, et $t_{Loading}$ le temps de chargement.

$u\ [m.s^{-1}]$	$R_{eq}^{1D}\ [m]$	$T_0\ [K]$	$w_f^{1D}\ [N.m^{-1}]$
3	0,02	293,15	100000

Tableau i-4 – Conditions opératoires.

Trois cas de calculs sont conduits selon la prise en compte ou non des effets de *« viscosity wedge »* et de *« squeeze »* voir (Tableau i-5).

	Cas A : Stationnaire thermique	Cas B : Transitoire isotherme	Cas C : Transitoire thermique
Effet thermique	X		X
Effet transitoire		X	X

Tableau i-5 – Hypothèses sur le modèle pour chaque cas de calcul.

A chaque instant correspond une charge $w^{1D}(t)$. Il est possible de représenter les variables en fonction du temps. De nouvelles notations sont introduites pour distinguer les cas. L'exposant correspondant au cas étudié est donc utilisé. Par exemple, $h_m^A(t)$ désigne la valeur instantanée de l'épaisseur minimale de film dans le cas A. De plus, $h_{m,min}^A$ se réfère à la valeur minimale de l'épaisseur minimale de film au cours du temps. Un temps thermique

caractéristique est également introduit. Il correspond à la définition faite par Raisin *et al.*[20] (initialement fonction des caractéristiques thermiques des matériaux en contact, il est montré que ce temps peut être simplifié pour ne plus dépendre de ces caractéristiques thermiques) et donnée dans l'eq. i-20. Le ratio $\bar{t_T} = t_T/t_{Loading}$ représente l'influence relative des effets thermiques par rapport à l'effet de *« squeeze »*.

$$t_T = \frac{a_f^{1D}}{u} = 0{,}07\ ms \qquad \textit{eq. i-20}$$

$$\bar{t} = \frac{t}{t_{Loading}} \qquad \textit{eq. i-21}$$

Dans les cas A et C, l'état initial correspond à la charge $w_i^{1D} = 0{,}67 \times 10^{-3} \times w_f^{1D}$. Cela permet d'avoir une répartition de température quasiment uniforme (augmentation maximale de $1.1K$) ainsi que des déplacements élastiques des surfaces négligeables ($\delta_{h_m}^A(0) = \delta_{h_m}^C(0) = 2\ nm$). Dans ce cas, $h_m^A(0) = h_m^C(0) = 529\ nm$. Dans le cas B, l'état initial est défini en fixant simplement la séparation rigide initiale à $h_0^B(0) = 527\ nm$.

- *Cas A : Etude stationnaire thermique*

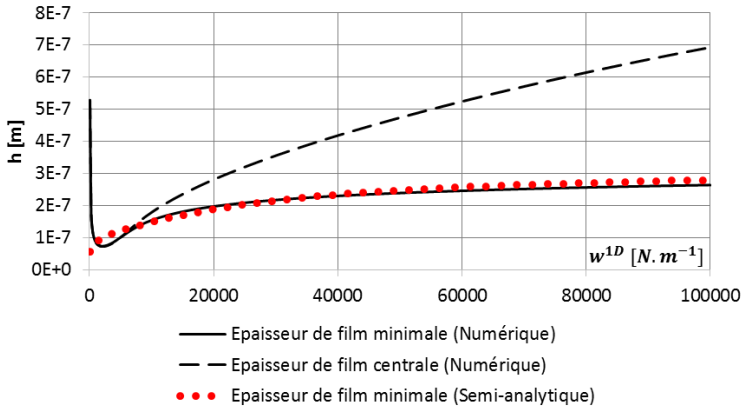

Figure i-19 – Variation de l'épaisseur de film avec la charge pour toutes les charges considérées.

L'évolution de l'épaisseur minimale et centrale de film est représentée sur la Figure i-19. Pour les charges inférieures à $w^{1D} = 2065{,}7\ N.m^{-1}$, l'épaisseur de film diminue. Cela est uniquement dû à une diminution de la séparation rigide des solides h_0. Le faible déplacement élastique, ainsi que la valeur positive de h_0 sont des éléments qui indiquent que le contact est en régime hydrodynamique. Pour les charges supérieures à $w^{1D} = 2065{,}7\ N.m^{-1}$, le contact se comporte de la même façon que ce qui a été vu dans l'étude précédente en conditions stationnaires.

- *Cas B : Etude transitoire isotherme*

La contribution des effets de squeeze seuls sont étudiés en utilisant la littérature comme référence. Dowson et Wang[31] ont étudié la variation de l'épaisseur minimale et centrale de film et pour un solide lâché à une hauteur donnée. Durant le rapprochement des corps, une

quantité de fluide est piégée au sein du contact, ce qui se traduit par une stagnation de l'épaisseur centrale de film. L'épaisseur de film minimale continue à décroitre vers 0.

La formule prédictive de Wang, Venner et Lubrecht[32] permet de prédire la valeur de l'épaisseur centrale de film lorsqu'elle atteint son plateau. Afin de l'utiliser, il faut adapter la définition de certains de ces termes. Tout d'abord, le coefficient réciproque asymptotique de pression-viscosité α^* est mis en œuvre afin de permettre l'utilisation du modèle WLF[33]. Les valeurs $a^{1D}(\bar{t}=1)$, $w^{1D}(\bar{t}=1)$ et $p_h^{1D}(\bar{t}=1)$ sont utilisées à la place des valeurs maximales données par Wang et al.[32] (b^*, w_1^* and p_h^*). Le modèle adapté (exposant $Wang^*$) s'écrit alors comme dans l'eq. i-23.

$a^{1D}(\bar{t}=1)\ [m]$	$p_h^{1D}(\bar{t}=1)\ [Pa]$	$\eta_0\ [Pa.s]$	$\alpha^*\ [Pa^{-1}]$
$1{,}05 \times 10^{-4}$	$6{,}06 \times 10^{8}$	0,0195	$2{,}36 \times 10^{-8}$

Tableau i-6 – Paramètres employés dans la formule de remplacement inspirée par Wang et al.[32] *pour le cas B.*

$$M = \pi \left(\frac{3}{4\lambda^*}\right)^{1/2}$$

$$L = \alpha^* p_{h,f}^{1D} \left(\frac{4\lambda^*}{3}\right)^{1/4} \qquad \textit{eq. i-22}$$

$$\frac{h_c^{Wang^*}(\bar{t}=1)}{R_{eq}^{1D} \times (U_{DH})^{1/2}} = 2.3 \times M^{0,2} \times L^{0,55} \qquad \textit{eq. i-23}$$

avec $U_{DH} = \frac{1}{2}\left(\frac{L}{\alpha^* E'}\right)^4$ et $\lambda^* = \frac{12\eta_0 {R_{eq}^{1D}}^2}{a_f^{1D} p_{h,f}^{1D} t_{Loading}}$

La Figure i-20 expose la variation de l'épaisseur centrale et minimale de film pour un temps de chargement $t_{Loading} = 1\ ms$.

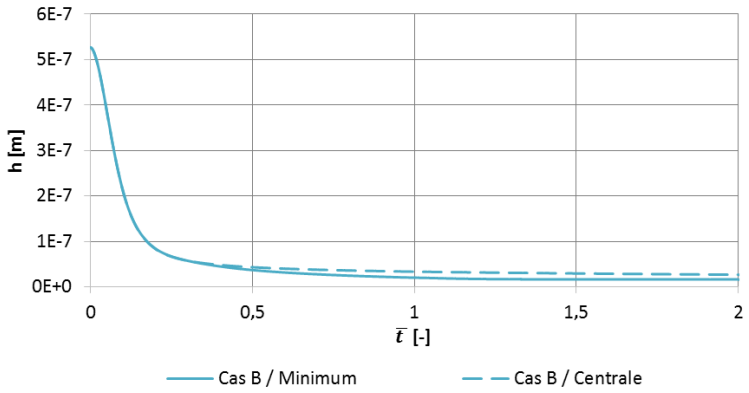

Figure i-20 – Variation de l'épaisseur centrale et minimale de film pour $t_{Loading} = 1\ ms$.

Comme vu précédemment, les deux grandeurs diminuent constamment. L'épaisseur centrale décroit beaucoup moins à partir d'un certain stade. La variation de l'épaisseur minimale de film pour différents temps de chargement est tracée dans la Figure i-21.

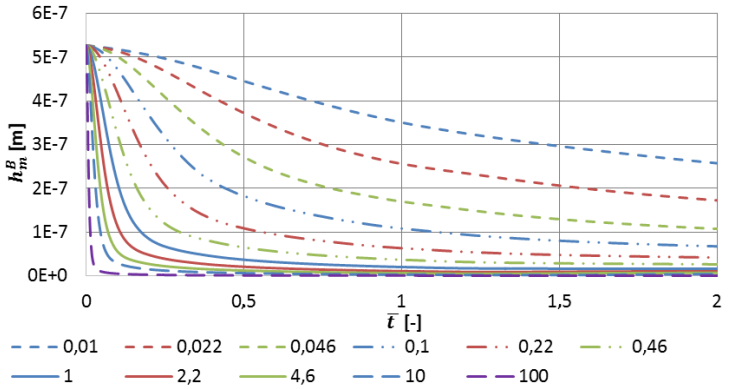

Figure i-21 – Variation de l'épaisseur minimale de film avec $\bar{t}$ dans le cas B pour toutes valeurs de $t_{Loading}$.

Dans tous les cas, l'épaisseur minimale de film diminue au cours du chargement. Pour chaque courbe, la charge maximale est atteinte à $\bar{t} = 1$. Pour $t_{Loading} = 0{,}01\ ms$, une diminution de l'épaisseur de film de $33{,}4\%$ est observée. Cette diminution est de $99{,}8\%$ pour $t_{Loading} = 100\ ms$. Cela montre dans quelle mesure l'effet de *« squeeze »* est plus important pour des temps de chargement courts. La pente nulle au début de chaque courbe correspond à une vitesse initiale verticale nulle.

Le Tableau i-7 contient les valeurs de $h_c^{Wang^*}(\bar{t} = 1)$ et $h_c^B(\bar{t} = 1)$ pour les différents temps de chargements considérés.

$t_{Loading}\ [ms]$	$h_c^{Wang^*}(\bar{t} = 1)\ [nm]$	$h_c^B(\bar{t} = 1)\ [nm]$	Différence relative
0,01	404,6	351,0	13,3%
0,022	264,8	256,4	3,2%
0,046	178,2	172,4	3,2%
0,1	117,4	117,5	0,1%
0,22	76,8	76,3	0,6%
0,46	51,7	51,1	1,2%
1	34,0	34,1	0,2%
2,2	22,3	23,0	3,3%
4,6	15,0	15,6	3,9%
10	9,9	10,5	6,4%
100	2,9	3,2	13,0%

Tableau i-7 – Valeurs adaptées de l'épaisseur centrale (Wang et al [32]*) compares aux valeurs obtenues par le modèle dans le cas B, pour différents temps de chargement.*

Pour $0{,}046\ ms < t_{Loading} < 4{,}6\ ms$, l'erreur relative entre la formule prédictive et le modèle est inférieure à 4%, ce qui est une indication de la précision du modèle présenté.

- *Cas C : Compétition entre effets thermiques et de squeeze*

Les variation de l'épaisseur centrale et minimale de film dans les cas A, B et C sont représentées dans la Figure i-22 pour le temps de chargement $t_{Loading} = 1\ ms$.

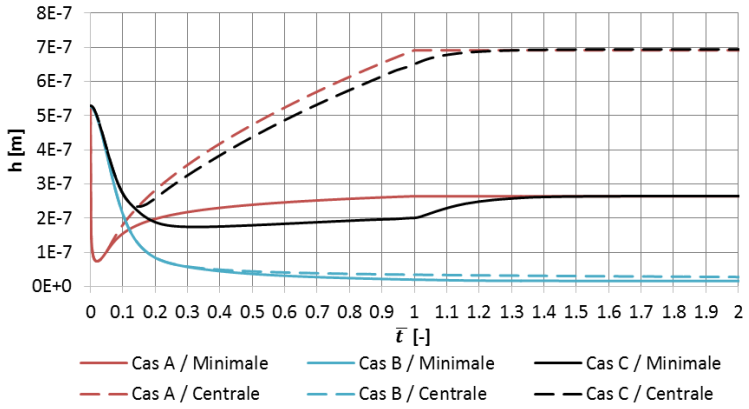

Figure i-22 – Variation de l'épaisseur centrale et minimale de film dans les cas A, B and C, en fonction de $\bar{t}$. La charge maximale est atteinte à $\bar{t} = 1$.

Au début du chargement, l'épaisseur de film diminue rapidement dans le cas A (ce qui correspond au régime hydrodynamique), tandis que la variation dans le cas C est très similaire à la variation dans le cas B. L'effet de *« squeeze »* est la raison principale permettant à l'épaisseur de film de rester suffisamment élevée au début du chargement. A partir de $\bar{t} = \bar{t_T} = 0{,}07$, l'épaisseur de film dans le cas C diminue plus lentement que dans le cas B, ce qui indique l'apparition d'effets thermiques non-négligeables. A ce stade, une augmentation de la charge correspond à une augmentation de l'épaisseur de film dans le cadre stationnaire. Le minimum temporel de l'épaisseur minimale de film ($h^C_{m,min} = 175\ nm$) est atteint à $\bar{t} = 0{,}372$ dans le cas C. A noter $h^C_{m,min}/h^A_{m,min} = 2{,}35$. De là, l'épaisseur centrale et minimale de film augmentent jusqu'à ce que la charge maximale soit atteinte. L'état quasi-statique est atteint à $\bar{t} = 1{,}368$. La discontinuité observée à $\bar{t} = 1$ correspond à l'arrêt brutal du chargement.

Par la suite, l'effet du temps de chargement sur le contact est étudié.

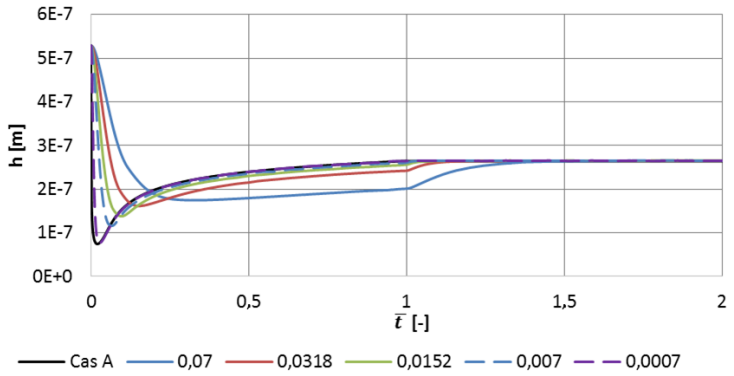

Figure i-23 – Variation de l'épaisseur minimale de film dans les cas A et C, pour $\bar{t_T} = \{0{,}0007;\ 0{,}007;\ 0{,}0152;\ 0{,}0318;\ 0{,}07\}$, en fonction de $\bar{t}$.

Pour les chargements extrêmement lents ($t_{Loading} = \{10, 100\}\ ms$ soit $\bar{t_T} < 0{,}007$), le temps thermique est très petit devant le temps de chargement, ce qui signifie que le contact se comporte rapidement comme leas stationnaire (voir Figure i-23). C'est pourquoi plus le temps de chargement est élevé, plus $h^C_{m,min}$ est proche de $h^A_{m,min}$. Pour les chargements un peu moins lents ($t_{Loading} = \{1;\ 2{,}2;\ 4{,}6\}\ ms$) ce qui correspond à $\bar{t_T} = \{0{,}0152;\ 0{,}0318;\ 0{,}07\}$,

l'effet de squeeze est un peu plus important et permet de soutenir le film durant la phase initiale du chargement. Cela permet d'assurer un minimum d'épaisseur minimale de film plus élevé.

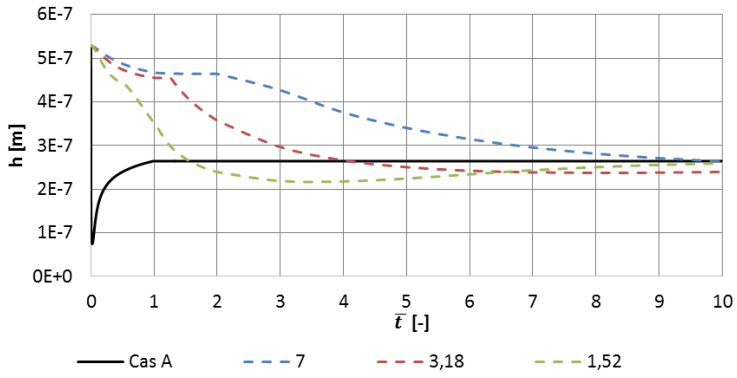

Figure i-24 – Variation de l'épaisseur minimale de film dans les cas A et C, pour $\bar{t_T} = \{1{,}52;\ 3{,}18;\ 7\}$, en fonction de $\bar{t}$.

Pour les chargements rapides, ($t_{Loading} = \{0{,}01;\ 0{,}022;\ 0{,}046\}\ ms$ ce qui correspond à $\bar{t_T} > 1{,}52$), l'effet de *« squeeze »* est tellement proéminent que durant l'augmentation de la charge, l'épaisseur minimale de film dans le cas C est supérieure à celle obtenue dans le cas A. En revanche, le temps caractéristique thermique est très élevé devant le temps de chargement ($\bar{t_T} = 1{,}52$ pour $t_{Loading} = 0{,}046\ ms$), ce qui provoque une apparition relativement tardive de l'effet thermique. C'est pourquoi l'épaisseur de film diminue bien après que la charge maximale soit atteinte, avec une valeur minimale obtenue à $\bar{t} = 3{,}96$. Dans ces cas, une discontinuité très forte est observée en début de chargement. Elle correspond au moment où le minimum de l'épaisseur de film se distingue de l'épaisseur centrale.

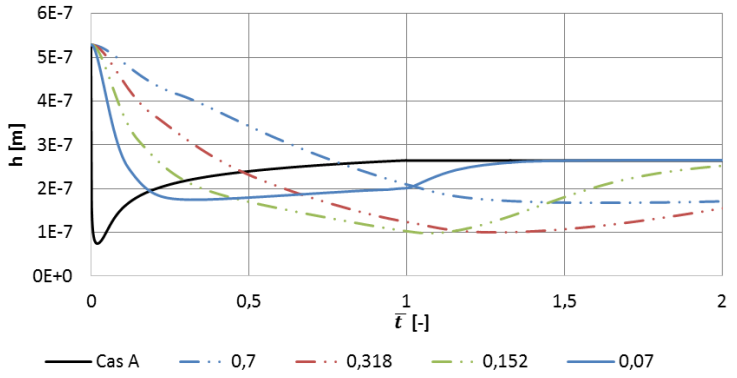

Figure i-25 – Variation de l'épaisseur minimale de film dans les cas A et C, pour $\bar{t_T} = \{0{,}07;\ 0{,}152;\ 0{,}318;\ 0{,}7\}$, en fonction de $\bar{t}$.

Pour des vitesses de chargement modérées ($t_{Loading} = \{0{,}1;\ 0{,}22;\ 0{,}46\}\ ms$ ce qui correspond à $\bar{t_T} \in \{0{,}152;\ 0{,}318;\ 0{,}7\}$), l'effet de *« squeeze »* est toujours présent. Cependant, il ne permet pas d'assurer une séparation suffisante pour la totalité du chargement. De plus, les effets thermiques apparaissent tardivement. Cela conduit à $h^C_{m,min}/h^A_{m,min} \approx 1$.

Le ratio $h^C_{m,min}/h^A_{m,min}$ est représenté pour les différentes valeurs de $\overline{t_T} = t_T/t_{Loading}$ dans la Figure i-26 afin d'illustrer les trois types de chargements observés.

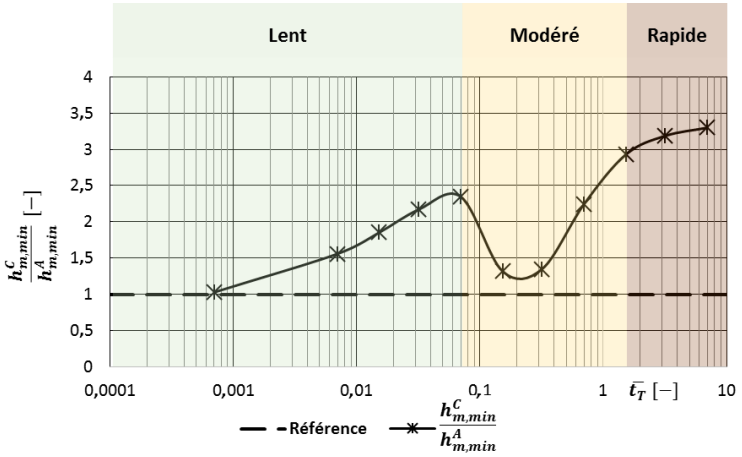

Figure i-26 – Ratio entre la valeur de l'épaisseur minimale dans le cas C sur la valeur dans le cas A, en fonction du ratio caractéristique t_T. La ligne horizontale marque la valeur de référence dans le cas A.

Conclusions générales et perspectives

Conclusion

Ce travail de thèse se focalise sur les contacts lubrifiés fortement chargés sous conditions de vitesse d'entrainement nulle. Ces contacts sont présents entre deux éléments roulants dans un roulement sans cage. Trois phénomènes peuvent expliquer une séparation des surfaces dans ce cas : le glissement aux parois, l'effet thermique de *« viscosity wedge »* et l'effet transitoire de *« squeeze »*. Dans le cas du contact acier-acier, seuls les deux derniers effets sont considérés.

Dans le Chapitre 2, les outils numériques et expérimentaux sont présentés, puis comparés. Le modèle de calcul par élément finis permet de déterminer simultanément la distribution de pression et de température dans le contact, ainsi que le déplacement élastique des surfaces. Le dispositif expérimental met en œuvre le tribomètre Jerotrib. L'utilisation d'une surface transparente en saphir est justifiée. Enfin, l'équivalence entre le modèle 1D et les essais est étudiée.

Dans le Chapitre 3, l'effet de *« viscosity wedge »* est étudié en conditions stationnaires. L'approche duale expérimentale/numérique permet de comprendre l'influence de la vitesse des surfaces, de la charge appliquée sur le contact et de la température externe. Une augmentation de la vitesse conduit à une augmentation de l'épaisseur minimale de film jusqu'à un plateau. Une augmentation de la charge conduit à une faible augmentation de l'épaisseur de film. Enfin, une augmentation de la température externe provoque une réduction de l'épaisseur de film. Une formule de prédiction est proposée pour approximer la variation de l'épaisseur minimale de film avec la vitesse et la charge. Dans les conditions d'études données, elle est en bon accord avec les résultats numériques et expérimentaux.

Les influences des effets de *« viscosity wedge »* et de *« squeeze »* sont compareés dans le Chapitre 4. La charge est variée linéairement d'une faible valeur vers une forte valeur. Un régime hydrodynamique est observé à faible charge dans le cas stationnaire. La transition vers le régime EHD marque la mesure d'une valeur minimale (au cours du temps) de l'épaisseur minimale de film. La prise en compte des deux effets permet d'augmenter la valeur de ce minimum Au début du chargement, l'effet de *« squeeze »* amortit considérablement la chute de l'épaisseur de film. A mesure que ce dernier effet s'estompe, l'apparition de gradients thermiques permet au *« viscosity wedge »* d'assurer une séparation pérenne des surfaces. Lorsque le ratio caractéristique thermique-transitoire est faible (chargement lent), l'effet de *« squeeze »* disparaît relativement vite durant le chargement. Le comportement du contact est alors majoritairement définit par la référence stationnaire. Dans ces conditions, un chargement plus rapide est bénéfique car cela permet un effet de *« squeeze »* plus important sans délai important de l'apparition des effets thermiques. Pour des chargements très rapides, l'effet de *« squeeze »* est bénéfique pour la totalité de la phase de chargement, ce qui permet une apparition tardive du *« viscosity wedge »*. Enfin, pour des chargements à vitesse modérée, l'effet de *« squeeze »* perd son efficacité avant que des gradients de température suffisants

aient pu apparaître. Cela conduit à une faible valeur minimale (au cours du temps) de l'épaisseur minimale de film.

Ce travail s'inscrit dans un contexte global où l'amélioration de la durée de vie des composants est cruciale. Les processus physiques expliquant la séparation des surfaces sont étudiés en détail. Cette démarche permet aux concepteurs de roulements sans cage de mettre en œuvre des techniques de prédiction du comportement des contacts entre éléments roulants.

Perspectives

Dans ce mémoire de thèse, les résultats présentés se reposent sur des expériences menées spécifiquement à cette fin. Cela permet une validation quantitative du modèle. Une première tentative de prédiction d'épaisseur minimale de film est faite. Cependant, seuls une huile, une géométrie et un couple de matériaux solides sont pris en compte. Des expérimentations approfondies avec une plus grande variété des paramètres de contrôle permettraient d'obtenir les données nécessaires pour la mise en place d'une formule de prédiction globale.

L'analyse faite sur les effets de *« squeeze »* et de *« viscosity wedge »* est une première tentative de description du comportement d'un roulement sans cage. La condition de vitesse d'entrainement nulle est considérée durant toute l'étude. En réalité, le comportement cinématique des roulements sans cages peut permettre l'apparition d'une faible vitesse d'entrainement. De plus, la variation de la charge est supposée linéaire, et la masse des solides ignorée. En utilisant les résultats donnés ici comme base de travail, un modèle complet couplant la dynamique d'ensemble d'un roulement et le comportement multi-physique des contacts lubrifiés permettrait d'améliorer la prédiction du comportement de ces composants.

General introduction

Mechanical contacts are omnipresent in our environment: between a tyre and the road, between two teeth in a set of gears, or in the various moving joints of the body. To protect the surfaces from wear and reduce energy losses, a fluid is often placed at the interface between the contacting bodies.

The classical phenomenon explaining lubricant film build-up in this so-called lubricated contact is the hydrodynamic entrapment of the fluid in the converging inlet, due to the adherence of the lubricant to the moving surfaces. In such contact, the lubricant is able to bear the load and separate the surfaces. The design of the majority of highly loaded lubricated contacts rely on semi-analytical formulae derived under rolling conditions. They are tied to the mean entrainment velocity of the fluid, which is itself defined as the average of the tangential velocities of both surfaces.

This work proposes a study of highly loaded lubricated contacts in which the two surfaces are moving at the same velocity, but in opposite directions, corresponding to a Zero Entrainment Velocity (ZEV) condition. A number of applications can function under such condition, with some of them showing good performance and little surface damage. This suggests the existence of a lubricant film despite the absence of the entrainment phenomenon. Yet, the physical origin of this film is unclear and design tools for such contacts are lacking. The objective of this work is then to shed light on the physics at stake in highly loaded lubricated contacts under Zero Entrainment Velocity condition. This can lead to the initiation of a quantitative prediction of the film thickness. This work, based on numerical modelling, will also present a number of experimental validations.

The main principles of lubrication are presented in Chapter 1. Particularly, elastohydrodynamic lubricated (EHL) contacts are detailed. Then, the physical phenomena found in the literature that could explain the origin of a film thickness formation under Zero Entrainment Velocity (ZEV) condition are presented. As such, a focus is made on transient (squeeze) and thermal effects.

Chapter 2 introduces the finite element model. It incorporates the rheology of the lubricant as well as the thermomechanical properties of the materials. A thermal and transient analysis is conducted. Moreover, a dedicated experimental procedure for the model validation is presented. From this, multiple model hypotheses are discussed.

Chapter 3 focusses on stationary ZEV contacts as part of a thermal analysis. The strong couplings between several mechanisms explain the load bearing capacity. Then the influence

of the operating conditions on the film thickness is presented. This includes the surface velocities, the applied normal load as well as the external temperature of the solids and fluid.

Chapter 4 shows the relative influence of squeeze and thermal effects on the film thickness. Each effect is studied independently. Then, the combined influence of both effects is investigated.

This document concludes with a summary of the presented results. Some prospects for future research are proposed.

Chapter 1. Introduction

1.1 History of the lubricated contact 42

1.2 Hertz theory 44

1.3 Elastohydrodynamic lubrication in rolling contacts: illustration on rolling element bearings 46

1.4 Other mechanisms for a load bearing capacity 50

1.4.1 Thermal effect: viscosity wedge 51

1.4.2 Transient effect: squeeze 52

1.4.3 Wall slip 55

1.5 Objectives and methodology 55

In this chapter, the historical context of lubricated contacts and their use are first presented. Then, the focus is put on highly loaded contacts, which corresponds to the elastohydrodynamic lubrication regime. Finally, the phenomena behind the generation of film thicknesses through thermal and squeeze effects are introduced.

1.1 History of the lubricated contact

Lubrication aims to reduce the energy losses (friction) and control the lifetime of mechanical systems by avoiding wear. The main principle is to entrain a lubricant (often a fluid or a grease) between the contacting bodies. This technique can be found in many industrial applications (engines[34], compressors[35], bearings[36]...), everyday products (bicycle or motorcycle chain[37]...) or even biological mechanisms (joints[38], mucous membranes[39]...). An example of the efficiency, simplicity and longevity of this principle can be illustrated by how animal fats were applied on rotating parts such as chariot wheel rods by Hittites to reduce friction and increase the life of their equipment[40]. Because the fluid is moving between the surfaces, it can carry heat in and out of the contact, thus regulating the temperature of the solids[41].

Figure 1.1-1 is an illustration of two surfaces moving relative to one another under a load w.

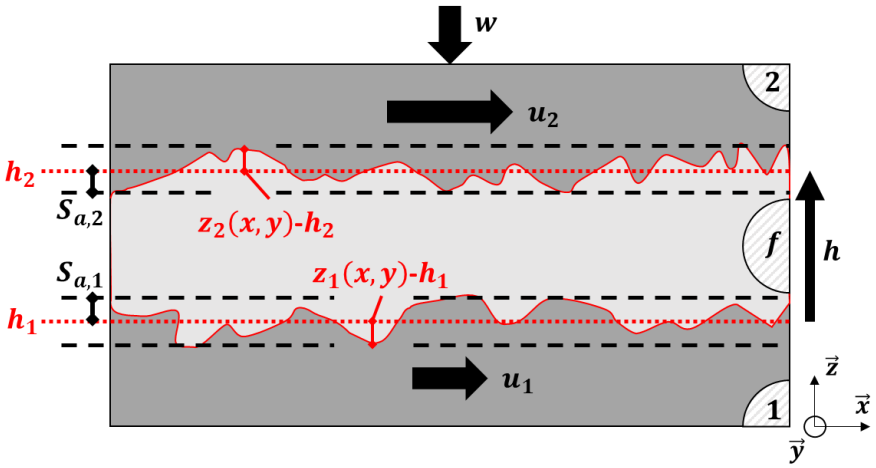

Figure 1.1-1 – Representation of a lubricated contact under a load w. Both contacting bodies are moving at velocities u_1 and u_2. The average distance separating them is the film thickness h. The surface roughness of each solid is $S_{a,i}$.

The bottom surface (subscript "1") is moving along the x-axis at a velocity u_1 and the top surface at a velocity u_2 (subscript "2"). The average value u_e, called the entrainment velocity, is defined in eq. 1.1-1.

$$u_e = \frac{u_1 + u_2}{2} \qquad \text{eq. 1.1-1}$$

Over a given area of measurement S, it is possible to define the average altitude of each surface h_i. From this definition, each solid has a surface roughness $S_{a,i}$ (see eq. 1.1-2).

$$S_{a,i} = \frac{1}{S}\iint_S |z_i(x,y) - h_i| dS \qquad \text{eq. 1.1-2}$$

Assuming that the contact is fully flooded with lubricant, the average distance h separating the surfaces is called the film thickness (see eq. 1.1-3).

$$h = h_2 - h_1 \qquad \textit{eq. 1.1-3}$$

The arithmetic average of the surface roughness is written S_a (see eq. 1.1-4):

$$S_a = \sqrt{{S_{a,1}}^2 + {S_{a,2}}^2} \qquad \textit{eq. 1.1-4}$$

Three lubrication regimes are defined in the Stribeck curve[42], represented in Figure 1.1-2(taken from ref. [1]):

- Boundary lubrication regime: a small or no film thickness separates the solid bodies. This leads to numerous direct surface-to-surface contacts, causing important friction and wear. The load is entirely supported by those direct contacts between solids;
- Mixed lubrication regime: a fluid film of a similar size as the surface asperities separates the solids. This leads to some surface-to-surface contacts along with some load bearing capacity of the fluid;
- Full film lubrication regime: a film thickness higher than the size of the surface asperities separates the solids. The lubricant fully bears the applied normal load.

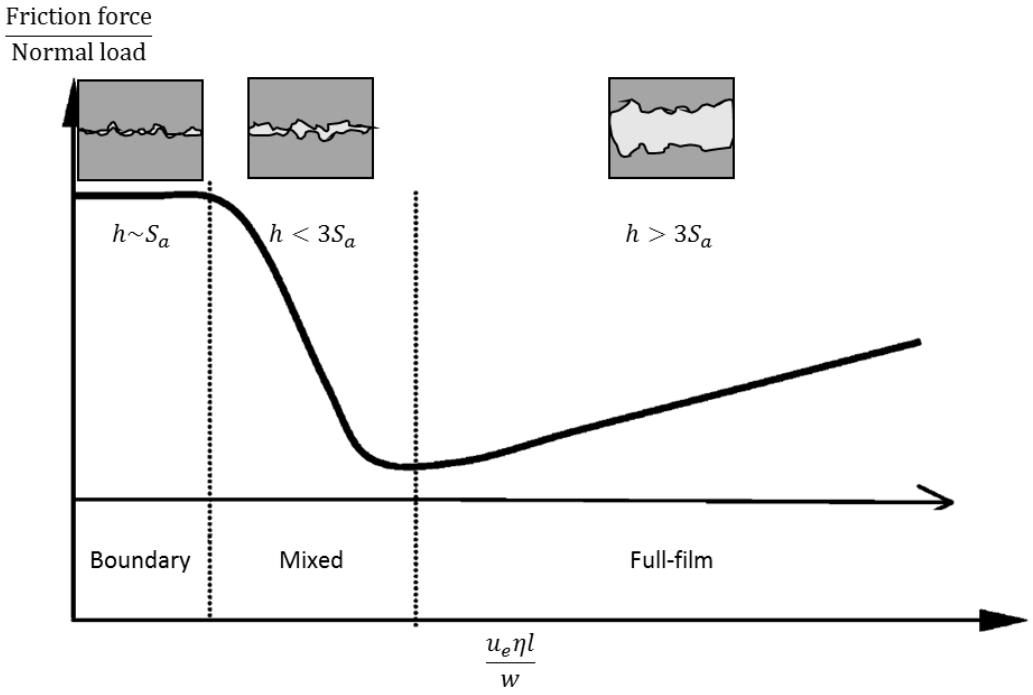

Figure 1.1-2 – Stribeck curve taken from [1]*, with η the fluid viscosity, w the normal load and l a characteristic length of the contact.*

The work presented in this document focusses on the full-film regime. Hirn[36] is the first to have studied the lubrication process in journal bearings. When mineral oils were first introduced in the industrial environment, Petrov[43] observed that the friction in applications was greatly reduced. He was the first one to systematically link friction with viscosity. This

work, alongside the work by Tower[44] proved that in some conditions, lubricated contacts were driven by hydrodynamics. To link the pressure in the lubricant with other parameters and variables in the contact, Reynolds[45] introduced the eponymous equation that has since then been widely used in lubrication theory. This subdomain of full-film lubrication where no elastic (or plastic) surface displacement is considered is commonly referred to as the hydrodynamic regime.

When Martin[2] and Gümbel[3] initially calculated film thicknesses between gears (which corresponds to concentrated or non-conforming contacts) that were assumed to be rigid, they found that the film thickness was lower than the surface roughness, which would indicate boundary or mixed lubrication. However, the surfaces of the gears in the corresponding applications were subjected to less wear than predicted, which was indicative of a larger film thickness. This meant that the elastic displacement of the surfaces had to be taken into account in the corresponding full-film lubrication studies. Ertel[4] in 1939, and Grubin and Vinogradova[5] ten years later presented results that not only assumed that the elastic displacement of the surfaces was that of a dry contact, but also that the viscosity varied with the pressure under the form of the Barus[46] pressure-viscosity law. These new considerations yielded increased theoretical values of film thickness far more fitting with the observations. This means that a full representation of highly loaded lubricated contacts needs to include both the elastic displacement of the surfaces and the hydrodynamic entrainment of fluid between them, along with the piezo-viscosity of the fluid. When the surface displacement is elastic, this type of full-film lubrication is referred to as elastohydrodynamic lubrication (EHL).

1.2 Hertz theory

The dry contact theory (as defined by Hertz[47]) is often chosen as a reference for EHL contacts. All surfaces are considered smooth. The Young's modulus and Poisson coefficients of both solids are E_1, E_2, v_1 and v_2. The material parameter E' is defined as in eq. 1.2-1. Figure 1.2-1 groups the three types of dry contact, classified by their geometries.

$$\frac{2}{E'} = \frac{(1-v_1)^2}{E_1} + \frac{(1-v_2)^2}{E_2} \qquad \textit{eq. 1.2-1}$$

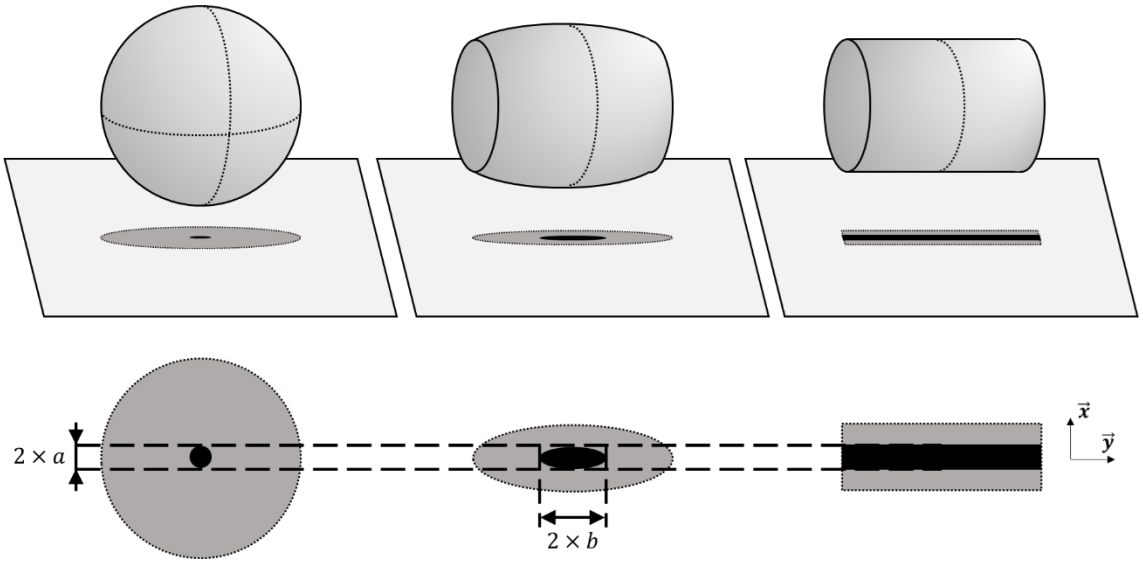

Figure 1.2-1 – The three types of basic geometries with the respective contact areas in black. On the left, the point contact between a sphere and a plane. In the middle, the wide point (elliptical) contact between a barrel and a plane. On the right, the line contact between a cylinder and a plane.

At the center of Figure 1.2-1 is the elliptic contact between a barrel and a plane, subjected to a load w^{2D}. The geometry is defined by the radii R_x^{2D} and R_y^{2D} of the barrel. If $R_y^{2D} > R_x^{2D}$, then the contact is considered wide. The geometrical ellipticity ratio $D = R_x^{2D}/R_y^{2D}$ is used to calculate the contact ellipticity ratio k_{ell} (eq. 1.2-2)[48].

$$k_{ell} \approx D^{\frac{2}{\pi}} \qquad \textit{eq. 1.2-2}$$

The equivalent radius of the contact R_{eq}^{2D} is calculated in eq. 1.2-3.

$$\frac{1}{R_{eq}^{2D}} = \frac{1}{R_x^{2D}} + \frac{1}{R_y^{2D}} \qquad \textit{eq. 1.2-3}$$

The contact region between the two solids is an ellipse of secondary radius b^{2D} (see eq. 1.2-4) and primary radius a^{2D} (see eq. 1.2-5).

$$b^{2D} = \left(\frac{6{k_{ell}}^2 \epsilon_{ell} w^{2D} R_{eq}^{2D}}{\pi E'}\right)^{1/3} \qquad \textit{eq. 1.2-4}$$

$$a^{2D} = \frac{b^{2D}}{k_{ell}} \qquad \textit{eq. 1.2-5}$$

where

$$\epsilon_{ell} \approx 1 + \frac{\frac{\pi}{2} - 1}{D} \qquad \textit{eq. 1.2-6}$$

The maximum pressure p_h^{2D} is defined in eq. 1.2-7.

$$p_h^{2D} = \frac{3w^{2D}}{2\pi a^{2D} b^{2D}} \qquad \textit{eq. 1.2-7}$$

The corresponding equation for the pressure profile is defined in eq. 1.2-8. When the contacting body is a sphere (on the left of Figure 1.2-1), then the problem is simplified ($R_y^{2D} = R_x^{2D}$, $D = k_{ell} = 1$ and $a^{2D} = b^{2D}$).

$$p_{h,f}^{2D}(x,y) = \begin{cases} p_h^{2D} \times \left(1 - \left(\frac{x}{a^{2D}}\right)^2 - \left(\frac{y}{b^{2D}}\right)^2\right)^{1/2} & \text{for } x^2 + y^2 < 1 \\ 0 & \text{elsewhere} \end{cases} \qquad \textit{eq. 1.2-8}$$

On the right in Figure 1.2-1 is the contact between an infinitely long cylinder of radius R^{1D} with a plane, under a load per unit length w^{1D}. The contact region is an infinitely long strip of width $2 \times a^{1D}$ (see eq. 1.2-9).

$$a^{1D} = \left(\frac{8w^{1D}R^{1D}}{\pi E'}\right)^{1/3} \qquad \textit{eq. 1.2-9}$$

Moreover, the solids are subjected to a parabolic pressure profile whose maximum value is the Hertz contact pressure p_h (see eq. 1.2-10 and eq. 1.2-11). The contact between a cylinder and a plane (or two cylinders) is referred to as a line contact or 1D contact.

$$p_h^{1D} = \frac{2w^{1D}}{\pi a^{1D}} \qquad \textit{eq. 1.2-10}$$

$$p_{h,f}^{1D}(x,y) = \begin{cases} p_h^{1D} \times \left(1 - \left(\frac{x}{a^{1D}}\right)^2\right)^{1/2} & \text{for } \left(\frac{x}{a^{1D}}\right)^2 < 1 \\ 0 & \text{elsewhere} \end{cases} \qquad \textit{eq. 1.2-11}$$

In the next section, the example of rolling contacts is described more precisely in order to define the main elements related to the study of lubricated contacts.

1.3 Elastohydrodynamic lubrication in rolling contacts: illustration on rolling element bearings

Similarly to gears, rolling element bearings include concentrated (non-conforming) contacts. They are used to illustrate EHL contacts. Figure 1.3-1 is a representation of the most basic type of cylinder roller bearing(CRB).

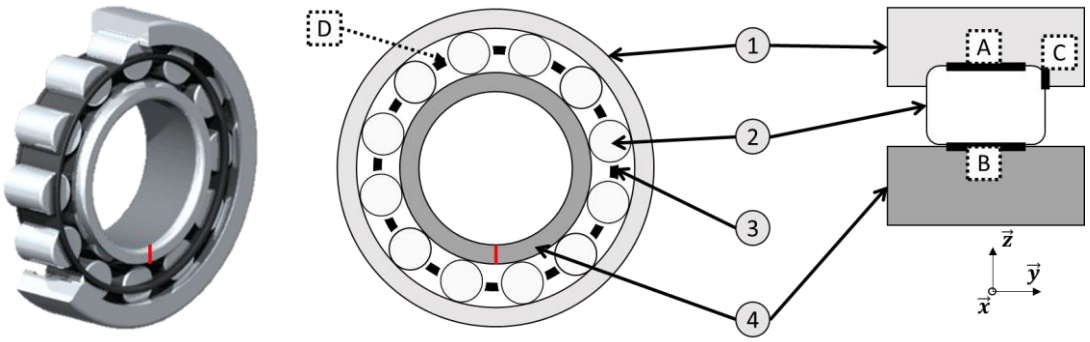

Figure 1.3-1 – On the left: Cylinder Roller Bearing. In the middle: Side view representation of the same bearing. On the right: Partial tangential view of the bearing near a rolling element.

It is comprised of four types of solids. The inner ring noted (4), the outer ring (1) and the rolling elements (2) serve to transmit loads while enabling energy efficient rotation. The last element is the cage (3). Its main function is to ensure that all rolling elements are separated and evenly distributed. Multiple zones of interest, where contact occurs, can be highlighted in those bearings. There is the non-conforming contact between the outer ring and the rolling element (A) and the non-conforming contact between the inner ring and the rolling element (B). The rings can be shaped so that the bases of the cylinders come into a conformal contact with them, thus keeping the rolling elements in the bearing and ensuring an axial load bearing capacity (C). This contact is called the roller/flange contact and has been studied by other authors ([49], [21]). More information on the cage on cylinder contact (D) can be found in [50].

When the contact between two bodies supports high loads (for example when the surfaces are non-conforming), extremely high pressures up to a few gigapascals are involved in the lubrication process[51]. In contact (B) (Figure 1.3-1), the two solids are rolling together. Assuming no slip, this means that their tangential velocities are the same. This case is referred to as pure rolling conditions ($u_e = u_1 = u_2 = u$). Figure 1.3-2 is a representation of the deformed, loaded and moving bodies and the separating film of lubricant.

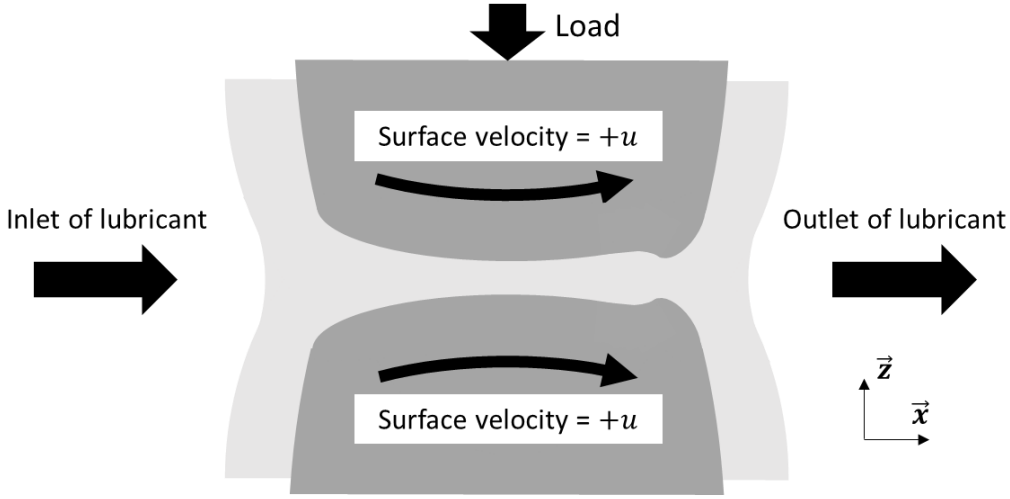

Figure 1.3-2 – Elastohydrodynamic line contact in pure rolling conditions.

The lubricant is entrained by the adhering surfaces before arriving to the pressurised contact area. The geometrical wedge created by the solids leads to the load bearing capacity of the

contact. This process is called the oil wedge. The film thickness (noted h) separating the solids can be determined through experiments which rely on either optical[25] or electrical conductivity[52] measurements. An interferogram corresponding to a point contact [53] is presented in Figure 1.3-3. It relies on interferometry principles[54], which links the colour composition of refracted light to film thickness. On the other hand, the quantitative prediction of friction([55], [56]) as well as in-situ pressure[57] and temperature([56], [58], [59]) measurements are still open topics of research.

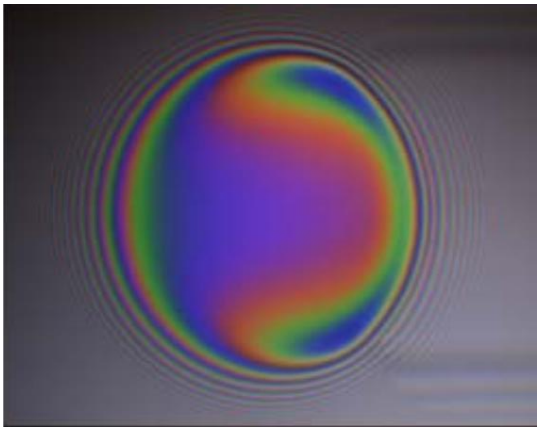

Figure 1.3-3 – Film thickness measurement through interferometry of the contact between a PMMA disc and a steel ball, lubricated with GTL8 ($10\ N$ *load, pure rolling and entrainment velocity of* $1.17\ m.s^{-1}$*) taken from* [53].

As a complement, numerical models can provide in-situ information. A result by Houpert and Hamrock[60] is represented in Figure 1.3-4.

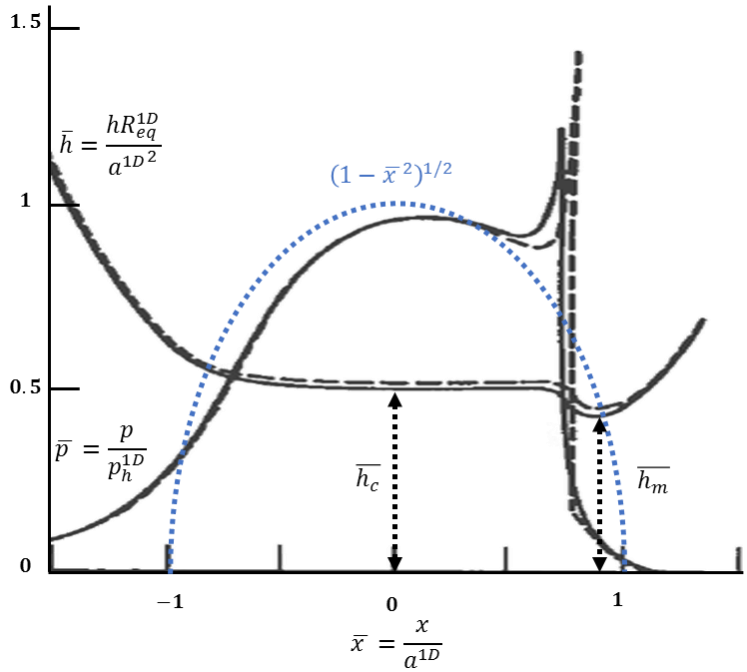

Figure 1.3-4 – Dimensionless pressure and film thickness profiles in an EHL contact (in black), taken from [60]. *The Hertz pressure profile, which corresponds to dry contacts, is also represented as a reference (in blue).*

It shows the variation of the dimensionless lubricant film thickness (noted $\bar{h}$) and pressure (noted $\bar{p}$) along the direction of sliding of the solids (noted $\bar{x}$). The dimensionless values are

defined by using the Hertz parameters previously introduced. Multiple specificities of EHL contacts can be noted on that Figure:

- The pressure profile of an EHL contact under rolling conditions is fairly close to the dry contact pressure (Hertz pressure) in most of the contact region;
- The fluid at the inlet of the contact (left side) sees a steady increase of pressure. This is commonly referred to as the pressure build-up;
- The film thickness in most of the pressurized region does not vary much ($\bar{x} \in [-1, 1]$). As such, the central film thickness (noted $\overline{h_c}$) is often used as a simple representation of the thickness in most of the contact;
- The fluid on the outlet of the contact (right side) sees a sudden peak of pressure followed by a rapid depression. This feature, commonly referred to as the "pressure spike", is associated with the location of the minimum film thickness (noted $\overline{h_m}$). It marks the location of the outlet of lubricant in rolling/sliding EHL contacts. It is the variable that needs to be compared with the surface roughness in order to determine if there is a risk of direct contact between the surfaces.

The prediction of the film thickness in EHL contact often takes the form of semi-analytical formulae in pure rolling conditions ([4]–[12]). They are written using the reduced parameters in eq. 1.3-1 to eq. 1.3-5. The semi-analytical models developed by Ertel-Grubin[4], [5] and Moes-Venner[12] are reported eq. 1.3-6 and eq. 1.3-7 respectively. They all predict film thicknesses proportional to the entrainment velocity u_e to some power.

$$W_1 = \frac{w^{1D}}{E' R^{1D}} \quad \textit{eq. 1.3-1}$$

$$U = \frac{\eta 2 u_e}{E' R^{1D}} \quad \textit{eq. 1.3-2}$$

$$G = \alpha E' \quad \textit{eq. 1.3-3}$$

$$M_1 = \frac{W_1}{U^{1/2}} \quad \textit{eq. 1.3-4}$$

$$L = G U^{1/4} \quad \textit{eq. 1.3-5}$$

$$\frac{h^*}{R^{1D}} = 1.31 (GU)^{3/4} (W_1)^{-1/8} \quad \textit{eq. 1.3-6}$$

$$\frac{h_m}{R^{1D} (U)^{1/2}} = 1.56 (L)^{0.55} (M_1)^{-0.125} \quad \textit{eq. 1.3-7}$$

where α is the pressure-viscosity coefficient of the lubricant. The viscosity dependence on pressure is represented by a simple Barus[46] or Roelands[61] law.

Nevertheless, EHL studies extend to a wide variety of kinematic conditions other than pure rolling conditions, where the two surface velocities may not be the same. It is therefore important to differentiate the entrainment velocity u_e from the sliding velocity u_s (see eq. 1.3-8). The Slide to Roll Ratio (SRR) is defined as the ratio of the sliding velocity over the

entrainment velocity, as in eq. 1.3-9. For given entrainment velocities, EHL contacts can be studied for a variety of SRRs([20], [51], [62]).

$$u_s = u_2 - u_1 \qquad \textit{eq. 1.3-8}$$

$$SRR = \frac{u_s}{u_e} \qquad \textit{eq. 1.3-9}$$

Because of the shearing occurring in sliding contacts, non-Newtonian and thermal effects have to be considered. In order for computational models to represent the behaviour of these sliding EHL contacts, it is important to transcribe the physical behaviour of the lubricant into usable equations. That domain of study is called rheology. In 1891, Veitch Wilson[63] observed a reduction of the film thickness but also of the friction when increasing the bulk temperature of the lubricant in his contact. This leads to numerous questions on how the temperature of the lubricant in EHL contacts affects its viscosity. The viscosity of some lubricants can also depend on the shear rate they are subject to (shear thinning behaviour[64]).

In the next section, different effects are introduced to give other perspectives on film thickness generation.

1.4 Other mechanisms for a load bearing capacity

In wind turbines or spacecraft momentum wheels, there is a need for higher radial load bearing capacity of rolling element bearings (REB) within the same space. One solution is to remove the cage in order to fill in more rolling elements up to full complement. The corresponding bearings are aptly named “Full complement bearings”. In spacecraft design where longevity is key and maintenance not an option, the lack of a cage also brings many other benefits such as the removal of cage squeal, the increase in stability, the improved lubrication conditions as well as the reduction of wear and fractures([13]–[16], [50]).

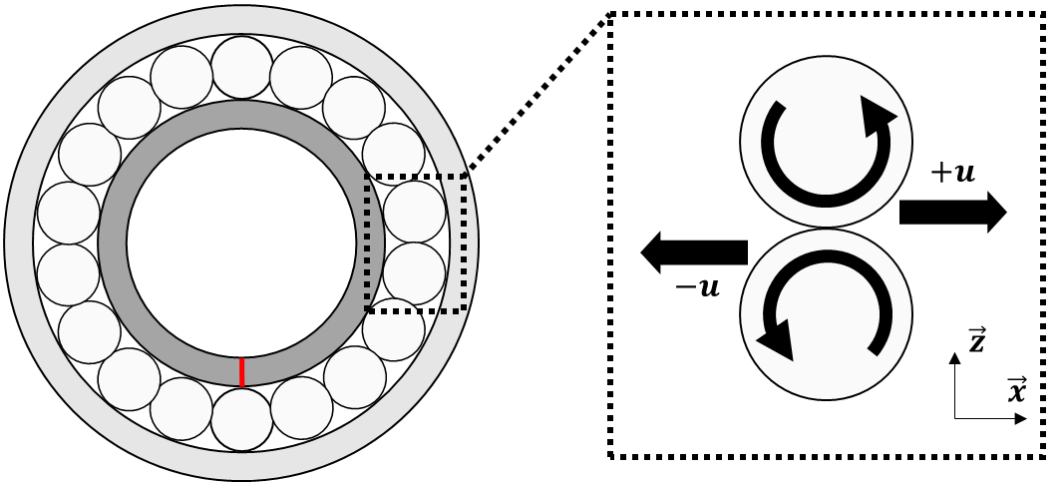

Figure 1.4-1 – On the left: Side view representation of a full complement bearing. On the right: Contact between two rolling elements.

In these bearings, two successive rolling elements come into contact. Assuming that the contact between rolling elements and the rings are without slip, the rotational speeds of each

rolling element are the same. Therefore, at their area of contact, the two rolling elements have the same tangential velocities, but in opposite directions (Figure 1.4-2 on the right). This means that there is a Zero Entrainment Velocity (ZEV) of the fluid ($u_e = 0$, or in other words $SRR \to \infty$). ZEV contacts can be found in the cam follower/tappet contact which is temporarily in such condition[65]. There is no oil wedge in ZEV contacts and thus the semi analytical formulae previously described lead to a nil value of the film thickness (see eq. 1.3-6 and eq. 1.3-7). Yet, this type of contact has been shown to be able to carry a load with a full lubrication([51], [62], [66]–[75]), since no wear is observed on the contacting surfaces.

Three phenomena other than the classical oil wedge previously described can explain a load bearing capacity. They are introduced in the next subsections.

1.4.1 Thermal effect: viscosity wedge

Cameron[17] introduced the concept of "viscosity wedge" to link the temperature variations in EHL contacts[63] with a change in load bearing capacity. He took the example of two solids entering the contact at the same temperature but exiting at a higher one, similarly to the one represented in Figure 1.4-3.

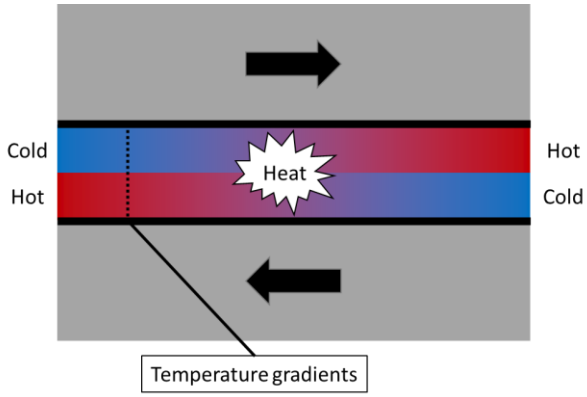

Figure 1.4-3 – Basic representation of the temperature variation of the fluid in opposite sliding.

This leads to temperature gradients in the thickness of the lubricant, and in turn, to viscosity gradients. Cameron then explained that the arising viscosity differences lead to the generation of pressure. Nowadays, using more sophisticated computational techniques and with the increase of the computational power at disposal, it is possible to precisely calculate the temperature and viscosity variations in high shearing contacts, as was demonstrated by Cheng[76]. Such contacts are referred to as Thermal Elastohydrodynamic contacts (TEHL). For very high sliding ratios, Chiu and Sibley[77] noted that the film thickness profiles presented two local minimum values at the inlet/outlet of the contact. The local maximum at the center of the contact is referred to as a "dimple". At infinite SRR (ZEV condition), the dimple is even more prominent([57], [67], [74]). When the solids in contact are made of the same material, and when the contact is subjected to ZEV condition, the typical profiles of pressure and film thickness are similar to the one represented in Figure 1.4-4 (taken from [68]).

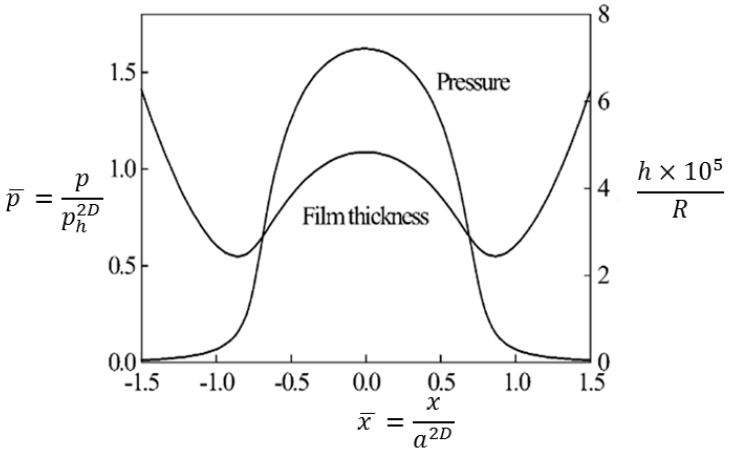

Figure 1.4-4 – Dimensionless pressure and film thickness profiles in an EHL contact under ZEV condition, taken from [68]*. The dimensionless film thickness is described using the equivalent curvature radius of the contacting surfaces.*

In this Figure, the typical dimple is visible, with two local minimum film thicknesses on the inlet/outlet as well as a local maximum film thickness at the center. The pressure profile is also quite different from the one in classical rolling EHL (in Figure 1.3-4), with a central pressure exceeding the Hertz pressure.

Cameron[78] argued that to increase the temperature gradients in the contact, it was necessary to have two different constitutive materials for both solids. This was proven to be inaccurate by Dyson and Wilson[75] who experimented on ZEV contacts with two steel surfaces, showing satisfactory film thicknesses. In their conclusion, they noted that ZEV contacts were better supported for smaller surface roughness. In the late 90s, a venture made by NASA ([13]–[16]) provided concrete evidence of the load bearing capacity of ZEV contacts due to the viscosity wedge. In the past two decades, further progress on the numerical techniques has led to the capacity to model ZEV contacts with even more precision. Guo et al.[68] noted the increase of the central film thickness with the load in ZEV contacts. This behaviour is specific to ZEV and has been shown to occur in point contact experiments and models ([67], [74]), and numerical line contact models ([51], [62], [72]). They also highlighted the small variations - and sometimes increases - of the minimum film thickness with the load. In 2015, Zhang et al.[72] studied ZEV contacts with non-Newtonian rheology. Depending on whether non-Newtonian effects were present or not, differences were noted on the values of central film thickness, maximum temperature and friction coefficient. However, the minimum film thickness was barely affected by those considerations. More recently, the same team studied the behaviour of ZEV contacts at very low film thicknesses[74] and for wavy surfaces[73].

1.4.2 Transient effect: squeeze

In full complement bearings, rolling elements accumulate under the radially loaded zone, which inevitably leads to a rarity of rolling elements in the unloaded zone. During the rotation of the bearing, rolling elements go in and out of the loaded zone. With no cage to ensure a fixed separation of the rolling elements, this leads to back and forth movements between them. Multiple other mechanisms can undergo fast normal approach between contacting

bodies. The term “squeeze” is used to refer to the normal approach between surfaces, displacing the lubricant separating them[18]. The study of contacts in squeeze motion can be separated in two. If the contacting surfaces have no tangential velocity, then the contact is in pure squeeze conditions. If there is an entrainment velocity of the solids, then the squeeze effect must be studied along with the oil wedge (hydrodynamic entrapment).

Pure squeeze

There have been various attempts at modelling the problem of squeeze. In 1875, Stefan[79] solved the problem of fully submerged approaching surfaces. He is the first to have developed an equation to predict the time of sinkage in the transient contact between a flat round plate and a smooth plane. Taylor[80] used Reynolds equation in the context of fully submerged squeeze contact with a viscous fluid. The case of impact loading, that is when a sudden load provokes a single normal approach, was studied by Eirich and Tabor[81]. Their model was used to calculate the pressure, fluid flow, shear rate and temperature distributions in the contact. A similar approach will be done in this thesis. In 1961, Christensen[82] is the first one to try to solve the EHL problem of the normal approach between cylindrical bodies. He demonstrated that for high loads, both the pressure dependence of the viscosity of the fluid and the elastic displacement of the solids needed to be taken into account. His experimental results, conducted for point contacts, were able to confirm these observations qualitatively. This work also showed how central pressures greater than the Hertz pressure could arise in the initial stages of the loading process. In 1970, Herrebrugh[83] and Conway[84] put the hydrodynamic equations and the elastic displacement equations into a single integral form. This change enabled the correct calculation of the approach velocity of the solids. Safa and Gohar[85] and Yang and Wen([86], [87]) measured the pressure between two non-conforming surfaces during an impact, highlighting the importance of taking the piezoviscosity of the fluid as well as the elasticity of the solids into account to understand the squeeze problem.

From the previous remarks, it appears that an accurate representation of the squeeze problem can be based on Reynolds equation. The variation of the viscosity of the fluid with pressure, as well as the elastic displacement of the contacting surfaces, need to be taken into account.

In 1967, Dowson and Jones[88] were the first ones to use interferometry techniques[54] to measure film thickness distributions between a steel ball and a glass disc under transient loading. Surprisingly, after the loading process was finished and the contact was then subjected to the highest load for one minute, there was still an important amount of highly pressurised lubricant separating the surfaces at the center even though dry contact started occurring at the edges of the contact area. The authors reported the presence of pools of lubricant hours after the maximum load was attained. When the contact was finally unloaded, the pools were dispersed and the surfaces took their original shapes. This is illustrated by the work of Nishikawa et al.[89], who experimented on point contacts in cyclic motion and were able to measure film thicknesses through interferometry techniques. The various interferograms they obtained for a single impact, along with the corresponding film thickness

profiles along a single line, are represented in Figure 1.4-5. The film thickness profiles show how the central film thickness barely varies during loading, and how the dimple is formed as the fluid is trapped.

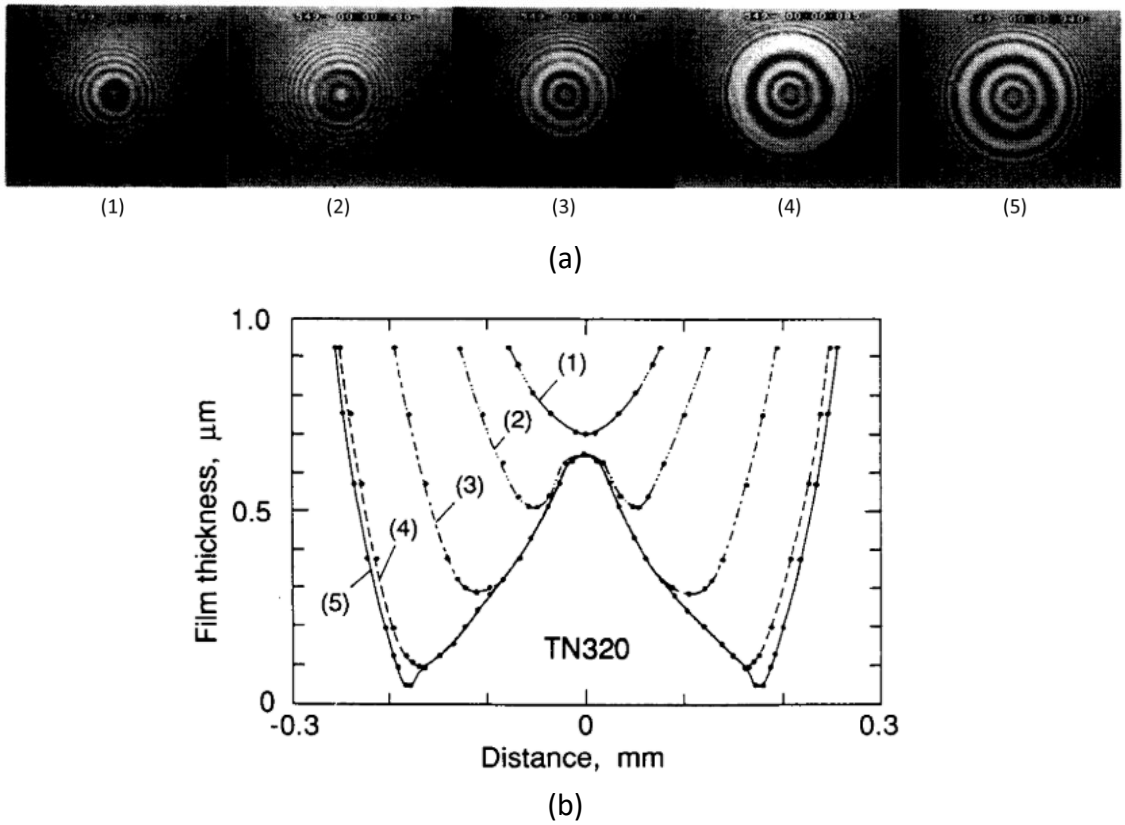

Figure 1.4-5 – (a) Interferograms during a single impact at 5 different moments. (b) Film thickness profiles along a single line for the same moments of the same impact. Taken from [89].

In 1967, Westlake and Cameron[90] studied the leakage of fluid overtime, showing how the central entrapment reduces in size, but not in central height. The stability of the central film thickness in pure squeeze is a topic of interest in various researches ([31], [91]–[93]). Film thickness predictions formulae have been proposed for the simple impact configuration (see Wang et al.([32], [94])). These semi-analytical models are able to predict the value of the central film thickness when the plateau is reached, taking the mass of the solids into account when solving the problem (see section 4.3.1).

Squeeze in rolling/sliding contacts

In 1963, Hays[95] used the limited computational power at his disposal to approximate the pressure profiles in squeeze problems and then to study the effect of a variation in curvature on the behaviour of the contact found in journal bearings. In 1964, this work was experimentally validated by Moore[96]. In 1971, Vichard[97] confronted the EHL film thickness analytical models to contacts where various input parameters were time dependant. In doing so, he showed how the squeeze effect contributes to the stability of the film thickness when present in HL and EHL contacts. In other words, transient effects tend to dampen the variation of the film thickness compared to stationary cases.

Most studies show that the squeeze effect acts against the changes in film thickness. This behaviour will be a focal point in later sections of this thesis.

Squeeze and viscosity wedge effects

Most existing works including both the squeeze and thermal effects are related to gears[98] or cam-tappet([20], [65], [99]) contacts. They show that taking the variations of temperature in dynamically loaded systems changes the predictions of film thicknesses[100], [101]. Moreover, in the case of cam-tappet contacts where the entrainment velocity can temporarily become nil, the viscosity wedge can have an important impact on the measurable values. To the author's knowledge, no work has been done on the normal approach of solids under constant thermal ZEV condition.

1.4.3 Wall slip

Wall slip (also known as boundary slip) happens when the lubricant does not adhere to a neighbouring surface[19]. This means that the velocity of the fluid near the surface is not equal to the velocity of the solid. In EHL contacts, where the contacting surfaces are made out of different materials, the lubricant may not adhere to both surfaces in the same way[102]. Wong et al.[103], [104] studied the behaviour of ZEV contacts between dissimilar materials. In their studies, fluid is first entrapped by a squeeze motion between the solids, which leads to a dimple. They then applied a tangential motion to observe the behaviour of the dimple. These tangential motions were extremely small in order to reduce the strength of thermal effects and isolate the effect of wall slip. They showed that under ZEV condition, the dimple was slowly moving out of the contact center, highlighting the effect of wall slip.

In stationary conditions and for two dissimilar solids under ZEV condition, they showed that promoting the wall slip on one of the contacting bodies by applying a surface coating lead to the appearance of a hydrodynamic lift, even at small velocities[105], [106]. They proposed a design for full complement bearings that run at low velocities, for which the rolling elements are successively made out of an oleophobic surface (prone to wall slip) and an oleophilic one (not prone to slip).

Because the present work focusses on steel/steel contacts (usually found in full complement bearings) that present non-atomistic roughness, the influence of wall slip will not be considered in the rest of the manuscript.

1.5 Objectives and methodology

In the roller-to-roller contact present in full complement bearings, the entrainment velocity is nil during the entire process (ZEV). Because of that, no oil wedge is present, and the load is supposedly only supported by the squeeze and viscosity wedge effects. The bibliographical work shows that the load bearing capacity of both the viscosity wedge and squeeze effects is conceptually well understood. However, no quantitative semi-analytical model currently exists to predict the film thickness due to thermal effects under ZEV condition. Many EHL

contacts found in applications are subjected to both the squeeze and transient effects, such as gears or cam-tappets, but the relative influence of each effect is unclear.

The objective of this thesis is to understand how both effects can explain the film thickness generation during an impact under ZEV condition. The literature on the squeeze effect is already very complete when compared to the literature on the viscosity wedge under ZEV condition. Therefore, this thesis will first focus on a quantitative approach to the viscosity wedge bearing capacity alone, before squeeze and thermal effects are considered together. The next chapter introduces the numerical and experimental setup used to meet the objective.

Chapter 2. Numerical and experimental approach

2.1 Numerical simulations 58

2.1.1 Modelling 58

2.1.2 Computational techniques 67

2.2 Experimental apparatus 69

2.2.1 Description of the test-rig 69

2.2.2 Film thickness measurements 72

2.2.3 Observed values of film thickness 73

2.3 Model validation and hypothesis discussion 74

2.3.1 Model validation in transient isothermal conditions 74

2.3.2 Experimental validation of the 2D model in stationary ZEV condition 76

2.3.3 Discussion on the 1D hypothesis 77

2.3.4 Discussion on the material properties of the solids 78

2.4 Conclusion 80

In this chapter, a numerical model of EHL contact under ZEV condition is presented in two configurations: the line contact (1D) variant and the wide point contact (2D) variant. Because thermal and transient effects are simulated, two validation steps are considered. On the one hand, a transient isothermal problem is simulated and compared with the literature. On the other hand, a tailored experimental procedure is developed to validate the model in stationary thermal conditions. The experimental setup is detailed in the second section of this chapter. The main model assumptions are discussed at the end of the chapter.

2.1 Numerical simulations

2.1.1 Modelling

This model is a continuation of the works by Raisin et al.[20] and Wheeler et al.[21], which are themselves based on the work by Habchi[107].

Referential and coordinate system

The contact is described in a Galilean reference frame and with a Cartesian coordinate system. Figure 2.1-1 is a representation of the contacting surfaces without any elastic displacement and with arbitrary radii of curvatures. The solids exclusively move along the x-axis. The film thickness is formed along the $\vec{z}$ direction. The y-axis completes the orthonormal coordinate system. The plane $z = 0$ is tangent to the undeformed surface of the bottom solid. One of the hypothesis discussed in this manuscript consists in considering cylinder-on-cylinder contacts. This particular case where the two solids are infinitely long in the y-dimension is called “1D”, which is to differentiate from the general “2D” case. Time is noted by the parameter t.

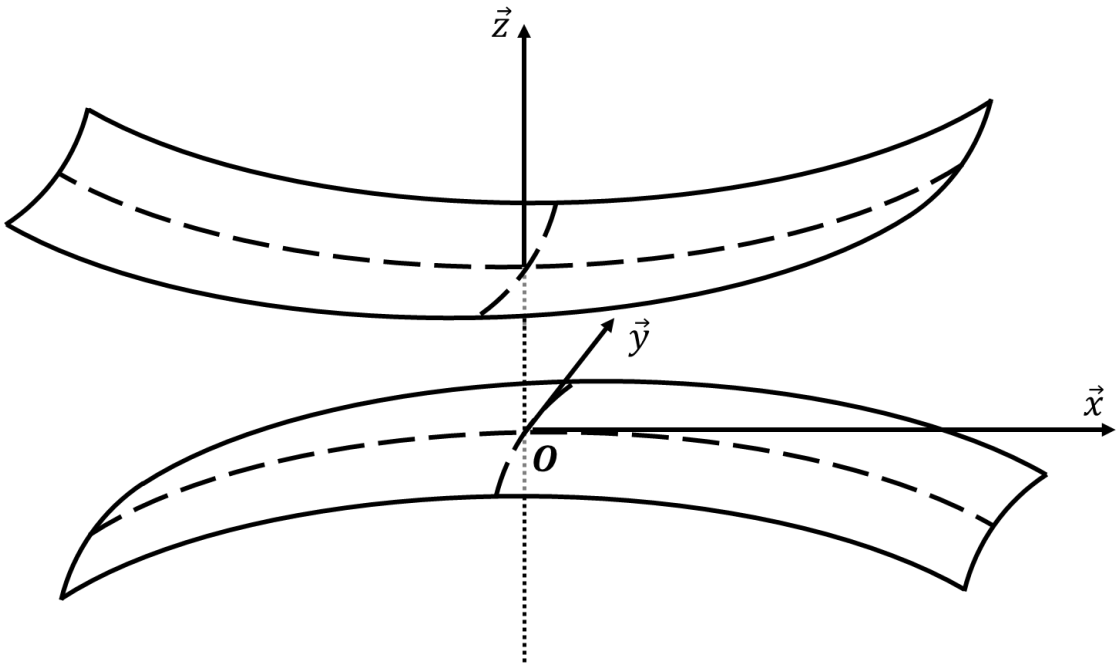

Figure 2.1-1 – Undeformed contact in a Cartesian coordinate system.

Reduced geometry

The description of the 1D variant assumes that two cylinders of curvature radii R_1^{1D} and R_2^{1D} enter into contact. For the 2D variant, the radii are given along the x and y-axes, as noted by the parameters $R_{1,x}^{2D}$, $R_{2,y}^{2D}$, $R_{1,x}^{2D}$ and $R_{2,y}^{2D}$. Reduced radii are introduced in eq. 2.1-1:

(1D)
$$\frac{1}{R_{eq}^{1D}} = \frac{1}{R_1^{1D}} + \frac{1}{R_2^{1D}}$$

(2D)
$$\frac{1}{R_{eq,x}^{2D}} = \frac{1}{R_{1,x}^{2D}} + \frac{1}{R_{2,x}^{2D}}$$
$$\frac{1}{R_{eq,y}^{2D}} = \frac{1}{R_{1,y}^{2D}} + \frac{1}{R_{2,y}^{2D}}$$

eq. 2.1-1

The film thickness separating the two solids is written as in eq. 2.1-2, considering a parabolic shape of the undeformed bodies as an approximation of cylinders (1D) and barrels (2D):

(1D)
$$h(x,t) = h_0(t) + g(x) + \delta(x,t)$$

(2D)
$$h(x,y,t) = h_0(t) + g(x,y) + \delta(x,y,t)$$

eq. 2.1-2

where h_0 is the rigid body separation and δ is the equivalent elastic surface displacement of both solids under the pressure distribution. The rigid solid geometry g is defined in eq. 2.1-3:

(1D)
$$g(x) = \frac{x^2}{2R_{eq}^{1D}}$$

(2D)
$$g(x,y) = \frac{x^2}{2R_{eq,x}^{2D}} + \frac{y^2}{2R_{eq,y}^{2D}}$$

eq. 2.1-3

Elastohydrodynamic equations, boundary conditions and domains

In the present model, three equations constitute the basis for EHL calculations. First, the pressure is calculated by an equation derived form of the Navier-Stokes equations called the Generalised Reynolds equation. Second, an elastic body mechanics calculation gives the elastic displacement of the contacting bodies. Third, an equation accounts for the load balance of the system.

The film thickness is expected to be of a few hundred nanometres while the contact length on the other hand is expected to be of a few hundred micrometres. Therefore, the hypothesis of thin films is made. In addition, inertia forces and surface tension are considered negligible with respect to the viscous forces. Moreover, there will be no boundary slip at the solid/fluid interfaces. Finally, the flow is considered laminar. All of those assumptions lead to a reduced form of the Navier-Stokes equations, as in eq. 2.1-4:

$$\vec{\nabla}p = \frac{\partial}{\partial z}(\overrightarrow{\tau_z}) \qquad \textit{eq. 2.1-4}$$

where $\overrightarrow{\tau_z} = \tau_{zx}\vec{x} + \tau_{zy}\vec{y}$ and:

$$\forall i \in \{x, y\}, \tau_{zi} = \eta \frac{\partial u_{fi}}{\partial z} \qquad \textit{eq. 2.1-5}$$

where u_{fi} is the fluid velocity in the direction i. In the 1D variant, $u_{fy} = 0$ and $\tau_{zy} = 0$. The viscosity η varies along the vertical axis. Considering no slip at the two solid/fluid interfaces, the double integration of eq. 2.1-4 along z leads to:

$$\overrightarrow{u_f} = \vec{\nabla}p\left(I_Z - \frac{\eta_e}{\eta'_e} I_1\right) + [\eta_e(u_2 - u_1)I_1 + u_1]\vec{x} \qquad \textit{eq. 2.1-6}$$

where $I_1 = \int_0^z \frac{1}{\eta(z\prime)} dz'$ and $I_z = \int_0^z \frac{z\prime}{\eta(z\prime)} dz\,'$ and $\frac{1}{\eta_e} = \int_0^h \frac{1}{\eta(z)} dz$ and $\frac{1}{\eta'_e} = \int_0^h \frac{z}{\eta(z)} dz$. u_1 is the surface velocity of the bottom solid and u_2 is the surface velocity of the top solid (see Figure 2.1-2). Note that under ZEV condition, $u_2 = -u_1 = u$ by definition. The mass conservation in the fluid writes as:

$$\frac{\partial \rho}{\partial t} + \frac{\partial (m_{f,x})}{\partial x} + \frac{\partial (m_{f,y})}{\partial y} = 0 \qquad \textit{eq. 2.1-7}$$

where $\forall i \in \{x, y\}, m_{f,i} = \int_0^h \rho u_{f,i} dz$. ρ is the density of the fluid. Combining eq. 2.1-6 and eq. 2.1-7 and differentiating leads to the Generalised Reynolds equation([108]):

$$\vec{\nabla}.\left(\left(\frac{\rho}{\eta}\right)_e \vec{\nabla}p\right) - \vec{\nabla}.\overrightarrow{\rho^*} - \frac{\partial \rho_e}{\partial t} = 0 \qquad \textit{eq. 2.1-8}$$

where $\rho_e = \int_0^h \rho dz$, $\rho'_e = \int_0^h \left(\rho \int_0^z \frac{dz'}{\eta}\right) dz$, $\rho''_e = \int_0^h \left(\rho \int_0^z \frac{z' dz'}{\eta}\right) dz$

and $\left(\frac{\rho}{\eta}\right)_e = \frac{\eta_e}{\eta'_e}\rho'_e - \rho''_e$, $\overrightarrow{\rho^*} = \begin{pmatrix} \rho'_e \eta_e (u_2 - u_1) + \rho_e u_1 \\ 0 \end{pmatrix}$

The Reynolds domain is represented in Figure 2.1-2, named either $\Omega_{\mathrm{p}}^{1\mathrm{D}}$ for the 1D variant or $\Omega_{\mathrm{p}}^{2\mathrm{D}}$ for the 2D variant. The sizes of the domains are indicated on the same Figure. At their edges, the pressure is set to 0.

Negative values of the pressure may appear at the outlets. To counter this problem, the penalty method, first described by Wu[109], is introduced. In ZEV, this term does not have a significant impact on the results given the fact that pressure is generated on both sides of the contact. It is still a useful and simple tool in the early stages of the calculation process described in section 2.1.2.

Rheological behaviour

Highly loaded ZEV contacts exhibit high pressures, contact temperatures and shear rates [51]. In rolling EHL where these variables may vary in a similar manner [74], it is required to account for their influence on the lubricant density and viscosity. Therefore, there is a need to characterise those dependencies in order to predict the behaviour of the contacts. There is a multitude of descriptive laws that can be used to represent the various lubricants found in the market. They each have their range of uses and shortcomings that need to be taken into account when analysing the results of the model.

Lubricant density

Murnaghan et al.[22] proposed the equation of state in eq. 2.1-9:

$$\rho(p,T) = \rho_R \frac{1}{\left(1+\frac{K_M'}{K_M}p\right)^{-\frac{1}{K_M'}}} \times \frac{1}{1+a_v(T_0-T_R)} \qquad \textit{eq. 2.1-9}$$

where $K_M = K_{00}e^{-\beta_K T}$, with β_k the temperature-density parameter. K_{00}, K_M' and a_v are specific parameters dependant on the modelled fluid.

This model is based on various ratios of volumes rooted in physical behaviours. However, its complexity makes parametrisation more difficult.

Lubricant Newtonian viscosity

Barus'[46] law is often presented as the simplest description of the viscosity variation with the pressure. It was initially used due to the computational constraints of former studies, and is now considered obsolete when quantitative descriptions of highly loaded contacts are required. It follows an exponential variation, as in eq. 2.1-10:

$$\eta(p) = \eta_R \exp(\alpha p) \qquad \textit{eq. 2.1-10}$$

where η_R is the viscosity at the reference pressure and α is the pressure-viscosity index.

The improved WLF[23] correlation is an alternative way to model the viscosity of some fluids, written as in eq. 2.1-11:

$$\eta(p,T) = \eta_G \left(\frac{-2.303\ C_1 \left(T - T_g\right) F}{C_2 + \left(T - T_g\right) F} \right)$$

where

$$T_g(p) = T_{g0} + A_1 \ln\left(1 + A_2 p\right)$$

$$F(p) = (1 + B_1 p)^{B_2}$$

eq. 2.1-11

A_1, A_2, B_1, B_2 as well as C_1 and C_2 are the correlation parameters of the model. η_G is the viscosity at glass transition and T_{g0} the glass transition temperature at ambient pressure.

Lubricant non-Newtonian viscosity

The influence of the shear stress on the viscosity is commonly considered using the Carreau and Yasuda[24] model in eq. 2.1-12:

$$\eta(p,T,\tau_e) = \frac{\eta(p,T)}{\left(1 + \left(\frac{\tau_e}{G_{CY}}\right)^{a_{CY}}\right)^{\frac{\frac{1}{n_{CY}} - 1}{a_{CY}}}}$$

where

$$\tau_e = \sqrt{{\tau_{zx}}^2 + {\tau_{zy}}^2}$$

eq. 2.1-12

τ_{zx} and τ_{zy} are the calculated shear stresses along the x and y-axes. a_{CY}, G_{CY} and n_{CY} are specific parameters depending on the modelled fluid.

Elastic surface displacement

Subjected to high pressures, the solid surfaces undergo non-negligible elastic displacements. In the context of this study, isotropic materials are used and their surface displacements are considered elastic. Similarly to Habchi[107], the total elastic displacement of both surfaces is computed using an equivalent solid, whose elastic properties are defined as:

$$E_{eq} = \frac{E_2^2 E_1 (1 + \upsilon_1)^2 + E_1^2 E_2 (1 + \upsilon_2)^2}{\left(E_2(1 + \upsilon_1) + E_1(1 + \upsilon_2)\right)^2}$$

eq. 2.1-13

$$\upsilon_{eq} = \frac{E_2 \upsilon_1 (1 + \upsilon_1) + E_1 \upsilon_2 (1 + \upsilon_2)}{E_2(1 + \upsilon_1) + E_1(1 + \upsilon_2)}$$

eq. 2.1-14

where E_1, υ_1, E_2 and υ_2 are the elastic parameters of both contacting bodies.

The combined elastic displacement is calculated by a linear elastic displacement model, as in eq. 2.1-15:

$$\nabla . \boldsymbol{\sigma_{elastic}} = 0 \qquad \textit{eq. 2.1-15}$$

where $\boldsymbol{\sigma_{elastic}} = \boldsymbol{C\varepsilon_{elastic}}(\overrightarrow{\boldsymbol{U_\delta}})$ and $\overrightarrow{\boldsymbol{U_\delta}} = \{U_\delta,\ V_\delta,\ W_\delta\}$ the unknown displacement vector. C is the stiffness matrix (eq. 2.1-16) and $\boldsymbol{\varepsilon_{elastic}}$ the strain vector (eq. 2.1-17):

$$\boldsymbol{C} = \frac{E_{eq}}{(1+\upsilon_{eq})(1-2\upsilon_{eq})} \times \begin{bmatrix} 1-\upsilon_{eq} & \upsilon_{eq} & \upsilon_{eq} & 0 & 0 & 0 \\ \upsilon_{eq} & 1-\upsilon_{eq} & \upsilon_{eq} & 0 & 0 & 0 \\ \upsilon_{eq} & \upsilon_{eq} & 1-\upsilon_{eq} & 0 & 0 & 0 \\ 0 & 0 & 0 & \frac{1-2\upsilon_{eq}}{2} & 0 & 0 \\ 0 & 0 & 0 & 0 & \frac{1-2\upsilon_{eq}}{2} & 0 \\ 0 & 0 & 0 & 0 & 0 & \frac{1-2\upsilon_{eq}}{2} \end{bmatrix} \qquad \textit{eq. 2.1-16}$$

$$\boldsymbol{\varepsilon_{elastic}}(\overrightarrow{\boldsymbol{U_\delta}}) = \begin{Bmatrix} \frac{\partial U_\delta}{\partial x} \\ \frac{\partial V_\delta}{\partial y} \\ \frac{\partial W_\delta}{\partial z} \\ \frac{\partial W_\delta}{\partial y} + \frac{\partial V_\delta}{\partial z} \\ \frac{\partial W_\delta}{\partial x} + \frac{\partial U_\delta}{\partial z} \\ \frac{\partial V_\delta}{\partial x} + \frac{\partial U_\delta}{\partial y} \end{Bmatrix} \qquad \textit{eq. 2.1-17}$$

In the 1D variant of the model, $V_\delta = 0$ as well as all derivatives with respect to y, which corresponds to the plain strain hypothesis. The domain in which the elastic displacement of the equivalent solid is calculated is represented in Figure 2.1-2. The base face/edge ($\Omega^{1D}_{e,base}$ for the 1D variant and $\Omega^{2D}_{e,base}$ for the 2D variant) is considered fixed ($\overrightarrow{\boldsymbol{U_\delta}} = \vec{0}$) while the value of pressure calculated with the Reynolds equation is ascribed to Ω^{1D}_{p} for the 1D variant and Ω^{2D}_{p} for the 2D variant ($\boldsymbol{\sigma_{elastic}}.\vec{z} = -p\vec{z}$). The rest of the outside boundaries of the domain are free, with $\boldsymbol{\sigma_{elastic}}.\vec{z} = \vec{0}$. The total displacement of both surfaces δ (as it appears in eq. 2.1-2) is calculated as in eq. 2.1-18:

$$\delta = |W_\delta|_{\Omega_p} \qquad \textit{eq. 2.1-18}$$

Load balance equation

The load balance equation is also verified, as written in eq. 2.1-19. The rigid body separation h_0 is calculated so that integral of the pressure field over the pressurised domain corresponds to the applied load.

(1D) $$\int_{\Omega_p^{1D}} p\, dx = w^{1D}$$

(2D) $$\iint_{\Omega_p^{2D}} p\, dxdy = w^{2D}$$ *eq. 2.1-19*

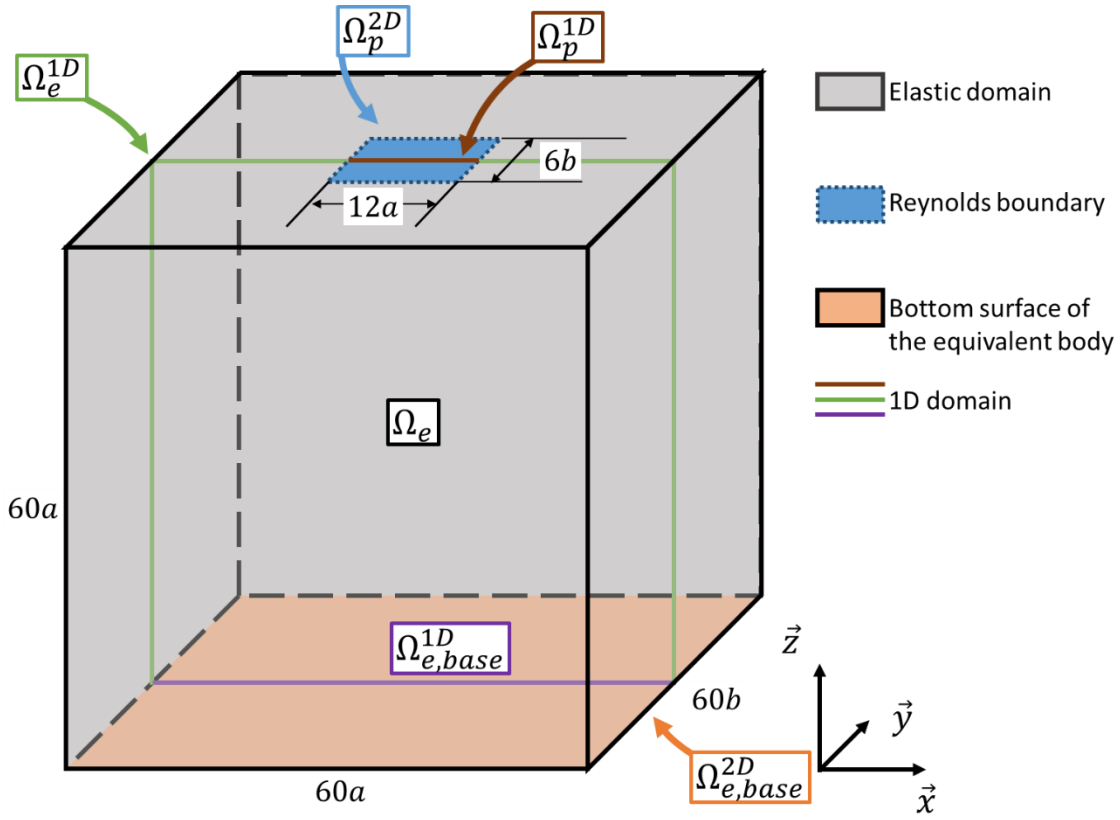

Figure 2.1-2 – Domain of calculation for the EHL aspect. The Generalised Reynolds calculation is calculated on the domain Ω_p^{1D} for the 1D variant and Ω_p^{2D} for the 2D variant. The equivalent elastic body domain is Ω_e^{1D} for the 1D variant and Ω_e^{2D} for the 2D variant. The linear load is defined along y. As such, the 1D slice is under a pressure profile along x. This is representative of an infinitely long problem along y.

In the time dependent studies presented in this document, the load is varied. The size of the computational domains is adjusted to take into account the widening contacts, similarly to Raisin[65]. Moreover, ZEV contacts have been shown to have slightly larger pressure profiles compared to classical rolling EHL. The size of the domains in Figure 2.1-2 and Figure 2.1-3 are chosen according to those constraints.

Thermal model equation, boundary conditions and domain

Because of the high shear heating generated in ZEV contacts and due to the fact that the fluid viscosity and density depend on the temperature, there is a need to model the temperature variations in the fluid. The energy equilibrium of the system is therefore calculated, assuming that only shear and compression heating happens in the fluid. Moreover, the transmission of energy through radiation is omitted as convection and conduction are considered prevalent. The temperature field is calculated in both solids as well as in the fluid thickness. As such, the following equations will be indexed to represent the domain in which they are solved. From bottom to top, the sub-domains indexes are:

$$i = \begin{cases} 1 & \text{for solid 1} \\ f & \text{for the fluid} \\ 2 & \text{for solid 2} \end{cases} \qquad \textit{eq. 2.1-20}$$

The domains in which the energy equation is calculated are represented in Figure 2.1-3. The labels of each sub-domain surface are not represented. The shear and compression heat sources can be calculated in the fluid subdomain as in eq. 2.1-21:

$$Q_s = \eta\left(\nabla\vec{u}_f\right)^2$$

$$Q_c = -\frac{T}{\rho}\frac{\partial\rho}{\partial T}\left(\vec{u}_f.\vec{\nabla}p\right) \qquad \textit{eq. 2.1-21}$$

Overall the heat generated is defined in eq. 2.1-22:

$$Q_i = \begin{cases} 0 & \text{for } i = \{1, 2\} \\ Q_s + Q_c & \text{for } i = f \end{cases} \qquad \textit{eq. 2.1-22}$$

The corresponding energy equilibrium writes as in eq. 2.1-23:

$$-\nabla(k_i\nabla T) + \rho_i C_{pi}(\vec{u}_i\nabla T + \frac{\partial T}{\partial t}) = Q_i \qquad \textit{eq. 2.1-23}$$

where k is the thermal conductivity and C_p the thermal capacity.

Note: The total heat source (per unit length in 1D) is written as in eq. 2.1-24, for $j = \{s, c, f\}$:

(1D) $$P_j^{1D} = \iint_{\Omega_{T,f}^{1D}} Q_j \, dxdz$$ *eq. 2.1-24*

(2D) $$P_j^{2D} = \iiint_{\Omega_{T,f}^{2D}} Q_j \, dxdydz$$

Temperature is continuous in the entire domain. The heat flux is considered constant between the fluid/solid interfaces. As such eq. 2.1-25 and eq. 2.1-26 are applied:

$$k_f \left.\frac{\partial T}{\partial z}\right|_{z=0^+} = k_1 \left.\frac{\partial T}{\partial z}\right|_{z=0^-}$$ *eq. 2.1-25*

$$k_2 \left.\frac{\partial T}{\partial z}\right|_{z=h^+} = k_f \left.\frac{\partial T}{\partial z}\right|_{z=h^-}$$ *eq. 2.1-26*

A fixed temperature constraint ($T = T_0$) is applied to the top and bottom external faces of both solids. The same constraint also applies to the side faces where $y = \pm 6b$, as well as the side faces of the solids and fluid domains where matter enters the computation domain (i.e. when the velocity vector is oriented towards the domain). When the velocity vector is locally oriented outside of the contact, flux is zero, as in eq. 2.1-27.

$$\left.\frac{\partial T}{\partial x}\right|_{\Omega} (x, y, z) = 0 \text{ if } \overrightarrow{u_f}.\vec{n} > 0$$ *eq. 2.1-27*

where $\vec{n}$ is the outer-pointing normal vector to the surface.

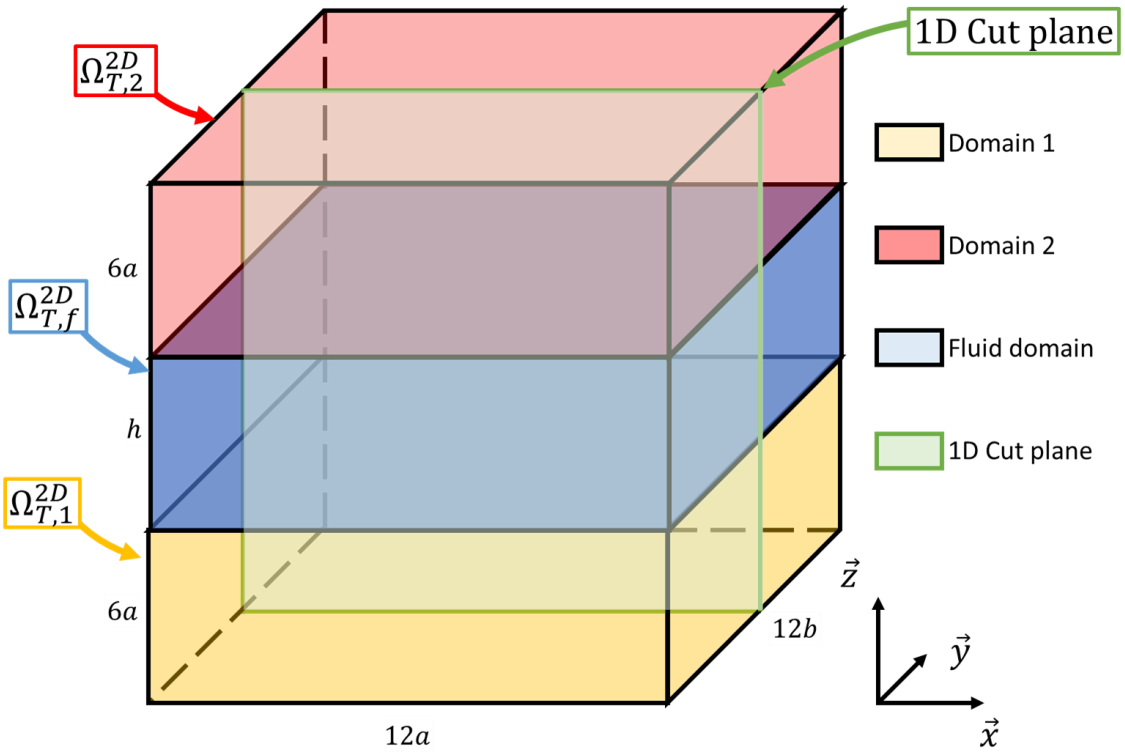

Figure 2.1-3 – Domain of calculation for the energy equation. The entire domain is referred to as Ω_T^{1D} in the 1D variant and Ω_T^{2D} in the 2D variant.

2.1.2 Computational techniques

Numerical process

The model described is non-linear and highly coupled. It is possible to implement a step-by-step solver process where different equations and dependencies of the full model are successively introduced, very similar to Raisin et al.[20]. As seen in Table 2.1-1, the initial step serves to initialise the elastic body displacement assuming a Hertz pressure profile. In step 2, the isothermal EHL problem is computed. In parallel, the temperature field is initialised but its influence on ρ and η is not yet taken into account. ZEV stationary isothermal conditions lead to no pressure generation. As such, the calculation process assumes a small entrainment velocity in step 2 ($SRR = 70\%$). With that same SRR, the thermal (step 3) and non-Newtonian effects (step 4) are progressively introduced. A parametric continuation on the velocities is done to achieve ZEV condition in step 5. This step can be used as a reference for parametric sweeps (stationary calculations for different loads, velocities, external temperatures or other input parameters) or transient calculations under ZEV condition.

Step	Name	Fully coupled equations	Loosely coupled equations
1	Hertz contact	• Elastic body displacement	
2	EHL $SRR = 70\%$	• Elastic body displacement Reynolds equation • Load balance equation	• Energy balance equation
3	TEHL Newtonian $SRR = 70\%$	• Elastic body displacement • Generalised Reynolds equation • Load balance equation • Energy balance equation	
4*	TEHL non-Newtonian $SRR = 70\%$	• Elastic body displacement • Generalised Reynolds equation • Load balance equation • Energy balance equation	
5	TEHL non-Newtonian* ZEV	• Elastic body displacement • Generalised Reynolds equation • Load balance equation • Energy balance equation	
6+	Parametric study or Transient study	• Elastic body displacement • Generalised Reynolds equation • Load balance equation • Energy balance equation	

* Step 4 may be foregone when the fluid is considered Newtonian. Step 5 then becomes "TEHL Newtonian ZEV"

Table 2.1-1 – Computational steps leading to a complete set of ZEV results.

Computation

All calculations are made on COMSOL 5.2. At each step of the calculation process, a Newton-Raphson full-system approach is written for all degrees of freedom in the finite element description. In Table 2.1-1 from step 3 onwards, the unknown values of the model are the pressure p, the elastic displacement of the equivalent solid $\overrightarrow{U_\delta} = \{U_\delta, V_\delta, W_\delta\}$, the rigid body separation h_0 and the temperature distribution T. The calculation time is also affected by the calculation of the integral values I_1 and I_z (see eq. 2.1-6). A typical TEHL ZEV stationary non-Newtonian calculation (up to step 5) with 16 100 degrees of freedom, on a computer equipped with a 3.5 GHz processor, takes 30 minutes. For parametric sweeps (step 6+, used to reach new values for a chosen parameter) it takes from 1 minute (case close to the reference calculation obtained in step 5) to a few hours (usually for extremely low film thicknesses with high local viscosities) to obtain a result with a non-Newtonian fluid. A transient calculation

(step 6+) with a Newtonian fluid, and with a thousand time steps takes up to one hour in favourable conditions. All of those calculation times can vary greatly depending on the density and viscosity model choices as well as the input parameters.

Stabilisation techniques

Given the high pressures and low film thicknesses found in EHL contacts, the Galerkin Least Squares stabilisation technique (see Hughes et al.[110]) is implemented in the 2D model. Because this is a residual based technique, the GLS method does not change the solution to the problem.

The Isotropic Diffusion ([111]) is another term that is added to the Generalised Reynolds equation to smooth out the obtained results. Contrary to the GLS technique, this term induces small changes of the computational results. A coefficient of 0.5 is chosen to mitigate the effects of ID and to ensure that the physical results are not influenced by it.

For more details on the implementation of those techniques, see the work by Habchi[107].

Regarding the thermal component of the model, no stabilisation techniques were employed.

Conclusion on the numerical model

The numerical model provides information on ZEV contacts in both stationary and transient conditions. This work aims to describe wide point contacts, and the 1D and 2D variants of the model reflect this objective. The next section will describe the experimental apparatus used to validate the model in stationary conditions.

2.2 Experimental apparatus

The experimental validation of the thermal model in ZEV condition is done with a tribometer developed in LaMCoS[25]. In previous studies, this test-rig was used for ball-on-plane contacts as well as barrel-on-plane ones.

2.2.1 Description of the test-rig

The test-rig, Jerotrib, was developed in 1999 by Molimard[25] to measure film thicknesses in EHL contacts. Since then, it has been used in a variety of applications. For example, Wheeler et al.[26] conducted skewing experiments on wide point contacts with a glass disc. Other works include the study of the Limiting Shear Stress by Ndiaye et al.[27]. This test-rig enables the measurement of the film thickness separating the opaque concave surface of a solid body and a transparent disc. It is represented in Figure 2.2-1.

In the present study, the opaque body is a steel barrel. At the point of contact with the disc, the two radii of curvature of the barrel are $R_{2,x}^{2D} = 0.013\ m$ and $R_{2,y}^{2D} = 0.330\ m$. The contact presents a low ellipticity ratio $D = R_{2,x}^{2D}/R_{2,y}^{2D} = 0.04$. Along with the steel barrel, a sapphire disc is chosen to enable optical measurements. Its thermal similarity with steel ([66], [70])

helps mimicking industrial applications which often involve steel on steel contacts. In order to understand the influence of the materials of the contacting bodies, a glass disc (with a chromium layer) is also selected for a comparative test presented in Appendix A. All surfaces are polished in order to reach an average surface roughness of $S_{a,i} < 5\ nm$ (see eq. 1.1-2, measured over a $1\ cm^2$ area). The properties of the solids are specified in Table 2.2-1.

Note: The value of thermal conductivity k of steel is taken from the given sources([26], [27]). Reddyhoff *et al.*[112] advanced a different value of $k = 21\ W.m^{-1}.K^{-1}$. This difference and the effect it has on the observed values are discussed in section 2.3.4.

	Steel	Sapphire
$E\ [Pa]$	210×10^9	360×10^9
υ	0.3	0.34
$\rho\ [kg.m^{-3}]$	7850	4000
$C_p\ [J.kg^{-1}.K^{-1}]$	470	750
$k\ [W.m^{-1}.K^{-1}]$	46	40

Table 2.2-1 – Material properties ([26], [27]*).*

Unlike past studies on the Jerotrib test-rig, a new lubrication system is used in order to lubricate both surfaces as they enter into the contact from opposite sides. Two projection nozzles are mounted on a tube directly connected to an external bath, as can be seen in Figure 2.2-2. The temperature of the fluid is fixed in that bath, with a precision of $0.2\ K$ (the temperature in the contact region is not measured). To close the loop of the feeding system, the lubricant outside of the contact is recovered through gravity, as shown in Figure 2.2-2. The lubricant is brought to the contact thanks to a peristaltic pump. In the experiments presented here, the volumetric flow of lubricant is fixed at $34\ cL.min^{-1}$. For the entirety of these results, the values of film thickness do not vary with a bigger flow.

The barrel and the disc are rotated by two independent servomotors, horizontally for the former and vertically for the latter (see Figure 2.2-1). The contact is loaded by moving the barrel and the horizontal servomotor up against the sapphire disc. A load sensor indicates the normal contact load with a precision of up to $2.5\ N$. For each set of operating conditions, the sensor is offset to 0 when the initial contact is made between the disc and the barrel. The lubricant is a commercial turbine (Shell T9) oil used in previous studies (see [26][28]) whose properties are detailed in Table 2.2-2. It follows a Murnaghan[22] density law (see eq. 2.1-9), its Newtonian viscosity is described by the improved WLF[23] correlation (see eq. 2.1-11) and its non-Newtonian viscosity follows the model proposed by Carreau and Yasuda[24] (see eq. 2.1-12).

$C_{pf}\ [J.kg^{-1}.K^{-1}]$	1900	C_2	14.1596
$k_f\ [W.m^{-1}.K^{-1}]$	0.118	A_1	188.95
$\rho_R\ [kg.m^{-3}]$	872	$A_2\ [Pa^{-1}]$	0.533×10^{-9}
$T_R\ [K]$	298	$B_1\ [Pa^{-1}]$	7.37×10^{-9}
$K_{00}\ [Pa]$	9.234×10^{9}	B_2	-0.6171
$K_M{}'$	10.545	$T_{g0}\ [K]$	204.68
$a_v\ [K^{-1}]$	7.734×10^{-4}	$p_0\ [Pa]$	0
$\beta_k\ [K^{-1}]$	6.09×10^{-3}	a_{CY}	5
$\eta_g\ [Pa.s]$	1×10^{12}	n_{CY}	0.35
C_1	15.9035	$G_{CY}\ [Pa]$	7×10^{6}

Table 2.2-2 – Fluid properties ([26][28]*).*

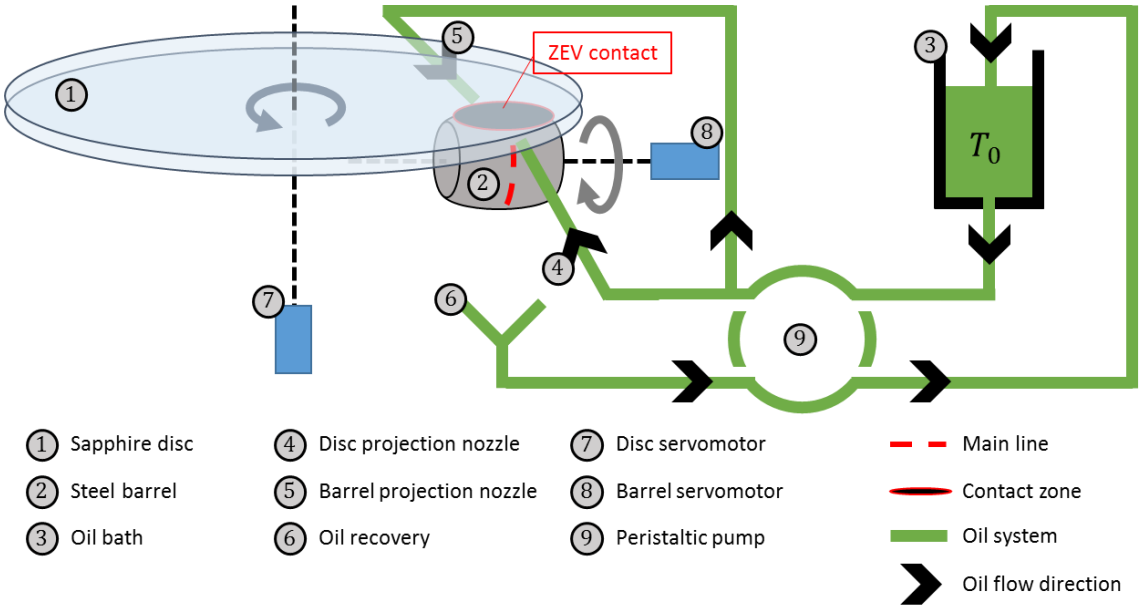

Figure 2.2-1 – Representation of the experimental apparatus.

Figure 2.2-2 – Photo of the projection system (4) (5) and the mounted barrel (2). The disc is not mounted.

2.2.2 Film thickness measurements

The white light Differential Colourimetric Interferometry (DCI) technique was developed on the Jerotrib test-rig by Molimard et al.[25] and adapted to wide contacts by Wheeler et al.[26] to measure the film thickness separating the barrel from the disc. White light is emitted from a source and is sent through the transparent disc. In Figure 2.2-3, light rays $I0$ are emitted from the top and are partially reflected at the disc/fluid interface with an intensity $I1$. The rest of the signal, $I2$, passes through the lubricant before being reflected on the barrel surface. These reflected rays are then again partially reflected at the fluid/disc interface. The amount of light that passes through that interface is referred to as $I3$. The rest is considered negligible, meaning that only the first reflection of light on the steel barrel is considered. The signals $I1$ and $I3$ exhibit a phase difference because of their different optical paths. Since white light is constituted of rays of various wavelengths, constructive or destructive interferences are observed for any phase difference. Capture of the light emitted gives a coloured map of the contact called an interferogram.

The calibration process is done in static conditions. When a quantity of lubricant is present between the solids in a dry contact, the film thickness measurement gives the separation of the surfaces. This principle, described by Molimard[29], is restricted to film thicknesses lower than $800\ nm$. More information on DCI and how it is performed when measuring film thicknesses with Jerotrib can be found in the work by Wheeler et al.[26].

Note: The path of light rays trough any material depends on its refraction index. This parameter varies with the pressure and temperature in the contact. The analysis of the experimental data is conducted assuming that the pressure in the contact is a Hertz distribution, and that the temperature everywhere is equal to the external temperature. This assumption is required to ensure that the experimental results are independent of the numerical model. Given the importance of the thermal state in ZEV contacts, this assumption is flawed to a degree. This is be discussed in Appendix B.

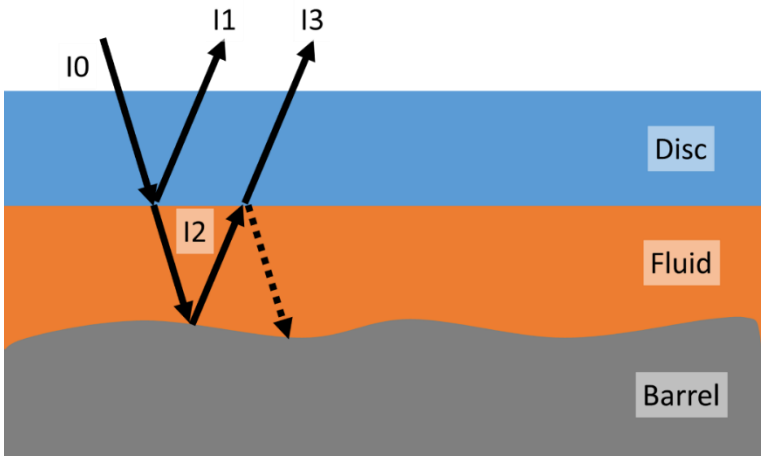

Figure 2.2-3 – Visualisation of the transmission and reflection of a light ray.

A total of 50 conditions are applied for the sapphire/steel contact, detailed in Table 2.2-3. As was stated, a complementary glass/steel experiment is also conducted for a velocity $u = 5\ m/s$, a load $\mathrm{w}^{2\mathrm{D}} = 50\ N$ and an external temperature $T_0 = 293.15\ K$ (in this case, the equivalent load per unit length is $w^{1D} = 4.6 \times 10^4\ N.m^{-1}$). For each set of conditions, 6 interferograms are captured to measure film thicknesses. The information contained in an interferogram is detailed in the next subsection.

$T_0\ (K)$	$u(m/s)$	$\mathrm{w}^{2\mathrm{D}}(N)$	$p_h(GPa)$	Equivalent $\mathrm{w}^{1\mathrm{D}}(N.m^{-1})$	Number of Cases
293.15	$\left\{\begin{matrix}1.77; 1.99; 2.26; 2.51; 2.81;\\ 3.16; 3.54; 3.97; 4.46; 5.00;\\ 5.61; 6.30; 7.06; 7.92\end{matrix}\right\}$	30	0.390	4.14×10^4	14
293.15		50	0.462	5.82×10^4	14
293.15		100	0.582	9.24×10^4	14
308.15	$\{3.16; 3.97; 5.00; 6.30; 7.92\}$	50	0.462	5.82×10^4	5
323.15	$\{5.00; 6.30; 7.92\}$	50	0.462	5.82×10^4	3

Table 2.2-3 – Sets of measurements for the sapphire disc.

2.2.3 Observed values of film thickness

Interferograms provide the values of film thicknesses in the entire contact area. At some specific locations, the value of the film thickness has to be discussed. The interferogram shown in Figure 2.2-4 gives the film thickness separating a sapphire disc and a steel barrel for $u = 5\ m/s$, $\mathrm{w}^{2\mathrm{D}} = 50\ N$ and $T_0 = 293.15\ K$. The direction of sliding is marked on the left side, and the coordinate system respects the one introduced in the model. The dotted main central line is of particular interest as it is the location where the information should be extracted for comparison with the 1D model. In total, four regions of interest can be highlighted in that interferogram. They are marked by different letters:

- Mark “A”: Two lobes are observed on the left and right sides of the contact. Those side lobes are the location of the global minimum film thickness. They dictate when the experiments have to be stopped in order to protect the surface of the disc. These values have already been described by Guo[70]. However, the rest of this manuscript will focus on the central line;
- Mark “B”: A local maximum is found right at the center of the contact. It marks the presence of a central dimple. In the rest of the document, the value of film thickness at this location is referred to as the central film thickness h_c;
- Marks “C” and “D”: Two local minimum film thicknesses can also be found along the vertical dashed line, located close to the inlet/outlet areas of the contact. They are noted by the letters “C” and “D” in Figure 2.2-4. Their values differ slightly from one another ([66], [67], [70], [72], [113]) because of the dissimilarity in the properties of the solid materials in contact. The highest local minimum film thickness is called h_m^+ and the lowest one is called h_m^-. The average value of the two will be referred to as the minimum film thickness and will be noted h_m.

This analysis is only applicable to steel/sapphire contacts or any two similar materials. For steel/glass contacts, refer to Appendix A.

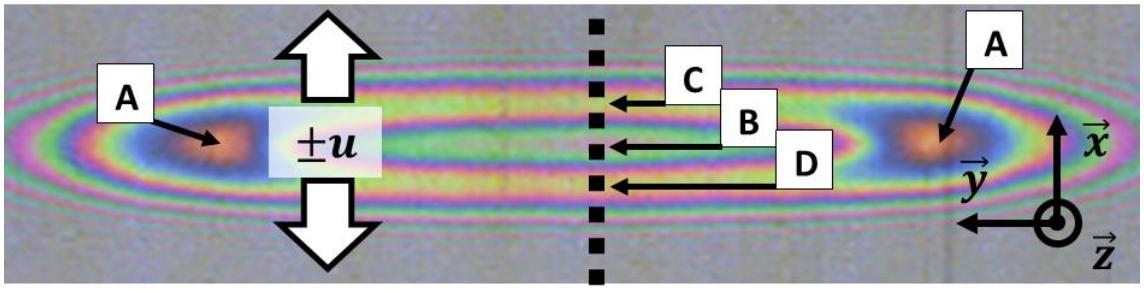

Figure 2.2-4 – Interferogram obtained with a sapphire disc (Magnification $\times 10$, $u = 5\ m/s$, $w^{2D} = 50\ N$ *and* $T_0 = 293.15\ K$).

2.3 Model validation and hypothesis discussion

The model presented in this chapter needs to be validated. This is done in two steps: first, the transient isothermal model is discussed with some entrainment; then, stationary thermal ZEV conditions are analysed. After that, a number of modelling hypotheses are discussed.

2.3.1 Model validation in transient isothermal conditions

Liu et al.[114] conducted transient isothermal calculations with the parameters given in Table 2.3-1. The fluid is considered Newtonian. It follows the Dowson-Higginson[115] density law and Roelands[61] viscosity law. The size of the calculation domain for Reynolds equation is defined as $x \in [-4.5a^{1D}, 1.5a^{1D}]$. No penalisation or stabilisation techniques are employed.

$w_0^{1D}\ [N.m^{-1}]$	8695
$C_w\ [-]$	0.1
$f\ [Hz]$	3000
$R_{eq}^{1D}\ [m]$	0.004
$u_1, u_2\ [m.s^{-1}]$	0.1
$\mu_R\ [Pa.s]$	0.00411
$\rho_0\ [kg.m^{-3}]$	850
$\alpha_{Roe}\ [Pa^{-1}]$	21×10^{-9}
$E_1, E_2\ [Pa]$	2.07×10^{9}
$\upsilon_1, \upsilon_2\ [-]$	0.3

Table 2.3-1 – Parameters used in the calculation made by Liu et al.[114].

First, the contact is studied in transient conditions with a variation of the load as described in eq. 2.3-1. Ten periods are calculated in order to reach a periodic state. As such, the results presented are obtained during the last period. In Figure 2.3-1, the dimensionless pressure ($\bar{p} = p/p_h^{1D}$) and film thickness ($\bar{h} = h \times R_{eq}^{1D}/{a^{1D}}^2$) profiles are represented along $\bar{x} = x/a^{1D}$ at four different moments ($2\pi ft = \{\pi/2\,, \pi, 3\pi/2\,, 2\pi\} + 18\pi$). The corresponding values of central pressure, central film thickness and minimum film thickness are reported in Table 2.3-2.

$$w^{1D}(t) = w_0^{1D} \times \left(1 + C_w \sin(2\pi f t)\right) \qquad \text{eq. 2.3-1}$$

For all measured values, the maximum relative difference happens for the minimum film thickness at $2\pi f t = \pi$. Indeed, there is a 2.2% relative difference between the current model and the one developed by Liu et al.[114]. The main differences between the two models reside in the calculation of the elastic displacement of the solids. Nevertheless, the present model is able to represent the film thickness variations in an isothermal contact subjected to a sinusoidal load.

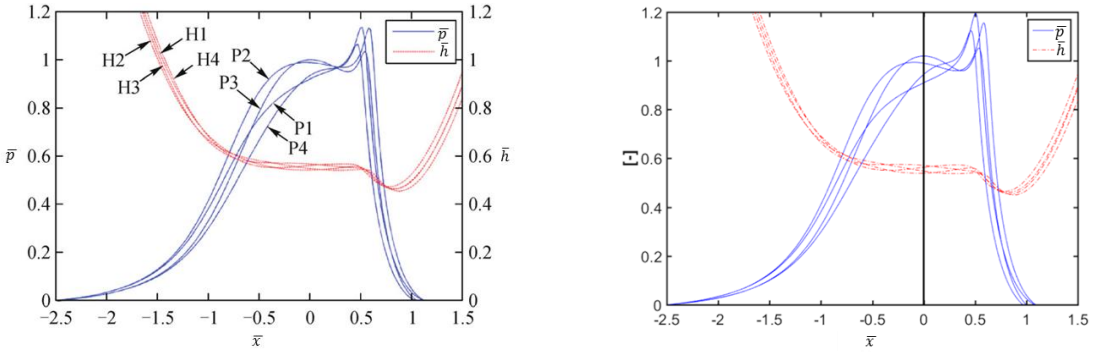

Figure 2.3-1 – Dimensionless pressure and film thickness profiles under the transient load defined in eq. 2.3-1. On the left, the reference case defined by Liu et al.[114]*. On the right, the results taken from the model introduced in this chapter.*

	$\overline{p_c}$		$\overline{h_c}$		$\overline{h_m}$	
$2\pi f t$	Liu	Meziane	Liu	Meziane	Liu	Meziane
$\pi/2$	0.99	0.99	0.55	0.55	0.45	0.45
π	1.00	1.02	0.57	0.57	0.46	0.45
$3\pi/2$	0.93	0.94	0.56	0.56	0.46	0.46
2π	0.92	0.91	0.54	0.54	0.47	0.46

Table 2.3-2 – Dimensionless values of the central pressure, the central film thickness and the minimum film thickness under the transient load defined in eq. 2.3-1. The values obtained by Liu et al. [114] *are reported alongside the results taken from the model introduced in this chapter.*

Liu et al.[114] also studied the problem of a contact subjected to a sudden decrease of the entrainment velocity from $0.1\, m.s^{-1}$ down to 0 (see eq. 2.3-2). The load is considered constant during the whole process, with the value w_0^{1D}. The dimensionless pressure and film thickness profiles are represented in Figure 2.3-2 at three different moments ($t_1 = 0\, ms, t_2 = 0.2212\, ms$ and $t_3 = 0.8715\, ms$). The corresponding values of central pressure, central film thickness and minimum film thickness are reported in Table 2.3-3.

$$u_1(t) = u_2(t) = \begin{cases} 0.1\, m.s^{-1} & \text{for } t = 0 \\ 0 & \text{for } t > 0 \end{cases} \qquad \text{eq. 2.3-2}$$

For all measured values, the maximum relative difference happens for the minimum film thickness at $t = t_3$. Indeed, there is a 4.2% relative difference between the current model

and the one developed by Liu et al.[114]. As such, the current model is able to reproduce a contact subjected to a sudden loss of entrainment velocity.

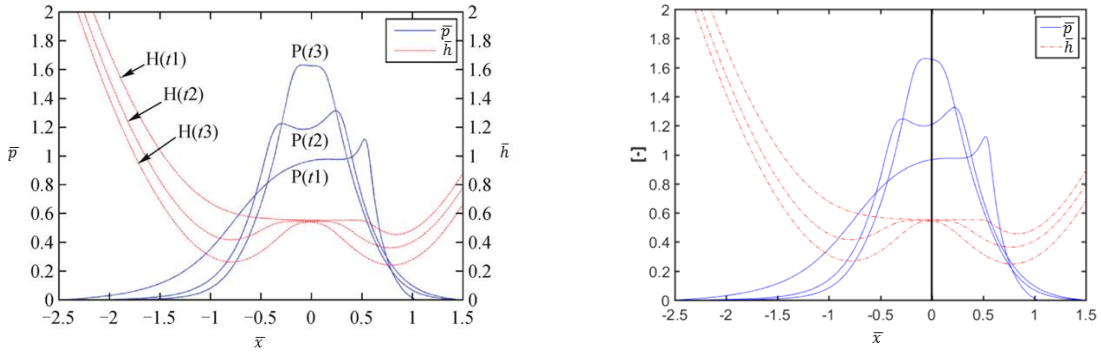

Figure 2.3-2 – Dimensionless pressure and film thickness profiles under the transient entrainment velocity defined in eq. 2.3-2. On the left, the reference case defined by Liu et al.[114]*. On the right, the results taken from the model introduced in this chapter.*

	$\overline{p_c}$		$\overline{h_c}$		$\overline{h_m}$	
t	Liu	Meziane	Liu	Meziane	Liu	Meziane
t_1	0.97	0.97	0.55	0.55	0.45	0.45
t_2	1.20	1.21	0.55	0.55	0.36	0.36
t_3	1.63	1.66	0.54	0.54	0.24	0.25

Table 2.3-3 – Dimensionless values of the central pressure, the central film thickness and the minimum film thickness under the entrainment velocity defined in eq. 2.3-2. The values obtained by Liu et al. [114] *are reported alongside the results taken from the model introduced in this chapter.*

The two transient calculations conducted by Liu et al.[114] are replicated with the current model.

2.3.2 Experimental validation of the 2D model in stationary ZEV condition

A reference case is defined for the experiments and 2D model with a velocity of $5\ m/s$, a load of $50\ N$ and an external temperature of $293.15\ K$. The corresponding experimental and numerical film thickness profiles are represented in Figure 2.3-3. The asymmetrical nature of the results is discussed in 2.3.4.

For the 2D variant of the model, the value of central film thickness presents a 2.8% difference with the experimental value whereas a 23.9% difference exists for the minimum film thickness. This difference is of the same order than the ones reported in other works [26] for classical pure rolling conditions.

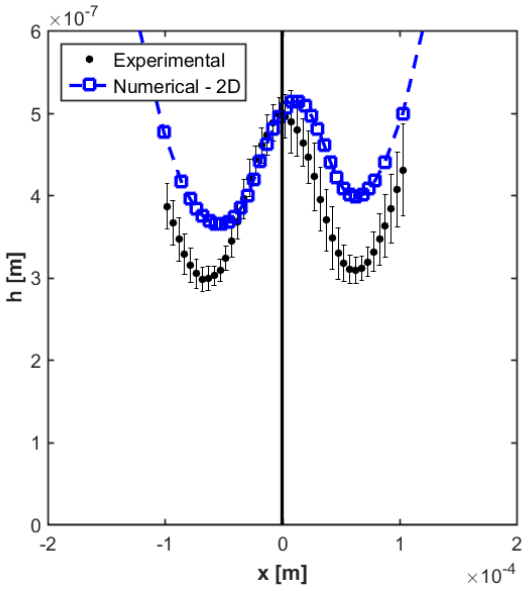

Figure 2.3-3 – Film thickness profiles for the reference case ($u = 5\ m/s$, $w^{2D} = 50\ N$ and $T_0 = 293.15\ K$), from experiments (along the dashed line in Figure 2.2-4) and simulations. The average value for 6 interferograms is represented. The error bars correspond to three times the standard deviation. The asymmetrical nature of the curves is explained in 2.3.4.

2.3.3 Discussion on the 1D hypothesis

The model presented in this chapter will be used to calculate either the infinitely long cylinder-on-plane line contact (i.e 1D variant), or the barrel-on-plane wide point contact (i.e 2D variant). In rolling EHL, Nijenbanning et al. [30] proposed a similar approach, where the 1D and 2D variants of their model were compared for wide point contacts. They found that in the direction of entrainment, the film thickness found in the 2D model along the central line ($y = 0$) could be described by the 1D model for ellipticity ratios $D < 0.1$. When this condition is met, wide point contacts can be studied along the entrainment direction as if it was an infinitely long cylinder in the y direction. The equivalence between the two variants of the model (1D and 2D) is assured by having the same Hertz pressure ($p_h^{1D} = p_h^{2D}$). Consequently, an equivalent 1D approximation of the central line of the 2D wide point contact is defined:

$$\begin{cases} R_{eq}^{1D} = E' a^{2D} / 4 p_h^{2D} \\ w^{1D} = \pi p_h^{2D} a^{2D} / 2 \end{cases} \qquad \text{eq. 2.3-3}$$

In 1D, the reference case has a normal load per unit length of $5.82 \times 10^4\ N.m^{-1}$, and the equivalent radius of contact is $R_{eq}^{1D} = 0.0128\ m$. For these reference cases, the experimental and numerical film thickness profiles are represented in Figure 2.3-4. The asymmetrical nature of the results is discussed in 2.3.4.

The value of central film thickness presents a larger difference ($28.3\ \%$ deviation) than for the 2D variant. On the other hand, the numerical minimum film thickness is only 3.3% higher than

the experimental one, with h_m^+ and h_m^- being 0.2% and 6.9% larger respectively. These results are especially good with respect to the other variant of the model.

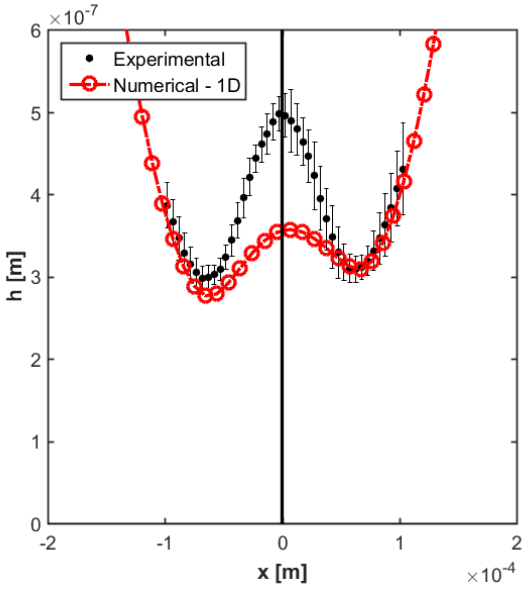

Figure 2.3-4 – Film thickness profiles for the reference case ($u = 5\ m/s$, $w^{1D} = 5.82 \times 10^4\ N.m^{-1}$ and $T_0 = 293.15\ K$), from experiments (along the dashed line in Figure 2.2-4) and simulations. The average value for 6 interferograms is represented. The error bars correspond to three timse the standard deviation. The asymmetrical nature of the curves is explained in 2.3.4.

For the 50 cases studied, the minimum film thickness is predicted by the 1D variant of the model with an accuracy between 0.2% and 23.5%, with the worst cases found at high external temperatures. The experimental values of central film thicknesses may be different when taking the variations of the refraction index into account, which is discussed in Appendix B. In the rest of the document, the 1D variant of the model will be retained both for its ability to predict the minimum film thickness, but also for the reduced calculation times it provides. In the next subsection, the influence of the thermal properties of the solids is discussed.

2.3.4 Discussion on the material properties of the solids

Differences between experimental and numerical results are here discussed with respect to the solid materials. First, the value for the thermal conductivity of steel is questioned. Second, the influence of having a sapphire surface instead of steel is discussed. Last, the steel on steel case is compared to the sapphire on steel one.

Thermal conductivity of steel

The thermal conductivity k of AISI 52100 steel has been a topic of discussion by various researchers. The classical value given in the literature is $k = 46\ W.m^{-1}.K^{-1}$[26]. Reddyhoff[112] argues that the thermal treatment change its value to $k = 21\ W.m^{-1}.K^{-1}$. The influence of the choice of thermal conductivity on the minimum and central film thicknesses is studied by comparing the results labelled “Numerical 1D – Steel(46)/Sapphire”

with “Numerical 1D – Steel(21)/Sapphire”. The legends indicate the detail of each result (Experimental or numerical) as well as the duet of solids in contact. The properties of “Sapphire” and “Steel(46)” are all listed in Table 2.2-1. “Steel(21)” possesses the same properties as “Steel(46)” expect for $k = 21\ W.m^{-1}.K^{-1}$.

Between the two numerical curves, the relative difference is 3.0% for h_m and 1.4% for h_c. This small difference is an indication that this property does not significantly alter the results and that the current choice ($k = 46\ W.m^{-1}.K^{-1}$) is representative of the steel barrel.

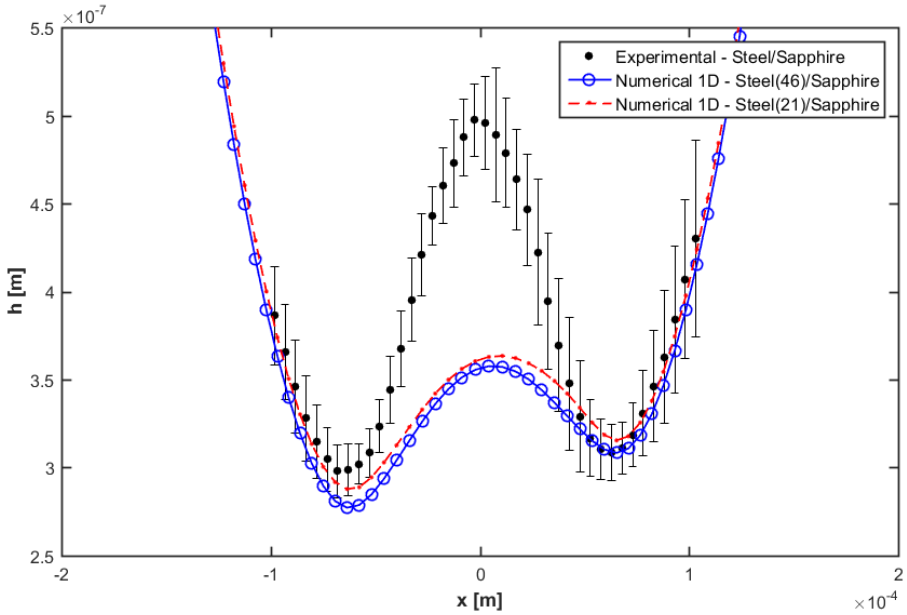

Figure 2.3-5 – Experimental or numerical 1D film thickness profiles obtained for the reference case ($u = 5\ m/s$, $w^{1D} = 5.82 \times 10^4\ N.m^{-1}$ and $T_0 = 293.15\ K$) for different descriptions of the steel.

Impact of material dissimilarity

The validation of the model is made with steel-on-sapphire contacts for experimental purposes. In later sections of this thesis, steel-on-steel contacts will be the focus. It is therefore necessary to understand the differences between the two configurations. As was observed in section 2.3.2, there is a difference between h_m^+ and h_m^- when the contact is between steel and sapphire. This can be seen numerically and experimentally for the steel-on-sapphire contacts in Figure 2.3-6 and Figure 2.3-4. For the reference case, the relative difference between h_m^+ and h_m^- is 4.0% experimentally and 11.3% numerically. The average value between h_m^+ and h_m^-, called h_m, will therefore be used primarily in the rest of this document to describe the minimum film thickness. For the steel-on-steel configuration in Figure 2.3-6, the film thickness is perfectly symmetrical. This result is expected given that the problem is now asymmetrical. Moreover, the film thickness profile obtained for two steel surfaces is very reminiscent of the numerical one obtained with a sapphire disc. There is a 7.82% relative difference for h_c and a 0.63% one for h_m. This means that the validation of the model with a sapphire disc can confidently be extended to steel-on-steel contacts.

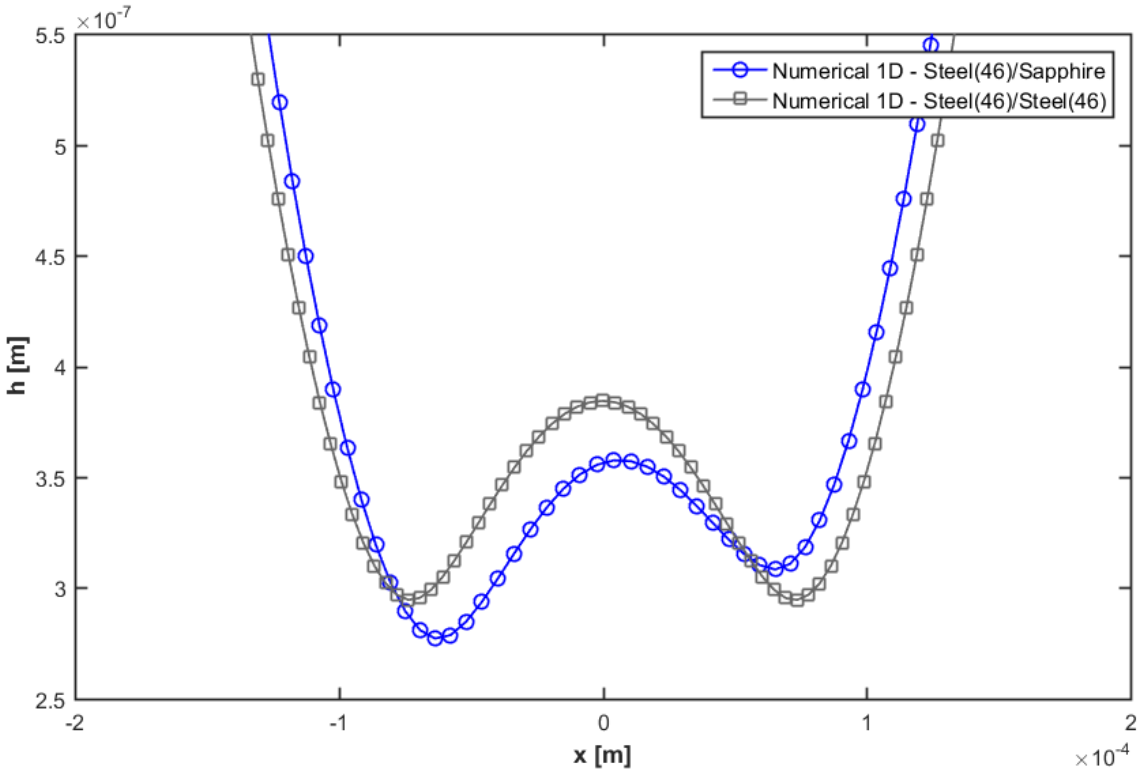

Figure 2.3-6 – Numerical 1D film thickness profiles obtained for the reference case ($u = 5\ m/s$, $w^{1D} = 5.82 \times 10^4\ N.m^{-1}$ and $T_0 = 293.15\ K$) with a variety of solid combinations.

2.4 Conclusion

In this chapter, the numerical and experimental tools used for the study of ZEV contacts are described. Two variants of the same numerical transient thermal EHL model are presented. They enable the calculation of the film thicknesses as well as numerous local quantities in ZEV wide point contacts. The less time-consuming variant assumed an infinitely long cylinder equivalent to the highly elliptical barrel typically found in applications.

After necessary modifications, a tribometer provides the measurements of film thicknesses in barrel-on-plane ZEV contacts. The thermal similarity of sapphire with steel enables optical interferometric measurements while ensuring a quasi-symmetry of the film thickness typically found in steel/steel contacts. The 1D variant of the model predicts the experimental minimum film thickness with great accuracy. However, the central film thickness prediction is less accurate.

This experimental validation of the thermal aspect of the line contact model is done in conjunction with a numerical validation of the transient aspect. The 1D variant of the model will be used in the next chapters for the more extensive study of ZEV contacts.

Chapter 3. Stationary TEHL ZEV contact

3.1 Local description of the viscosity wedge phenomenon 82
3.1.1 Antisymmetric configuration 82
3.1.2 Asymmetric configuration 88
3.2 Influence of the operating conditions 89
3.2.1 Influence of the velocity 89
3.2.2 Influence of the velocity for various contact loads 92
3.2.3 Influence of the velocity for various external temperatures 95
3.3 Conclusion 97

In this chapter, Zero Entrainment Velocity wide point contacts are studied in stationary conditions in the EHL regime using the 1D model. This chapter is divided into two parts. First, the generation of pressure in ZEV contacts is explained through the viscosity wedge principle by linking the various dependent variables in the system. Second, a dual numerical-experimental study is presented in order to show the influence of various operating conditions on the film thickness under ZEV condition[116].

Note: In the following sections, the notions of inlet and outlet are used. Due to the opposite sliding in ZEV contacts, there is an inlet and an outlet for each solid. As such, the inlet of one solid is in close proximity to the outlet of the other solid. In addition, the term "outside of the contact" will be used to refer to any event occurring at $|x| > a^{1D}$.

3.1 Local description of the viscosity wedge phenomenon

3.1.1 Antisymmetric configuration

The numerical model is exploited to understand the physics at stake and evaluate local quantities. In this section, the cylinder-on-plane contact is studied. The surfaces are made out of steel. As described in Chapter 2, the lubricant chosen is the Shell T9. It follows the Murnaghan[22] (eq. 2.1-9) density law, the modified WLF[23] (eq. 2.1-11) pressure/temperature viscosity correlation and the non-Newtonian formulation by Carreau-Yasuda[24] (eq. 2.1-12). The solid and fluid properties are found in Table 2.2-1 and Table 2.2-2 respectively. The external temperature is $T_0 = 293.15$ K, the equivalent contact radius $R^{1D} = 0.0128\, m$, the velocity $u = 2\, m.s^{-1}$ and the normal load per unit length $w^{1D} = 58198\, N.m^{-1}$.

Compression heat source

Because the viscosity wedge is a thermal process, it is important to first investigate how heat is generated in the contact. The ratio between the total heat source per unit length generated through compression P_c^{1D} over the total heat source per unit length generated P_f^{1D} (absolute values) is less than 0.01%. As such, it is possible to explain the viscosity wedge process by only studying the shear heat source.

Figure 3.1-1 – Profiles of various dependent variables in the contact at $2\ m.s^{-1}$. (a) Shear rate. (b) Shear heat source. (c) Temperature. (d) Viscosity. (e) Shear stress. The vertical lines mark the location of a^{1D}.

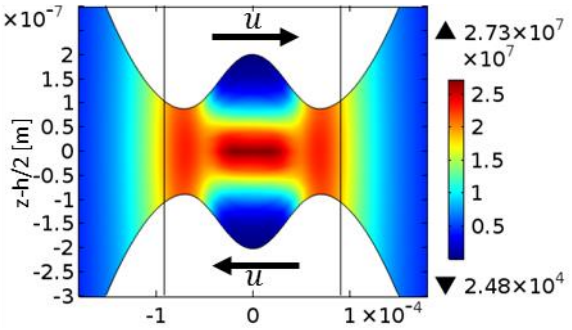

(a) $\dot{\gamma}\ [s^{-1}]$

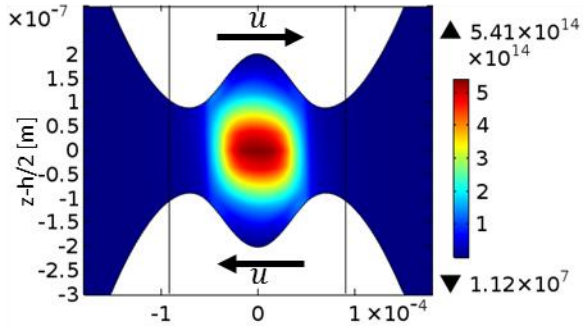

(b) $Q_s\ [W.m^{-3}]$

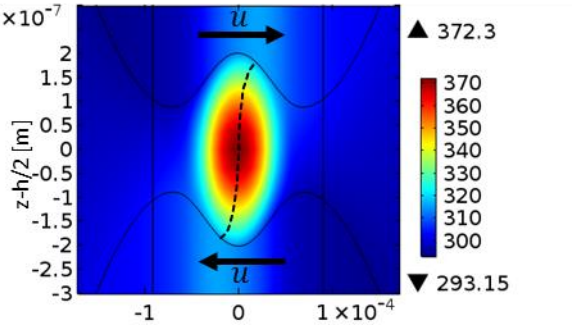

(c) $T\ [K]$

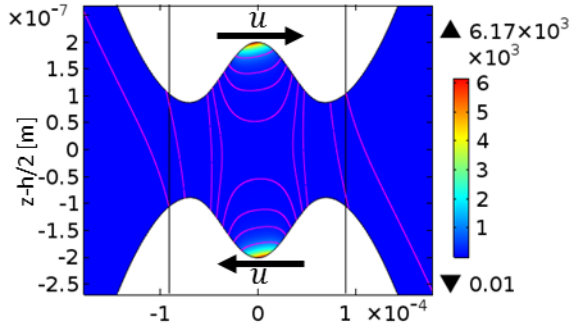

(d) $\eta\ [Pa.s]$ – Isovalues in pink
$\{0.018, 0.026, 0.5, 2, 10, 50, 200, 1000\}\ Pa.s$

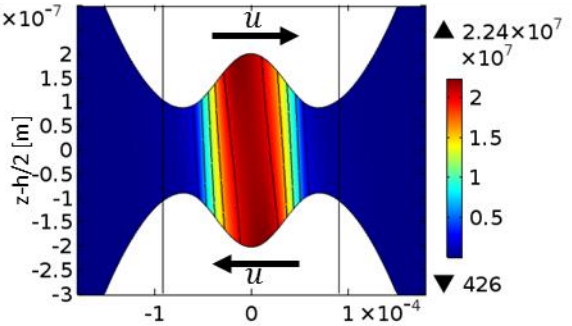

(e) $\tau_{zx}\ [Pa]$ – 5 Isovalues in black

Shear rate

The shear rate profile ($\dot{\gamma}$) is represented in Figure 3.1-1(a). The maximum value ($2.73 \times 10^7\ s^{-1}$) is observed at the center of the contact. High values are also present along the horizontal central line ($z = h/2$) as well as under the location of minimum film thickness ($x = \pm 0.77 a^{1D}$).

Shear heat source

The distribution of the shear heat source is represented in Figure 3.1-1(b). In 1D, the shear heat source is the product of the shear rate times the viscosity. Given that the pressure is much more important at the center of the contact, it is assumed that the viscosity is far more important at the center of the contact than at the location of minimum film thicknesses. As such, the maximum shear heat source ($5.41 \times 10^{14}\ W.m^{-3}$) is found where both the shear rate and the pressure are high, right at the center point of the contact. Outside of the deformed area, the shear heat source stays below $1 \times 10^{14}\ W.m^{-3}$.

Temperature

The temperature distribution is represented in Figure 3.1-1(c). As was just seen, the shear heat source is maximum at the center of the contact ($x = 0$, $z = h/2$). Due to the antisymmetric nature of the contact, the fluid velocity at that point is equal to zero. Therefore, while a lot of heat is generated at the center of the contact, the convection term in the energy equation is zero. Moreover, the boundary conditions of external temperature imposed at a depth into the solids means that heat is conducted from the lubricant to the solids. As such, the fluid is less hot towards the solid/fluid interfaces. The lack of convection at the center of the contact added to the conduction of heat from the fluid to the solids mean that the maximum temperature ($372.3\ K$) is found at the center of the contact.

Due to convection, the hot fluid around the center is entrained towards the outlets of the contact. As such, for any line l such as $z = \chi h$ with $\chi \in [0, 1]$, the maximum temperatures are shifted towards the outlets. The position of the maximum temperature along any line l is represented by the black dotted line. Gradients of temperature (see eq. 3.1-1, shown in Figure 3.1-2) between the two opposite surfaces can therefore be observed. In the present case, the maximum temperature difference is found at $x = \pm 0.52a^{1D}$.

$$\Delta T(x) = T(x, h) - T(x, 0) \qquad \text{eq. 3.1-1}$$

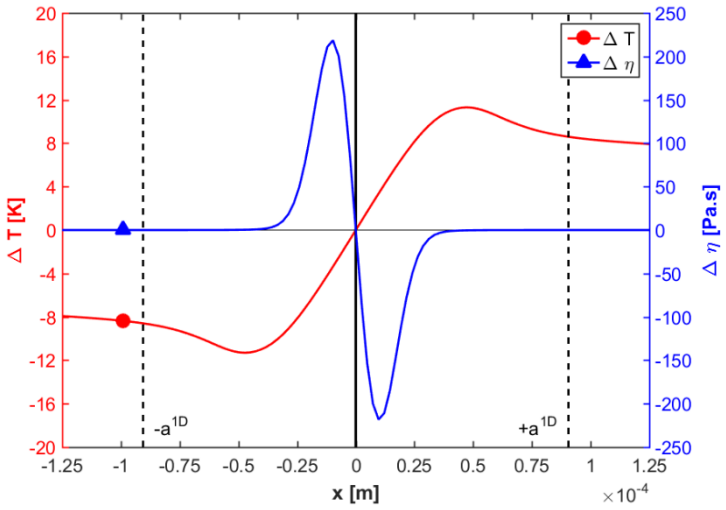

Figure 3.1-2 – Temperature and viscosity differences between the two interfaces at $2\ m.s^{-1}$. The vertical lines mark the location of a^{1D}.

Viscosity

The maximum values of viscosity are found where the pressure is high and the temperature is low, which is close to the coordinates $(0,0)$ and $(0,h)$ in Figure 3.1-1(d). Because of the antisymmetric nature of the problem, the pressure profile is symmetrical around the z-axis. As such, only the temperature can induce vertical viscosity differences (see eq. 3.1-2, represented in Figure 3.1-2) between the lines $z = h$ and $z = 0$.

$$\Delta\eta(x) = \eta(x,h) - \eta(x,0) \qquad \textit{eq. 3.1-2}$$

Shear stress

The product of the shear rate with the viscosity, i.e. the shear stress, is represented in Figure 3.1-1(e). Because of the thin film hypothesis made in section 2.1.1, it is possible to assume that the pressure does not vary along the z-axis. As such, in 1D, the averaging of eq. 2.1-4 leads to eq. 3.1-3:

$$\frac{\partial p}{\partial x} = \frac{1}{h}\int_0^h \frac{\partial p}{\partial x}\,dz = \frac{1}{h}\int_0^h \frac{\partial(\eta\dot{\gamma})}{\partial z}\,dz = \frac{(\eta\dot{\gamma})_h - (\eta\dot{\gamma})_0}{h} = \frac{\Delta(\eta\dot{\gamma})}{h} \qquad \textit{eq. 3.1-3}$$

where $\dot{\gamma} = \partial(u_{f,x})/\partial z$ is the shear rate.

The vertical gradient of shear stress explains the generation of pressure in the contact. The isolines represented provide a visual representation of this gradient.

Pressure

The pressure gradient as well as the pressure are represented in Figure 3.1-3, along with the corresponding Hertz profiles. The maximum pressure gradient is found at $x = \pm 0.40a^{1D}$. Because of this proximity to the contact center, the pressure in the periphery of the contact ($0.40a^{1D} < |x| < a^{1D}$) is lower than the Hertz distribution. For a constant load, this is compensated at the center of the contact where the pressure is 1.77 times higher than the Hertz maximum pressure. This specificity has been observed by other authors ([68], [70], [72], [113]). It should be an important concern when designing practical applications or experiments and when using viscosity models that are not suited for high pressures.

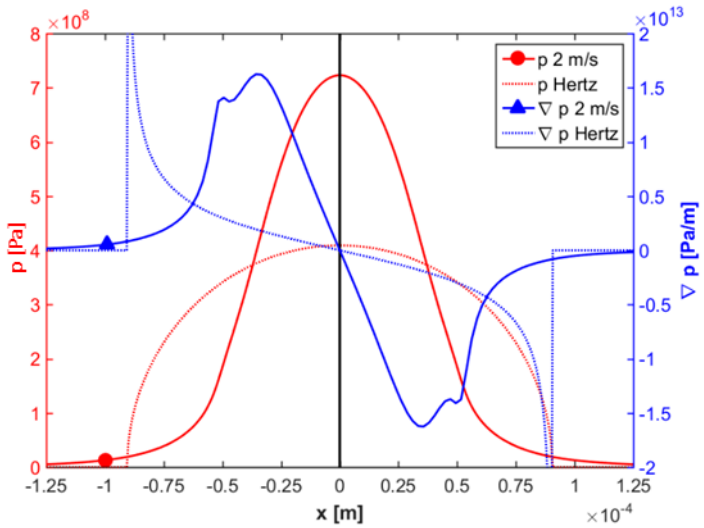

Figure 3.1-3 – Pressure and pressure gradient at $2\ m.s^{-1}$ and the reference Hertz dry contact.

The pressure distribution can be separated in three regions described in eq. 3.1-4. $\Omega_{p,o}$ stands for the outside of the Hertz area, $\Omega_{p,p}$ is at the periphery of the contact and $\Omega_{p,i}$ is the central region. In each region, the relative contribution $\bar{c}|_{\Omega}$ of any subdomain Ω to the total load bearing capacity can be calculated as in eq. 3.1-5.

$$\Omega = \begin{cases} \Omega_{p,o} & \text{for } |x| > a^{1D}; \\ \Omega_{p,p} & \text{for } 0.40a^{1D} < |x| < a^{1D} \\ \Omega_{p,i} & \text{for } |x| < 0.40a^{1D} \end{cases} \qquad \textit{eq. 3.1-4}$$

$$\bar{c}|_{\Omega} = \frac{\int_{\Omega} p\, dx}{w^{1D}} \qquad \textit{eq. 3.1-5}$$

Note: By definition $\Omega_p = \Omega_{p,o} + \Omega_{p,p} + \Omega_{p,i}$, $\bar{c}|_{\Omega_p} = 1$.

The corresponding values are reported in Table 3.1-1, for both the Hertz pressure profile and the pressure profile in ZEV. The Hertz profile is classically chosen as a reference in the case of rolling EHL contacts.

		Region		
		$\Omega_{p,o}$	$\Omega_{p,p}$	$\Omega_{p,i}$
Pressure distribution	Hertz	0%	50.4%	49.6%
	ZEV	2.0%	22.1%	75.9%

Table 3.1-1 – Relative contribution (in %) to the load bearing capacity $\bar{c}|_{\Omega}$ for the pressure distribution as defined by Hertz[47] *and the one calculated under ZEV condition.*

In the ZEV case, 2.0% of the load bearing capacity is built-up in region $\Omega_{p,o}$. As was previously seen, the existence of a pressure gradient (in blue in Figure 3.1-3) can only be attributed to temperature gradients across the film thickness, since no pressure gradient exists in the Hertz definition. This means that non-negligible temperature differences exist outside of the contact.

In region $\Omega_{p,p}$, the contribution to the load bearing capacity is 28.3 points lower than in the Hertz distribution. As such, in region $\Omega_{p,i}$, the load bearing capacity under ZEV condition is 26.3 point higher than in the Hertz distribution($28.3 - 2.0 = 26.3$). This corresponds to the shape of the pressure gradient, which attains its maximum at $x = \pm 0.40a^{1D}$ whereas the maximum pressure gradient is attained at $x = \pm a^{1D}$ in dry contacts (Hertz distribution). In ZEV condition, the high central pressure causes an important displacement of the solids (maximum displacement $\delta_{max} = 2.19\ \mu m$), localised at the center of the contact, which explains the observation of a dimple film thickness profile.

Figure 3.1-4 shows the couplings between the various dependent variables in the system. It highlights how the different control parameters can influence the dependant variables. Moreover, the complex behaviour of ZEV contacts can be inferred from the multiple coupling between variables.

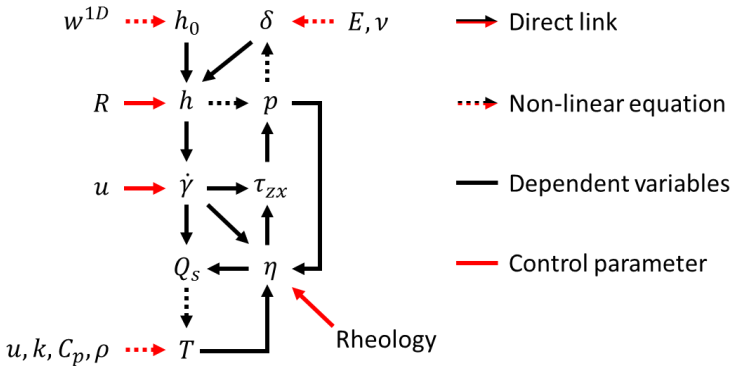

Figure 3.1-4 – Different links between the control parameters and dependent variables in ZEV contacts.

To summarise, in the ZEV case, hot fluid is generated at the center due to high shearing. The hot fluid close to the surfaces is entrained by them outside of the contact creating vertical temperature differences and by extension viscosity differences. The viscosity differences are magnified closer to the center where the pressure is higher. The maximum pressure generation happens quite close to the center of the contact. To respect the load balance of the system, this leads to very high central pressures. The subsequent high elastic surface displacement at the center explains the observed dimple.

3.1.2 Asymmetric configuration

To explain the small asymmetry observed in the experimental and numerical results presented in Chapter 2, the temperature distribution obtained numerically for the steel/sapphire pairing is plotted in Figure 3.1-5, with h_m^- and h_m^+ on the left and right respectively.

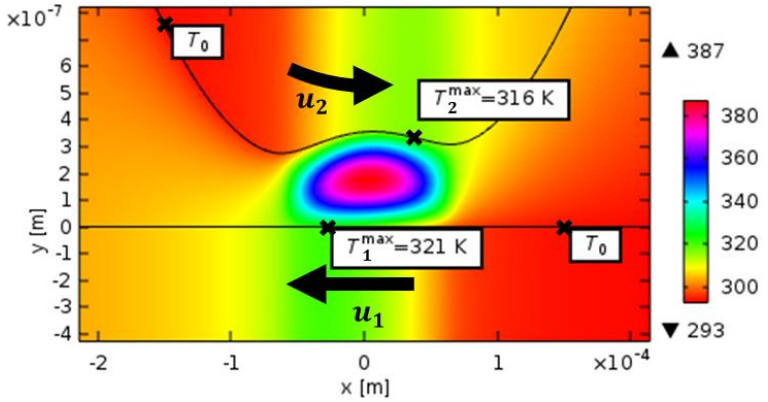

Figure 3.1-5 – Temperature variation in the fluid and solids for the reference case ($u = 5\ m/s$, $w^{1D} = 5.82 \times 10^4\ N.m^{-1}$ and $T_0 = 293.15\ K$). The equivalent body displacement is assigned to the top solid (steel). The bottom solid (sapphire) is considered rigid.

Because of the boundary conditions applied to the thermal model, the fluid enters the contact on both sides at the external temperature, as indicated by the mentions "T_0". Multiple steps explain the viscosity wedge process, similarly to the previous section:

- The top surface moves from the left to the right and the bottom surface moves from the right to the left;
- There is an important shear heat generation in the contact, with a total heat source per unit length generated (eq. 2.1-24) of $P_f^{1D} = 14372\ W.m^{-1}$;
- The fluid temperature rises significantly, with a maximum and central temperature increase of $94\ K$;
- The hot fluid at the center is driven out of the contact on both sides, creating differences in temperature between the inlet and outlet fluid;
- These temperature differences lead to viscosity gradients, themselves causing the generation of pressure.

The temperature and viscosity differences ΔT and $\Delta\eta$ between the two solid/fluid interfaces, as defined in eq. 3.1-1 and eq. 3.1-2, are plotted in Figure 3.1-6. Pressure generation is proportional to the viscosity times shear rate difference between the two surfaces, which explains how the viscosity wedge is responsible for a load bearing capacity. This equation also gives indications as to why the film thickness is asymmetrical in the sapphire/steel configuration. Because the thermal characteristics of both solids differ, heat is not exchanged at the same rate at each fluid/solid interface. Indeed, for the reference case, a power per unit length of $7285\ W/m$ is being evacuated through the fluid/steel interface while $7055\ W/m$ is transferred through the fluid/sapphire interface. The maximum temperature on each interface is $316\ K$ for the top surface and $321\ K$ for the bottom one, as seen in Figure 3.1-5.

$\Delta\eta$, which is magnified closer to the center due to high pressures, also show differences. The maximum value of $\Delta\eta$ on the left ($48.2\ Pa.s$) is indeed higher than on the right ($7.0\ Pa.s$). With more pressure generated on the left side of the contact, the pressure and displacement profiles are slightly shifted to the right. This explains the asymmetry observed in the film thickness.

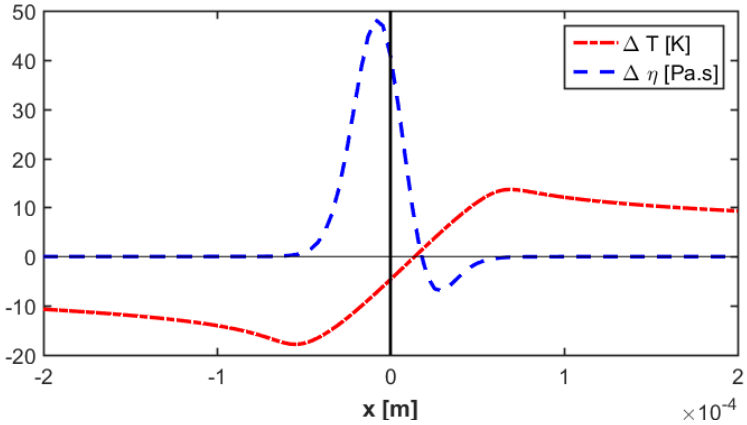

Figure 3.1-6 – Numerical temperature and viscosity differences between the two interfaces, in the reference case ($u = 5\ m/s$, $w^{1D} = 5.82 \times 10^4\ N.m^{-1}$ and $T_0 = 293.15\ K$), for a steel on sapphire contact.

3.2 Influence of the operating conditions

In this section, the influence of the operating conditions on the film thickness in stationary EHL contacts under ZEV condition is discussed. The experimental configuration described in Chapter 2 is studied here. The industrial lubricant T9 follows the Murnaghan[22] (eq. 2.1-9) density law, the modified WLF[23] (eq. 2.1-11) pressure/temperature viscosity correlation and the non-Newtonian formulation by Carreau-Yasuda[24] (eq. 2.1-12). Table 2.2-1 gives the values of the parameters for the steel and sapphire solids. Table 2.2-2 gives the values of the parameters for the fluid. The study focusses on the influence of the velocity, load and external temperature on the minimum and central film thicknesses. All cases are reported in Table 2.2-3.

3.2.1 Influence of the velocity

Under the hypothesis discussed in Chapter 2, the 1D model is used to calculate an approximation of the film thickness. The imposed normal load per unit length is $w^{1D} = 5.82 \times 10^4\ N.m^{-1}$ (which corresponds to $w^{2D} = 50\ N$) and the external temperature is $T_0 = 293.15\ \mathrm{K}$. The minimum imposed surface velocity is chosen to preserve the disc from damage and the maximum value is imposed by the servomotors. The numerical model is used to reach higher velocities up to $u = 17.7\ \mathrm{m.s^{-1}}$. The variations of the experimental and numerical (1D model), central and minimum film thicknesses with the velocity are represented in Figure 3.2-1. The relative difference between the numerical and experimental results are between 0.3% and 11.6%. As such, the 1D model enables the accurate prediction of the minimum film thickness. The results show an increase of the minimum film thickness with the surface velocity up to $u = 10\ m/s$. Similar observations have been made by previous authors ([68][67][51][72]).

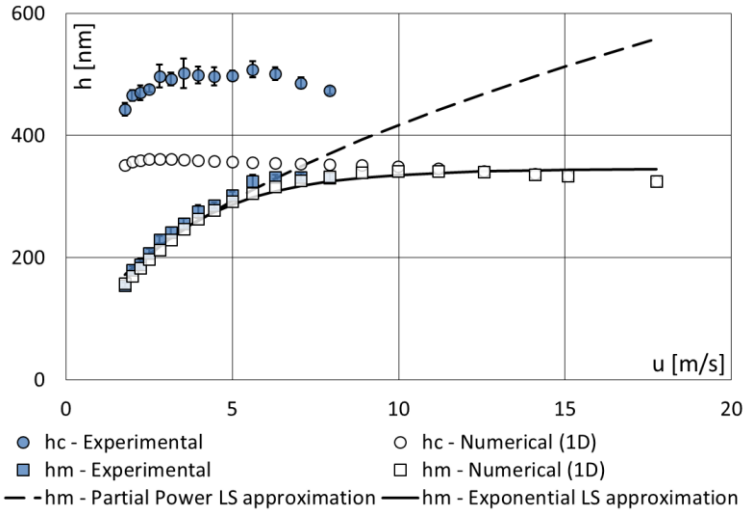

Figure 3.2-1 – Central and minimum film thickness variation with the surface velocity at $w^{1D} = 5.82 \times 10^4\ N.m^{-1}$ and $T_0 = 293.15\ K$. In the experiments, the standard deviation is represented by the black brackets.

The temperature difference between the sapphire disc and the steel barrel is represented in Figure 3.2-2, thanks to the numerical model. At $u = 1.77\ m.s^{-1}$ and $u = 7.92\ m.s^{-1}$, the maximum temperature difference is found at $x = -34\ \mu m$ and at $x = -65\ \mu m$ respectively. This is due to the increase in the convection term of the energy equation with the velocity. Similarly, the maximum pressure gradient is found further away from the center of the contact at higher velocities, as shown in Figure 3.2-2. Indeed, the maximum pressure gradient at $1.77\ m.s^{-1}$ (with a value of 2.1×10^{13} Pa/m) is found at $x = -34\ \mu m$, whereas at $7.92\ m.s^{-1}$, the maximum value (9.0×10^{12} Pa/m) is located at $x = -62\ \mu m$. To summarise, the increase of the minimum film thickness with the velocity is linked with a wider pressure generation, which is due to the increase in the convection of fluid.

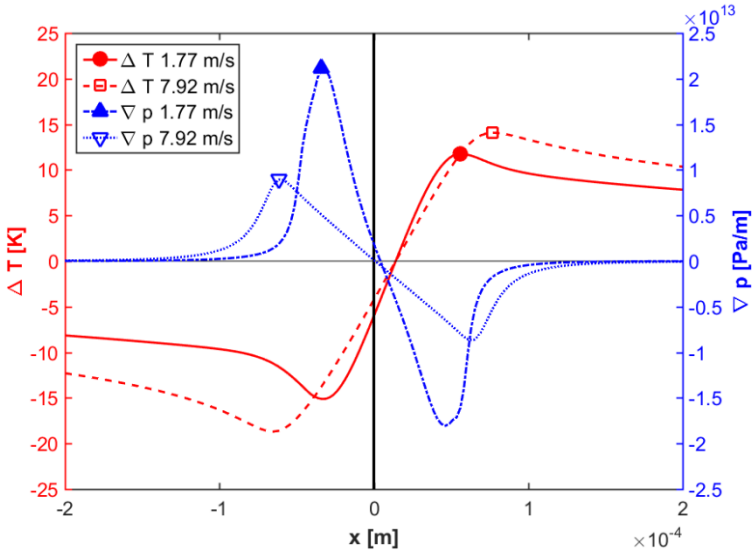

Figure 3.2-2 – Temperature differences (in red, left axis) between the two interfaces and pressure gradient (in blue, right axis) in the fluid at $w^{1D} = 5.82 \times 10^4\ N.m^{-1}$ and $T_0 = 293.15\ K$, for two different surface velocities.

Regarding the central film thickness, absolute differences of up to $130\ nm$ are observed in Figure 3.2-1. They correspond to relative differences between 14.2% and 28.1%. As was discussed in Chapter 2, the 1D model is better able to capture the value of minimum film

thickness than the central one. Despite these differences, the velocity has a small influence on the central film thickness for both the experimental and numerical data. This result is reminiscent of the conclusions made by other authors([68][67][51][72]). As was discussed for the minimum film thickness, the generation of pressure happens closer to the center of the contact at lower velocities. With respect to eq. 2.1-19, the central pressure is therefore higher at lower velocities, as shown in Figure 3.2-3. Indeed, at $1.77\ m.s^{-1}$, the central pressure is $0.79\ GPa$ when it is only $0.48\ GPa$ at $7.92\ m.s^{-1}$, a 64% difference. This increase of the central pressure is directly related to a higher central displacement of the solids, with a 8% increase between $1.77\ m.s^{-1}$ and $7.92\ m.s^{-1}$. This variation is accompanied by an increase of the rigid body separation by 11%. The two variations, being very similar, lead to an overall small variation of the central film thickness with the velocity.

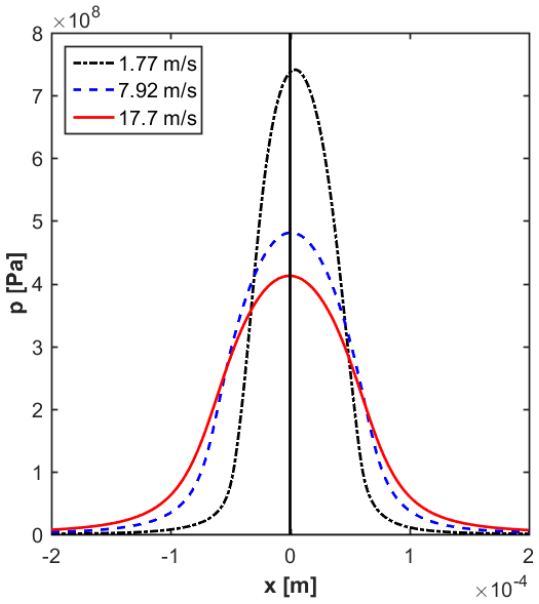

Figure 3.2-3 – Pressure profiles at $w^{1D} = 5.82 \times 10^4\ N.m^{-1}$ and $T_0 = 293.15\ K$, for three different surface velocities.

The cases calculated with high surface velocities(Figure 3.2-1) show that the central and minimum film thicknesses predicted by the 1D model become the same. This is indicative of the disappearance of the dimple. In Figure 3.2-3 at $17.7\ m.s^{-1}$, the pressure profile is the widest and the central pressure the lowest. This leads to lower elastic surface displacement of the contacting bodies, which explains the disappearance of the dimple. At higher surface velocities, a decrease of the central/minimum film thickness is also observed. For more information on the behaviour of ZEV contacts at extremely high velocities, see Appendix C. In rolling EHL theory([10][11]), power law descriptions are often used to predict the minimum film thicknesses separating solids (see eq. 1.3-6 and eq. 1.3-7). Using the experimental data between $1.77\ m.s^{-1}$ and $7.92\ m.s^{-1}$, a least square power law approximation is defined in eq. 3.2-1. It shows a good correlation for the velocities in the experimental data, however, it is unable to fit the numerical data at high velocities.

$$h_{m,power} = h^u_{m,power} \times u^{\alpha^u_{m,power}} \qquad \text{eq. 3.2-1}$$

where u is in $m.s^{-1}$, $h^u_{m,power} = 128.74\ nm$ and $\alpha^u_{m,power} = 0.51$.

To describe the plateau observed at high velocities, another approximation is introduced:

$$h_{m,sa} = h^u_{m,sa} \times (1 - \exp(-u/u^u_{m,sa})) \qquad \text{eq. 3.2-2}$$

where $h^u_{m,sa} = 345\,nm$ and $u^u_{m,sa} = 2.8\,m.s^{-1}$, which respectively represents the film thickness plateau at high velocities and the inverse of the exponential decay constant. These values depend on the other parameters in the system, such as the load. This description better fits the data (the maximum relative difference with the numerical results is 5.7%, and 8.2% for the experimental results) and only relies on two parameters. However, a complete prediction of the minimum film thickness would require a far broader parametrical study.

3.2.2 Influence of the velocity for various contact loads

The influence of the surface velocity on the central and minimum film thicknesses is represented in Figure 3.2-4, both numerically and experimentally for three different loads. The load per unit length (1D) corresponds to the experimental load (2D) (see eq. 2.3-3).

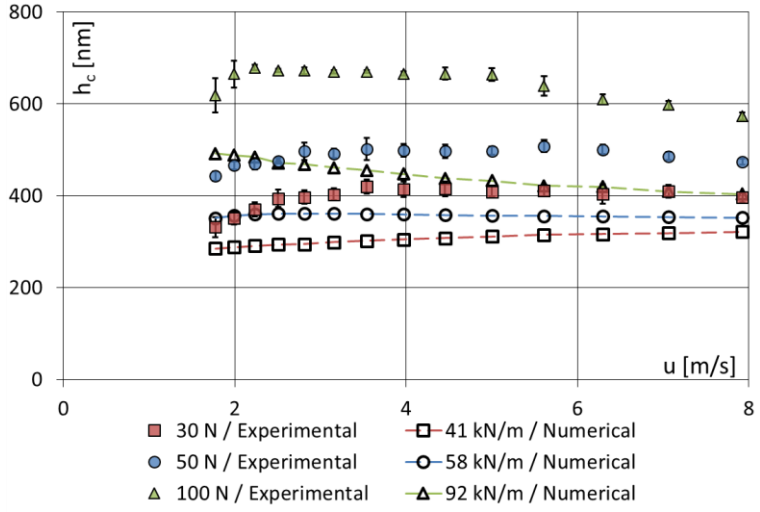

(a)

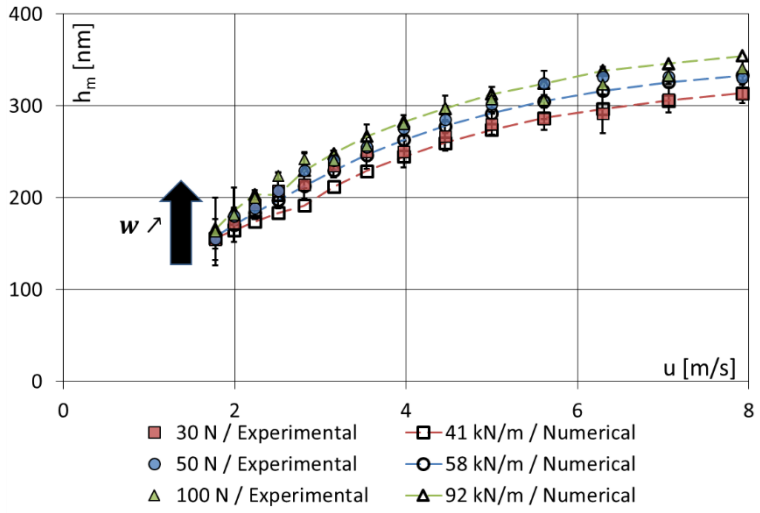

(b)

Figure 3.2-4 – (a) Central and (b) Minimum film thickness variation with the surface velocity for different loads at $T_0 = 293.15\,K$. In the experiments, the standard deviation is represented by the black brackets.

The relative difference between the experimental and numerical data is between 14.2% and 34.8% for the central film thickness and between 0.3% and 15.5% for the minimum film thickness. The minimum film thickness variation is quantitatively well predicted, whereas the calculations only qualitatively resemble the experimental results for the central film thickness. At low load, the central film thickness slightly increases with the surface velocity, whereas at high load the general trend is a global decrease of h_c. An increase of the contact load leads to an increase of the central and minimum film thickness, which is in opposition with the conclusions found in rolling/sliding EHL studied. Previous authors have found similar results in ZEV condition for both line contacts (numerical work only) [51] and point contacts[72]. At $1.77\ m.s^{-1}$, there is a 5.8% increase of the minimum film thickness between $30\ N$ and $100\ N$ and at $7.92\ m.s^{-1}$, the increase is 8.9%. This shows the low influence of the applied load on the minimum film thickness in ZEV velocity contacts compared to other control parameters.

Figure 3.1-4 shows the links between the different variables in the system. It is possible to appreciate the influence of a change in applied load on the state of the contact. An increase of the load leads to an increase of the pressure. This leads to a higher fluid viscosity, and as such, to a greater amount of total heat source ($P_s^{1D} = 11492\ W.m^{-1}$ at $30\ N$ and $P_s^{1D} = 19317\ W.m^{-1}$ at $100\ N$). The strong shear heat generated at high loads lead to higher temperatures at the center of the fluid. Greater temperature differences arise between the contacting surfaces, enhancing the viscosity wedge effect ($14.8\ K$ at $30\ N$ and $22.5\ K$ at $100\ N$).

As shown in eq. 2.1-2, the film thickness is the sum of three terms: the rigid body separation $h_0(x)$, the rigid solid geometry $g(x)$ and the elastic surface displacement $\delta(x)$. These three terms are represented in Figure 3.2-5. On the left side of the Figure (for $x < 0$) the lines show the results for a load per unit length $w^{1D} = 41\ kN.m^{-1}$ (which is equivalent to the experimental contact at $w^{2D} = 30$ N). On the right, the load per unit length is $w^{1D} = 92\ kN.m^{-1}$ (equivalent to $w^{2D} = 100$ N). This representation illustrates the influence of the load on the three constitutive terms of the film thickness. First, as the load increases at $u = 5\ m.s^{-1}$, an increase of the load corresponds to a decrease of the rigid body separation h_0 from $-0.86\ \mu m$ at $30\ N$ to $-2.07\ \mu m$ at $100\ N$. Second, an increase of the load leads to a wider contact. As such, the location at which the minimum film thickness is observed increases. In Figure 3.2-5, the positions at which the minimum film thickness is observed are $|x_{41}| = 0.05\ \mu m$ and $|x_{92}| = 0.09\ \mu m$ for the two loads. This induces an increase of the geometrical term $g(x)$ in the film thickness calculation, from $0.11\ \mu m$ at $30\ N$ to $0.27\ \mu m$ at $100\ N$. Third, stronger elastic displacements of the solids are seen with an increase of the load. Therefore, the displacement δ at the location of minimum film thickness increases with the load ($1.03\ \mu m$ at $30\ N$ and $2.11\ \mu m$ at $100\ N$). When summed together, those three terms compensate each other, which explains the small variations (and even increase) of the minimum film thickness with the load.

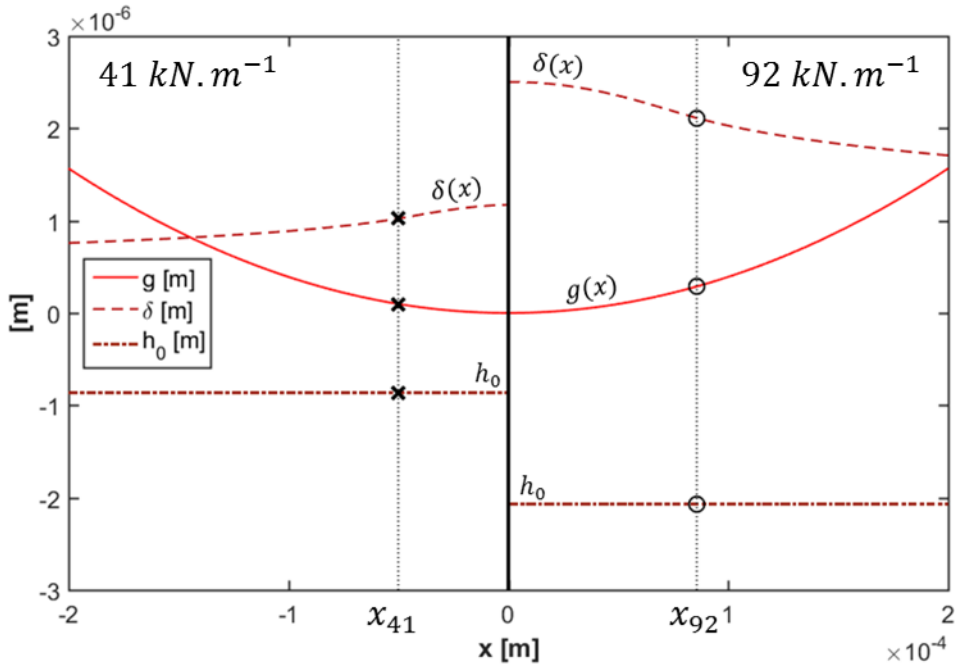

Figure 3.2-5 – Geometrical term $g(x)$, elastic displacement $\delta(x)$, rigid body separation h_0 at $u = 5\ m.s^{-1}$ and $T_0 = 293.15\ K$. On the left $w^{1D} = 41\ kN.m^{-1}$ and on the right $w^{1D} = 92\ kN.m^{-1}$. For each load, the position of the local minimum film thickness is noted by the labels "x_{41}" and "x_{92}" respectively.

Using the formula present in eq. 3.2-2, the values of $h^u_{m,sa}$ and $u^u_{m,sa}$ are determined as a function of the load. Complementary calculations are conducted, so that five loads are swept with twenty-one different velocities. All cases are reported in Table 3.2-1.

$u(m/s)$	$w^{2D}(N)$	$p_h(GPa)$	Equivalent $w^{1D}(N.m^{-1})$
$\{1.77; 1.99; 2.26; 2.51; 2.81; 3.16; 3.54; 3.97; 4.46; 5.00; 5.61; 6.30; 7.06; 7.92; 8.89; 9.98; 11.19; 12.56; 14.09; 15.09; 17.74\}$	10	0.270	1.99×10^4
	20	0.340	3.16×10^4
	30	0.390	4.14×10^4
	50	0.462	5.82×10^4
	100	0.582	9.24×10^4

Table 3.2-1 – Sets of calculations for the sapphire disc (105 total cases).

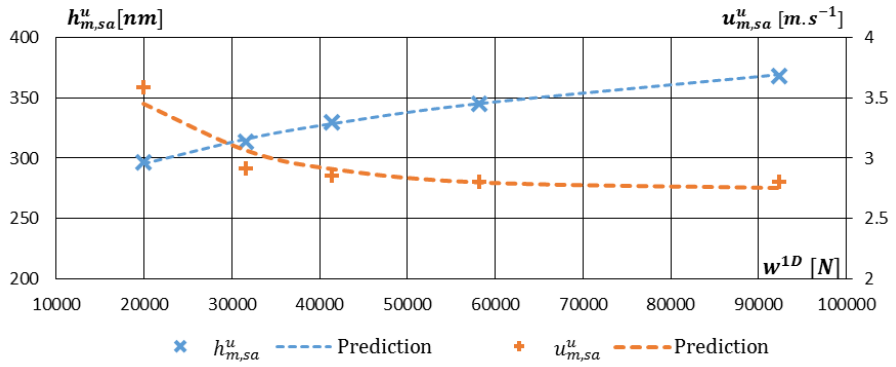

Figure 3.2-6 – Values of $h^u_{m,sa}$ and $u^u_{m,sa}$ as a function of the load.

Figure 3.2-6 presents the variation of $h^u_{m,sa}$ and $u^u_{m,sa}$ as functions of the load. The prediction formulae of these two values are given in eq. 3.2-3 and eq. 3.2-4.

$$h_{m,sa}^{u} = h_{m,sa}^{u,w} \times (w^{1D})^{\alpha_{m,sa}^{u,w}} \qquad \text{eq. 3.2-3}$$

$$u_{m,sa}^{u} = u_{m,sa}^{u,w} \times \left(1 + \exp\left(-\frac{w^{1D}}{w_{m,sa}^{u,w}}\right)\right) \qquad \text{eq. 3.2-4}$$

where w^{1D} is in $N.m^{-1}$. Also, $h_{m,sa}^{u,w} = 69.8\,nm$, $\alpha_{m,sa}^{u,w} = 0.146$, $u_{m,sa}^{u,w} = 2.74\,m.s^{-1}$ and $w_{m,sa}^{u,w} = 14695\,N.m^{-1}$ are *a priori* all functions of the rest of the input parameters in the system.

Figure 3.2-7 shows the semi-analytical prediction developed in the two previous sections along with the experimental and numerical data. The coefficient of determination for the experimental dataset is ${R_d}^2 = 0.96$; for the numerical dataset, it is ${R_d}^2 = 0.98$. For low loads and low velocities ($w^{1D} = 19904\,N.m^{-1}$ and $u \leq 2.233\,m.s^{-1}$), there is a significant relative difference between the results from the model and the semi-analytical formula ($> 10\%$ relative difference). For the rest of the tested parameters, the relative difference is below 6.15%. Note that the present formula is written for a given fluid (Shell T9), between a steel and sapphire surface of equivalent radius $R_{eq}^{1D} = 0.0128\,m$ and for $T_0 = 293.15\,K$. As such, all parameters given in eq. 3.2-3 and eq. 3.2-4 may vary depending on the calculation case.

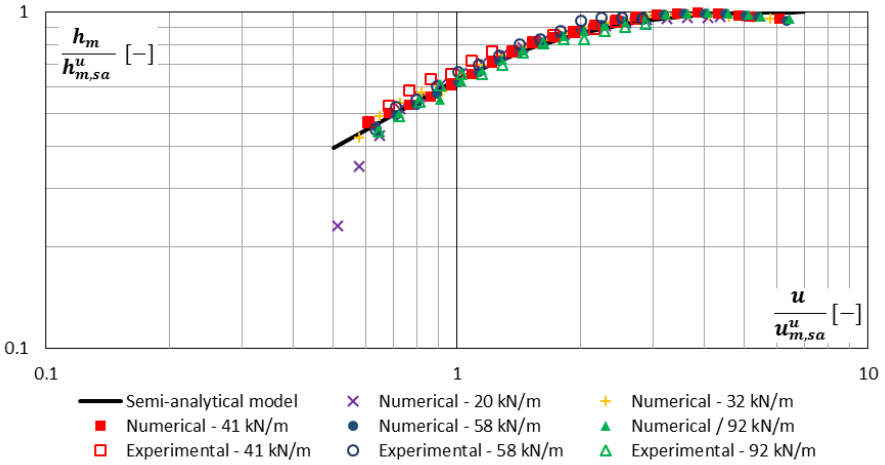

Figure 3.2-7 – Ratio of the film thickness over the value of $h_{m,sa}^{u}$ as a function of the ratio of the velocity over $u_{m,sa}^{u}$.

3.2.3 Influence of the velocity for various external temperatures

The influence of the velocity on the central and minimum film thickness is also investigated for various values of T_0 ($T_0 \in \{293.15; 308.15; 323.15\}\,K$), as shown in Figure 3.2-8.

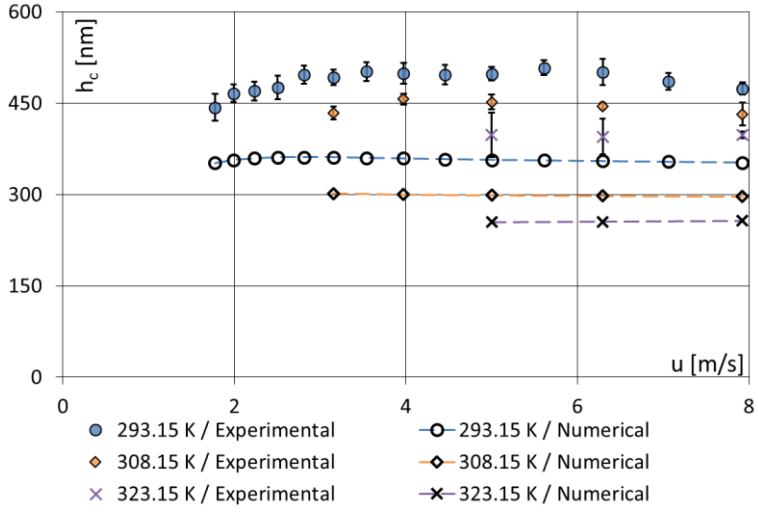

(a)

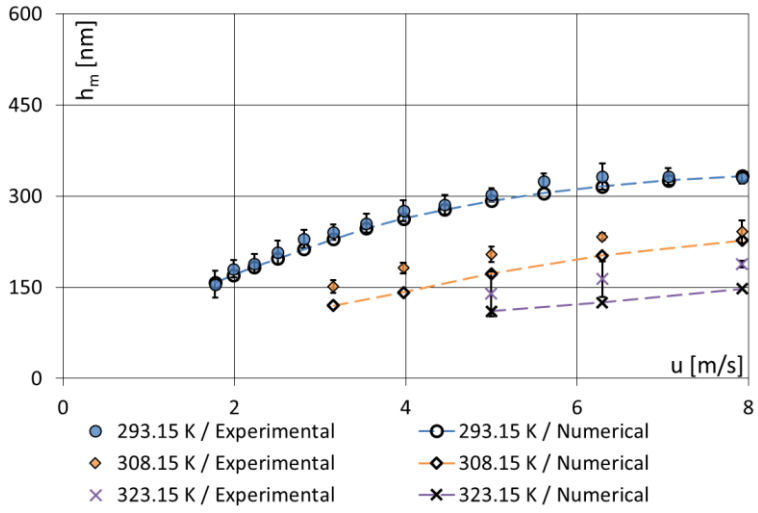

(b)

Figure 3.2-8 – (a) Central and (b) Minimum film thickness variation with the surface velocity for different external temperatures at $w^{1D} = 5.82 \times 10^4\ N.m^{-1}$. In the experiments, the standard deviation is represented by the black brackets.

Both the central and minimum film thickness decrease with the external temperature. Consequently, in order to stay in the full film lubrication regime, the experiments at high temperatures are stopped before reaching $1.77\ m.s^{-1}$ (At $3.16\ m.s^{-1}$ for $308.15\ \mathrm{K}$ and $5.00\ m.s^{-1}$ for $323.15\ \mathrm{K}$). Similarly to previous results, the central film thickness estimated by the model is lower than the experimental one. The highest relative differences between the experimental and numerical minimum film thickness measurements are 11.6%, 22.2% and 23.5% at respectively $293.15\ \mathrm{K}$, $308.15\ \mathrm{K}$ and $323.15\ \mathrm{K}$. An increase of the external temperature leads to a decrease of the ambient viscosity from $0.020\ Pa.s$ at $293.15\ \mathrm{K}$ down to $0.006\ Pa.s$ at $323.15\ \mathrm{K}$. The viscosity differences between the two solids are therefore more important at low external temperatures, as can be seen in Figure 3.2-9. Indeed, the maximum value of $\Delta\eta$ is $48.2\ Pa.s$ at $293.15\ \mathrm{K}$ and $4.2\ Pa.s$ at $323.15\ \mathrm{K}$. These maxima are found further away ($8.62\ \mu m$ to the left) from the contact center at $293.15\ \mathrm{K}$ than at $323.15\ \mathrm{K}$ ($4.32\ \mu m$ to the left). This corresponds to a wider pressure gradient profile at lower external temperatures, as represented in the same Figure.

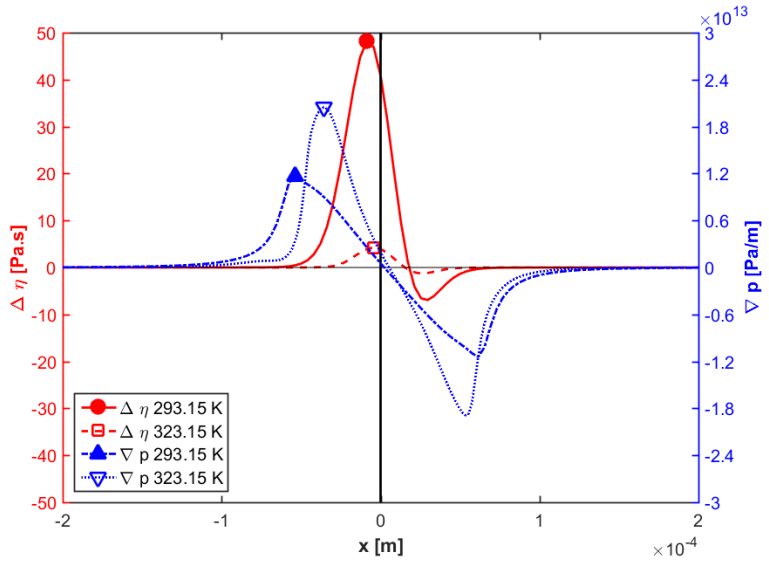

Figure 3.2-9 – Viscosity differences (in red, left axis) between the two interfaces and pressure gradient (in blue, right axis) in the fluid at $u = 5\ m/s$ and $w^{1D} = 5.82 \times 10^4\ N.m^{-1}$, for two different external temperatures.

The pressure profiles in both cases can be found in Figure 3.2-10. In order for the load balance equation to be respected, the wider pressure generation leads to a lower central pressure. Indeed, the central pressure is $5.62 \times 10^8\ Pa$ at 293.15 K and $7.05 \times 10^8\ Pa$ at 323.15 K, a 25% increase. Consequently, the central displacement $\delta(x)$ is larger for hotter contacts ($1.62\ \mu m$ at 293.15 K versus $1.68\ \mu m$ at 323.15 K). However, this increase is too small compared to the decrease of the rigid body separation($1.27\ \mu m$ at 293.15 K versus $1.43\ \mu m$ at 323.15 K). This explains why the central film thickness decreases with the temperature.

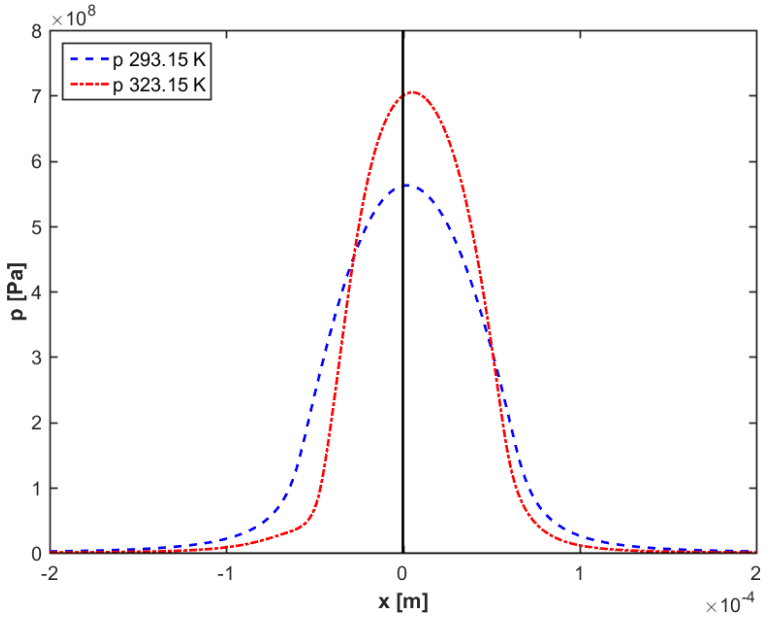

Figure 3.2-10 – Pressure profiles at $u = 5\ m/s$ and $w^{1D} = 5.82 \times 10^4\ N.m^{-1}$, for two different external temperatures.

3.3 Conclusion

It is possible, using the model, to understand how heat is generated in ZEV contacts, and in turn, how temperature differences rise between the contacting bodies. Given how temperature and viscosity are related, the viscosity wedge process can be explained in the

context of Zero Entrainment Velocity. High temperature differences exist within the contact area, which is linked to high pressure gradients quite close to the center. These ultimately lead to a very high pressure at the center of the contact, causing the dimple.

A dual experimental-numerical study of ZEV contacts in stationary conditions is conducted to establish the influence of the surface velocity, the contact load and the external temperature of the central and minimum film thicknesses.

An increase of the surface velocity leads to an increase of the minimum film thickness up to a limit value. The increase is explained by the rising thermal wedge. However, high velocities are synonymous of wide pressure generations, which means less pressure in the contact area. An exponential model is able to reproduce this behaviour for the velocities tested.

An increase of the contact load leads to an increase of the film thickness. This behaviour is counterintuitive when compared to rolling EHL, but can be explained by the fact that high loads lead to strong elastic surface displacements. The semi-analytical model is adapted for a range of loads, and shows a good agreement with the numerical results. However, it should be noted that the range of utilised parameters (load and velocity only) disable the generality of this model since the temperature, materials and geometry are fixed.

Finally, the influence of the external temperature is the same in ZEV as it is in rolling EHL. Indeed, an increase of the external temperature leads to a decrease of the film thickness.

Chapter 4. Squeeze and thermal effects in wide ZEV contacts subjected to varying loads

4.1 Framework 100

4.1.1 Loading process 100

4.1.2 Initial state 102

4.2 Case A : Stationary thermal wedge 102

4.3 Case B : Isothermal squeeze 106

4.3.1 Squeeze from the literature 106

4.3.2 Film thickness variation 107

4.4 Case C : Squeeze and thermal wedge competing in film thickness build-up 109

4.4.1 Reference calculation 109

4.4.2 Influence of the characteristic thermal-transient ratio 110

4.5 Conclusion 113

In stationary conditions, the load bearing capacity of ZEV contacts stems from the presence of temperature gradients across the lubricant thickness. In the case of full complement bearings, ZEV contacts happen in a time dependent environment where two cylinders undergo transient loadings. This influences the thermal state of the contact. Moreover, the squeeze of the lubricant generates a temporary load bearing capacity. The main objective of this chapter is to characterise the respective influence of the squeeze and of the thermal effects on the minimum film thickness. With the help of the numerical model validated in Chapter 2 and Chapter 3 under squeeze and thermal wedge conditions, it is possible to activate/deactivate each effect independently.

In the first section, the framework of this study is defined, with a focus given on a reference loading process. Second, the transient loading of isothermal contacts is studied using the literature as a reference. In the last section, the transient thermal problem and the influence of the loading time are discussed.

4.1 Framework

In the entire chapter, steel is chosen as the material for both solids (see Table 2.2-1). The fluid described in section 2.2.1 is also used here (see eq. 2.1-9, eq. 2.1-11, eq. 2.1-12 and Table 2.2-2). The operating conditions are given in Table 4.1-1. As was specified in Chapter 1**,** there are multiple ways to approach transient loadings in EHL contacts. In this section, the vertical motion of the solids and the applied initial conditions are presented.

$u\ [m.s^{-1}]$	$R_{eq}^{1D}\ [m]$	$T_0\ [K]$	$w_f^{1D}\ [N.m^{-1}]$
3	0.01	293.15	100000

Table 4.1-1 – Operating conditions.

4.1.1 Loading process

In this section, it is assumed that the motion of the rolling elements of a full complement bearing is controlled by the overall dynamics of the bearing. Consequently, the inertia of the rolling elements is neglected. The loading process is done by controlling the load $w^{1D}(t)$ ([117], [118]). Only a single approach between the two bodies is considered. By doing so, only three loading parameters are needed to describe the loading process: the initial load w_i^{1D}, the final load w_f^{1D} and the loading time $t_{Loading}$. The loading starts at $t = 0$. As such, the variation of load with time follows the description in **Error! Reference source not found.**:

$$\frac{w^{1D}(t)}{w_f^{1D}} = \begin{cases} 0.67 \times 10^{-3} + (1 - 0.67 \times 10^{-3}) \dfrac{t}{t_{Loading}} & \text{for } t < t_{Loading} \\ 1 & \text{for } t_{Loading} \leq t < t_{Final} \end{cases} \quad \text{eq. 4.1-1}$$

where $t_{Final} = 100 \times t_{Loading}$ is chosen so that the stead-state is reached in all studied cases.

The model is used to simulate the contact while including or ignoring the thermal or squeeze effects. This will provide information on the independent effects of respectively the squeeze and viscosity wedge effects. The calculation of transient isothermal contacts is also conducted separately. Three cases are therefore considered, as reported in Table 4.1-2.

	Case A : Stationary thermal	Case B : Transient isothermal	Case C : Transient thermal
Thermal effect	X		X
Transient effect		X	X

Table 4.1-2 – Description of the model assumptions for each calculation case.

When the transient effect is ignored, the results correspond to a series of stationary cases. Each time $t < t_{Loading}$ corresponds to a load $w^{1D}(t)$. It is possible to represent any dependent variable (such as the minimum film thickness $h_m(w^{1D}(t))$) as a function of time, even though no transient effects are considered. For $t > t_{Loading}$, the stationary case corresponds to the value obtained at w_f^{1D}.

Given the fact that multiple cases exist and that time variations are present, it is important to introduce the new notations employed in this chapter. In the following sections, the minimum film thickness in case A is noted $h_m^A(t)$ (and accordingly for cases B and C). The notation $h_{m,min}^A$ refers to the minimum value of $h_m^A(t)$ overtime. The value of the elastic surface displacement at the location of minimum film thickness is noted δ_{h_m}. Similarly, the value of the geometrical term at the location of minimum film thickness is noted g_{h_m}.

To study the appearance of thermal effects, a thermal characteristic time needs to be defined. In their study of characteristic times in thermal transient problems, Raisin et al.[20] defined a value of the thermal characteristic time for high slide-to-roll ratios. It was defined as the ratio of the Hertz contact length a^{1D} over the velocity of the fastest moving solid (In this case $|u_1| = |u_2| = u$). However, their definition of a^{1D} was based on an average value of the contact load. Indeed, they assumed a periodic variation of the load with time. As such, the definition of the thermal characteristic time must be adapted to the present study. The final load is therefore chosen as a reference for its definition. This leads to the definition of the thermal characteristic time given in eq. 4.1-2 (This thermal time is constructed by thermal characteristics of the materials. It is shown that it can be simplified to depend only on geometrical properties). Moreover, the dimensionless time $\bar{t}$ (eq. 4.1-3) is introduced to study the influence of the loading time. The ratio $\bar{t_T} = t_T/t_{Loading}$ represents the relative influence of the thermal effects compared to the squeeze effect. It is called the characteristic thermal-transient ratio.

$$t_T = \frac{a_f^{1D}}{u} = 0.07\ ms \qquad \textit{eq. 4.1-2}$$

$$\bar{t} = \frac{t}{t_{Loading}} \qquad \textit{eq. 4.1-3}$$

4.1.2 Initial state

In cases A and C where thermal effects are considered, the initial state is defined by a stationary thermal result (with $w_i^{1D} = 0.67 \times 10^{-3} \times w_f^{1D}$). This initial state presents two particularities. First, the elastic surface displacement is negligible compared to the film thickness, which corresponds to a thermal hydrodynamic regime. Second, the temperature in the entire fluid is subjected to very small variations, which are enough to ensure a stable film thickness under this very small load.

The corresponding temperature distribution is represented in Figure 4.1-1. The maximum temperature increase is $1.1\ K$, which is extremely small compared to what was observed in the previous chapter. The minimum film thickness is $h_m^A(0) = h_m^C(0) = 529\ nm$. The maximum contact pressure is only $0.372\ MPa$. The maximum elastic displacement of the solids is obtained at the location of minimum film thickness, with $\delta_{h_m}^A(0) = \delta_{h_m}^C(0) = 2\ nm$, which is only 0.3% of the value of $h_0^A(0) = h_0^C(0) = 527\ nm$. The film thickness is not null because of temperature gradients, albeit small, between the two contacting surfaces. Therefore, this initial state respects the conditions required for an independent study of the squeeze effect. More details on the contact behaviour of this configuration is given in Appendix D.

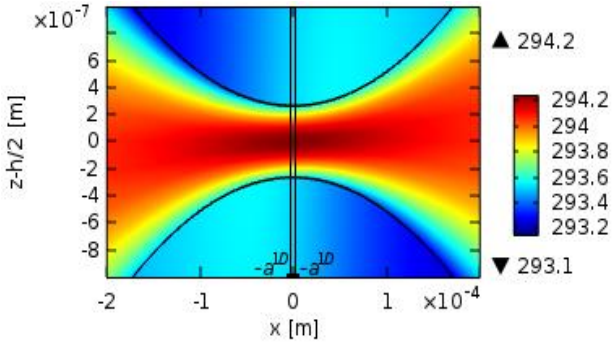

Figure 4.1-1 – Film thickness and temperature profiles in the initial state.

The thermal aspect of the model is not considered in case B. As such, the initial state is defined by fixing h_0 to the value obtained in cases A and C ($h_0^B(0) = 527\ nm$). The consequence is that there is no pressure and no elastic displacement in the initial state for case B. Given the small initial gap, no rebound is expected ([31], [119]).

4.2 Case A : Stationary thermal wedge

This section is dedicated to the study of the load influence on the central and minimum film thicknesses. The variation of the film thickness with the load is represented in Figure 4.2-1. The corresponding variation of the rigid body separation h_0, the elastic surface displacement at the location of minimum film thickness δ_{h_m} and the geometrical term g_{h_m} are represented in Figure 4.2-2.

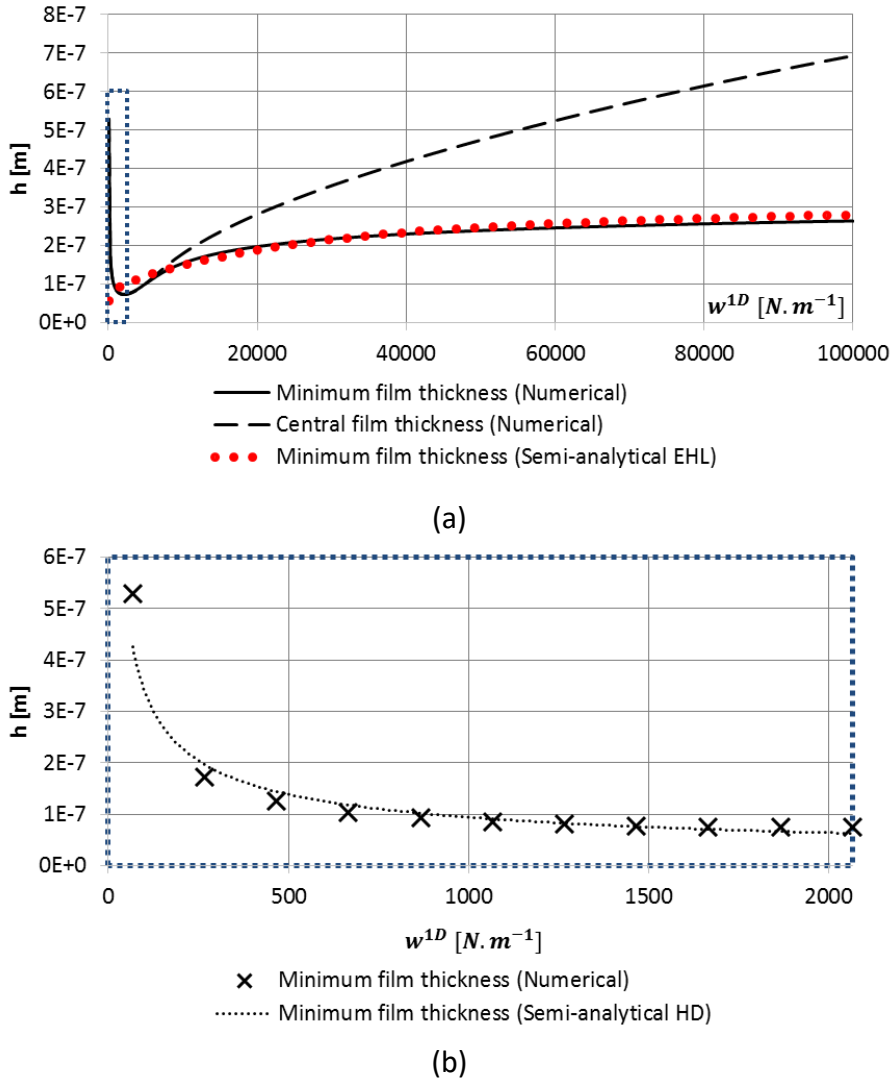

Figure 4.2-1 – (a) Variation of the central and minimum film thickness for all loads considered. (b) Variation of the minimum iflm thickness for low loads. The semi-analytical formula in the EHL regime is described in eq. 4.2-1. For the HD regime, see eq. 4.2-4.

As the load increases from $w^{1D} = 67\ N.m^{-1}$ to $w^{1D} = 2065.7\ N.m^{-1}$, the value of the minimum and central film thicknesses decreases down to $h^A_{m,min} = 74\ nm$. This is associated with a decrease of h^A_0 ($401\ nm$ from $h^A_0 = 412\ nm$ down to $h^A_0 = 11\ nm$) which is far stronger than the increase in the elastic surface displacement ($61.4\ nm$ from $\delta^A_{h_m} = 1.6\ nm$ up to $\delta^A_{h_m} = 63\ nm$). No dimple is observed between these two loads. As such, the geometrical term in the calculation of the minimum film thickness stays nil ($g_{h_m} = 0$). For this range of loads, it is therefore possible to see the thermal hydrodynamic regime applied to ZEV contacts.

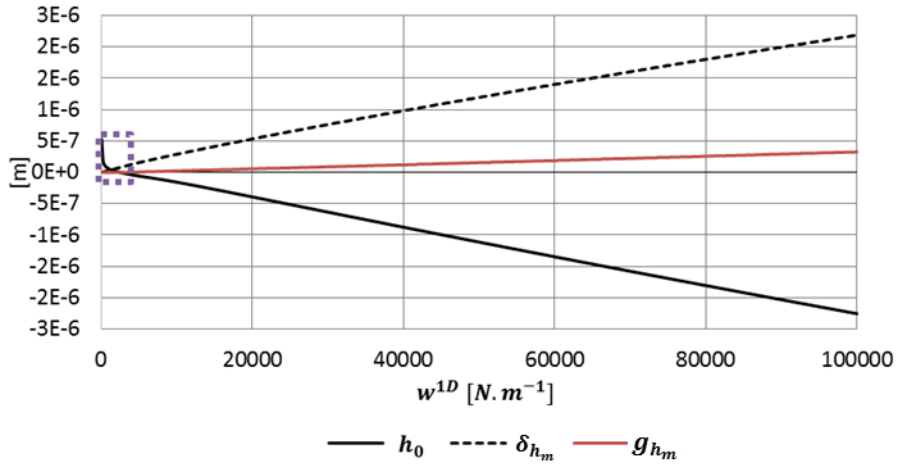

(a)

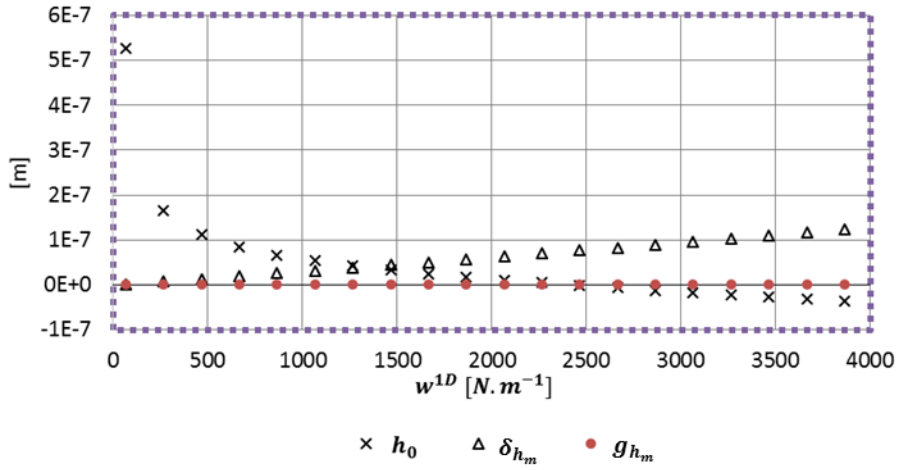

(b)

Figure 4.2-2 – Variation of the rigid body separation, the elastic surface displacement and the geometrical term at the location of minimum film thickness in case A (a) for all loads considered (b) for low loads.

From $w^{1D} = 2065.7\ N.m^{-1}$, an increase of the load is associated with an increase of the minimum film thickness. This corresponds to an increase of the elastic surface displacement stronger than the rigid body separation. Indeed, from $w^{1D} = 2065.7\ N.m^{-1}$ to $w^{1D} = 2265.5\ N.m^{-1}$, the elastic surface displacement increases by $6.4\ nm$ (from $\delta_{h_m}^A = 63.4\ nm$ up to $\delta_{h_m}^A = 69.8\ nm$) and the rigid body separation decreases by $6.3\ nm$ (from $h_0^A = 11\ nm$ down to $h_0^A = 4.7\ nm$). The increase of the elastic surface displacement is an indication that the contact is in the EHL regime.

The dimple apparition is observed at $w^{1D} = 5263.5\ N.m^{-1}$. This corresponds to the load for which the central and minimum film thickness are dissociated. From there, a dimpled film thickness profile is observed for all loads. Moreover, the central and minimum film thicknesses continue to increase. Figure 4.2-1 shows how the increase of the central film thickness with the load is stronger than the increase of the minimum film thickness. These results qualitatively corroborate the ones obtained in Chapter 3.

In Figure 4.2-1, a variation of the semi-analytical model described in Chapter 3 is used to predict the minimum film thickness in the EHL regime ($h_{m,sa}$), assuming that steel/steel contacts are the same as steel/sapphire (see section 2.3.4). It needs to take into account the different radii considered in this chapter. As such, a new formula is defined by multiplying the ratio of radii to some power α^R, as in eq. 4.2-1. The power given is determined by the method of least squares. However, it does not hold any physical meaning given the how close $R_{eq,sa}^{1D}$ and R_{eq}^{1D} are. The semi-analytical formula is not able to predict the film thickness in the HL regime. However, the approximation made in the EHL regime is able to give the value of the minimum film thickness with a good precision (for $w^{1D} > 8000\ N.m^{-1}$, the maximum relative difference between $h_{m,sa}$ and h_m is 6.12%).

$$h_{m,sa} = h_{m,sa}^{u} \times (1 - \exp(-u/u_{m,sa}^{u})) \times \left(\frac{R_{eq}^{1D}}{R_{eq,sa}^{1D}}\right)^{\alpha^R} \qquad \textit{eq. 4.2-1}$$

$$h_{m,sa}^{u} = h_{m,sa}^{u,w} \times (w^{1D})^{\alpha_{m,sa}^{u,w}} \qquad \textit{eq. 4.2-2}$$

$$u_{m,sa}^{u} = u_{m,sa}^{u,w} \times \left(1 + \exp\left(-\frac{w^{1D}}{w_{m,sa}^{u,w}}\right)\right) \qquad \textit{eq. 4.2-3}$$

where $h_{m,sa}^{u,w} = 69.8\ nm$, $\alpha_{m,sa}^{u,w} = 0.146$, $u_{m,sa}^{u,w} = 2.74\ m.s^{-1}$ and $w_{m,sa}^{u,w} = 14695\ N.m^{-1}$, $R_{eq,sa}^{1D} = 0.0128\ m$ and $\alpha^R = -0.42$. In eq. 4.2-1, w^{1D} is in $N.m^{-1}$.

A crude approximation of the film thickness in the hydrodynamic regime is also attempted (between $w^{1D} = 67\ N.m^{-1}$ and $w^{1D} = 2065.7\ N.m^{-1}$) using a power law formulation (see eq. 4.2-4 and Figure 4.2-1). This formulation provides a prediction off by a maximum relative difference of 20%. It serves mostly as a basis for comparison with the EHL region. As seen in eq. 4.2-4, the exponent that describes the variation of the film thickness is $\alpha_{w,HD} = -0.559$, which is negative. This is in contrast with the increase of the minimum film thickness with the load observed in the EHL regime. The exponent $\alpha_{w,HD}$ is quite big (absolute value), which means that the film thickness is very sensitive to a change in load in the HL regime. As such, it should be noted that experimentations on the HL regime are difficult to conduct.

$$h_{m,sa,HD} = h_{m,sa,HD}^{w} \times (w^{1D})^{\alpha_{w,HD}} \qquad \textit{eq. 4.2-4}$$

where $h_{sa,HD}^{w} = 4.47\ \mu m$ and $\alpha_{w,HD} = -0.559$ and w^{1D} is in $N.m^{-1}$. See Figure 4.2-1 for a representation.

In the next section, case B is studied in order to characterise the behaviour of the contact in transient isothermal conditions.

4.3 Case B : Isothermal squeeze

This section is dedicated to understanding the behaviour of isothermal contacts subjected to a time dependent loading (squeeze). First, elements of the literature are used to contextualise the present study. In the second part, the variation of the film thickness in transient isothermal conditions is studied.

4.3.1 Squeeze from the literature

In their numerical study of impacting solids, Dowson and Wang[31] showed the variation of the central and minimum film thicknesses for a solid dropped at a fixed height. Their paper studies a variety of cases. One of them corresponds to the experimental study by Safa and Gohar[85], which is used as a validation for their model. Another case they studied (shown in Figure 4.3-1) at very low initial height is extremely interesting, as it presents no rebound (Larsson and Höglund[119] having concluded the same). Moreover, the load at the end of their loading process stayed at a fixed value, which is reminiscent of the present study. They observed a decrease of the central and minimum film thicknesses, but noted that the value of h_c reached a quasi-constant value.

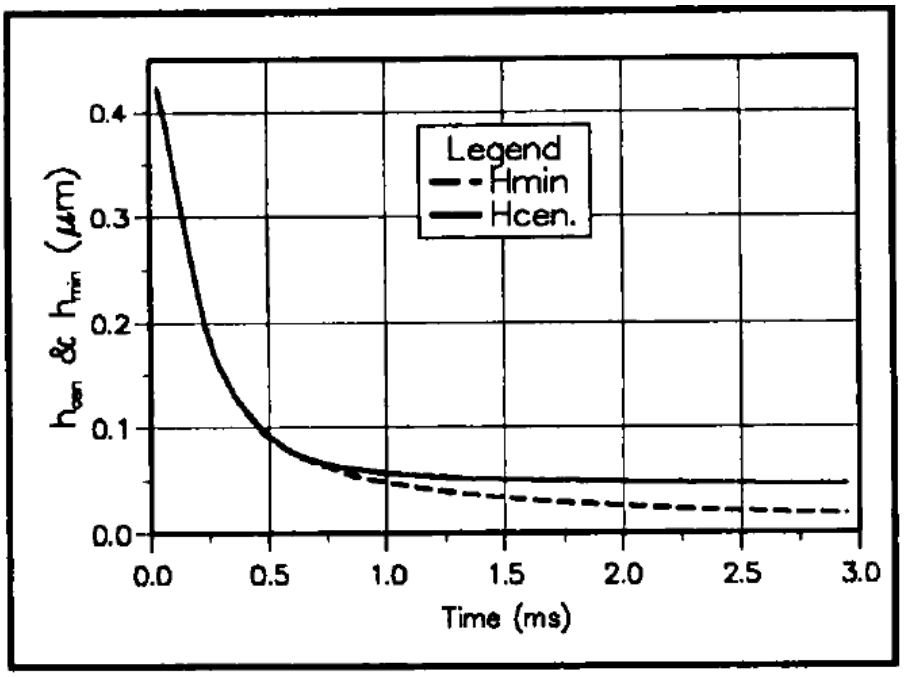

Figure 4.3-1 – Central and minimum film thickness variation for a ball dropped on a plane. Numerical results taken from [31]*, used for a qualitative comparison.*

The central film thickness formula of Wang, Venner and Lubrecht[32] can be used to appreciate this behaviour. Their study assumes a Newtonian fluid that is defined by the density law of Dowson and Higginson[115] and the viscosity law of Roelands[61]. Moreover, their study is done by imposing an initial velocity and taking the mass of the solid into account. As such, a few hypotheses are needed to adapt the formula to the present case. First, the reciprocal asymptotic isoviscous pressure-viscosity coefficient α^* is used to adapt to the usage of the WLF viscosity correlation as defined by Bair[33]. Second, the values of $a^{1D}(\bar{t}=1)$,

$w^{1D}(\bar{t}=1)$ and $p_h^{1D}(\bar{t}=1)$ are used instead of the values used by Wang et al.[32] (b^*, w_1^* and p_h^*). The initial parameters (b^*, w_1^* and p_h^*) took the mass of the solid into account. As such, the usage of the current parameters ($a^{1D}(\bar{t}=1)$, $w^{1D}(\bar{t}=1)$ and $p_h^{1D}(\bar{t}=1)$) enables the semi-analytical model to be used even though the current model does not consider the mass of the solids. In this context, the dimensionless Moes parameters are defined in eq. 4.3-1, and the film thickness formula defined by Wang et al.[32] is adapted in eq. 4.3-2 (superscript $Wang^*$). All complementary values are reported in Table 4.3-1. In the next subsection, the central film thickness calculated at $\bar{t}=1$ will be compared to the prediction adapted from the formula proposed by Wang et al. [32].

$a^{1D}(\bar{t}=1)\ [m]$	$p_h^{1D}(\bar{t}=1)\ [Pa]$	$\eta_0\ [Pa.s]$	$\alpha^*\ [Pa^{-1}]$
1.05×10^{-4}	6.06×10^{8}	0.0195	2.36×10^{-8}

Table 4.3-1 – Parameters used to predict the central film thickness in case B, using the semi-analytical formula by Wang et al. [32].

$$M=\pi\left(\frac{3}{4\lambda^*}\right)^{1/2}$$
$$L=\alpha^* p_{h,f}^{1D}\left(\frac{4\lambda^*}{3}\right)^{1/4} \qquad \textit{eq. 4.3-1}$$

where $\lambda^*=\frac{12\eta_0 {R_{eq}^{1D}}^2}{a_f^{1D}p_{h,f}^{1D}t_{Loading}}$

$$\frac{h_c^{Wang^*}(\bar{t}=1)}{R_{eq}^{1D}\times(U_{DH})^{1/2}}=2.3\times M^{0.2}\times L^{0.55} \qquad \textit{eq. 4.3-2}$$

where $U_{DH}=\frac{1}{2}\left(\frac{L}{\alpha^* E\prime}\right)^4$

4.3.2 Film thickness variation

Figure 4.3-2 shows the variation of the central and minimum film thicknesses in case B for $t_{Loading}=1\ ms$. At the beginning, the vertical velocity is 0, which explains the horizontal tangent for the film thickness curves. Both values continuously decrease overtime, with a minimum film thickness tending towards 0. These results are reminiscent of those obtained by Dowson and Wang[31] for their case with a nil drop height. Indeed, in both their results and the ones presented in this chapter, there is a strong initial decrease of the film thickness during the early stages of the loading process. When the dimple is formed in both cases, the central film thickness barely decreases anymore, while the minimum film thickness is continuously decreasing towards 0.

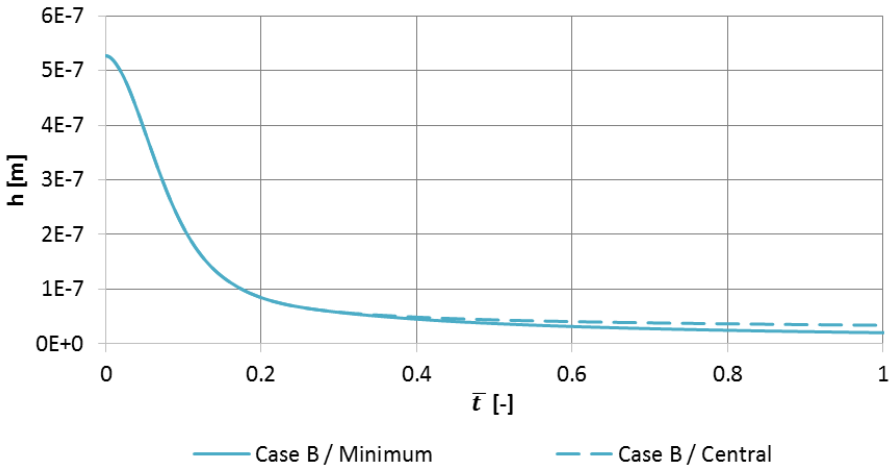

Figure 4.3-2 – Variation of the minimum and central film thicknesses in case B, for $t_{Loading} = 1\ ms$.

The variation of the minimum film thickness is represented in Figure 4.3-3(as a function of $\bar{t}$) for different loading times. In all cases, the film thickness decreases with the loading time. The decrease of the minimum film thickness is relatively quicker for higher loading times. In this Figure, the maximum load is always reached at $\bar{t} = 1$. For $t_{Loading} = 0.01\ ms$, the minimum film thickness has decreased by 33.4% when the maximum load is reached. In contrast, for $t_{Loading} = 100\ ms$, the minimum film thickness has decreased by 99.8%. Therefore, depending on the loading time, the squeeze effect can either be useful for most of the loading process, or completely disappear before the maximum load is reached.

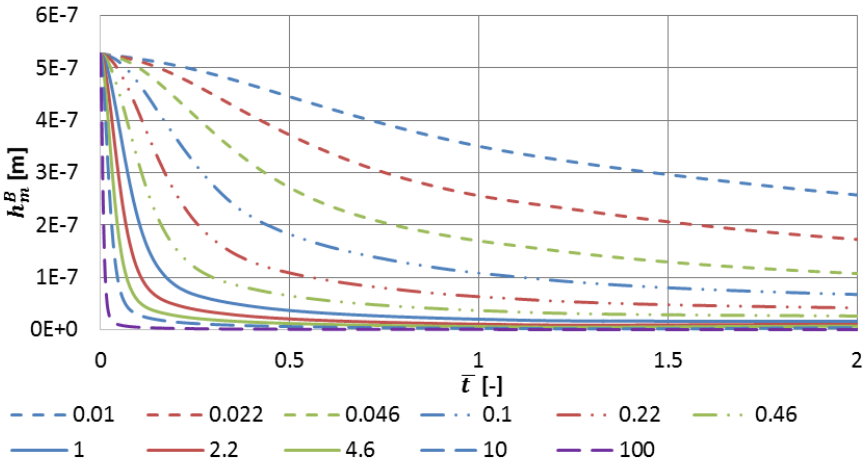

Figure 4.3-3 – Variation of the minimum film thicknesses with $\bar{t}$ in case B for all values of $t_{Loading}$.

Table 4.3-2 contains the values of $h_c^{Wang^*}(\bar{t} = 1)$ and $h_c^B(\bar{t} = 1)$, for all values of $t_{Loading}$. For loading times such as $0.046\ ms < t_{Loading} < 4.6\ ms$, the relative difference is less than 4%. The prediction formula provided by Wang et al.[32] is in good agreement with the results of the present model.

$t_{Loading}$ $[ms]$	$h_c^{Wang^*}(\bar{t}=1)$ $[nm]$	$h_c^B(\bar{t}=1)$ $[nm]$	Relative difference
0.01	404.6	351.0	13.3%
0.022	264.8	256.4	3.2%
0.046	178.2	172.4	3.2%
0.1	117.4	117.5	0.1%
0.22	76.8	76.3	0.6%
0.46	51.7	51.1	1.2%
1	34.0	34.1	0.2%
2.2	22.3	23.0	3.3%
4.6	15.0	15.6	3.9%
10	9.9	10.5	6.4%
100	2.9	3.2	13.0%

Table 4.3-2 – Values of the central film thickness adapted from Wang et al [32] *compared to the value given by the current model in case B, for various loading times.*

The decrease of both the central and minimum film thicknesses is observed over time. However, the value of the central film thickness decreases at a very low rate when the dimple is formed. The prediction formula by Wang et al.[32] is able to accurately predict the value of the central film thickness when the maximum load is reached. For slow loading ramps (high loading times), the film thickness decreases at a higher relative rate. This highlights how the squeeze effect is stronger for faster loadings.

4.4 Case C : Squeeze and thermal wedge competing in film thickness build-up

4.4.1 Reference calculation

The variations of the central and minimum film thicknesses for $t_{Loading} = 1\ ms$ in cases A, B and C are represented in Figure 4.4-1.

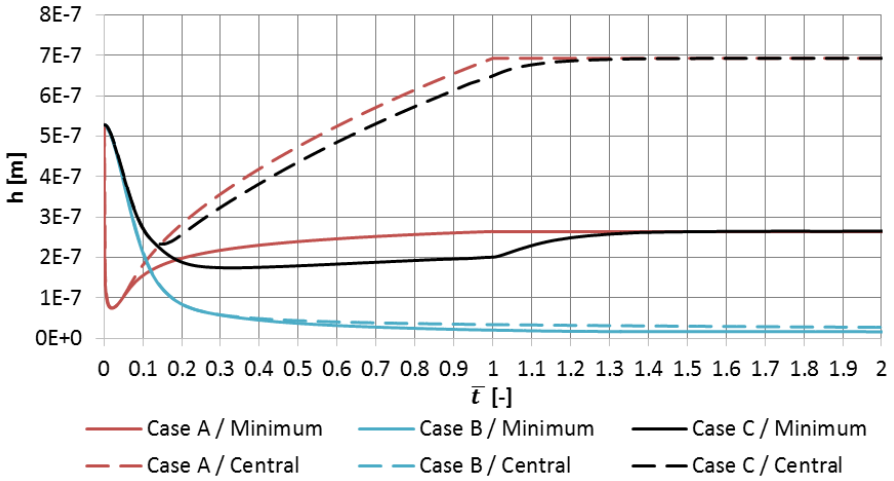

Figure 4.4-1 – Variation of the central and minimum film thicknesses in cases A, B and C, as a function of the dimensionless time $\bar{t}$. The maximum load is reached at $\bar{t}=1$.

When the transient and thermal effects are considered in case C, both the minimum and central film thicknesses follow a non-monotonous variation with time. The time evolution of

h_c^C and h_m^C globally follow the results of case A (stationary thermal), with some differences. At the beginning of the loading process, while case A rapidly reaches a minimum value at $\bar{t} = 0.02$, the decrease in case C closely follows the shape of case B, with a relative difference between the minimum film thicknesses in cases B and C of 0.6%. The squeeze effect is the main reason for the relatively high film thickness at the beginning of case C.

Around $\bar{t} = \bar{t_T} = 0.07$, the film thickness in case C decreases at a slower rate than in case B. At this stage, meaningful thermal effects appear. Moreover, the load is high enough ($w^{1D} = 7062.3\ N.m^{-1}$) that the corresponding film thickness in case A is in the EHL regime, which is associated with an increase of the film thickness with the load(see section 4.2). Soon thereafter, the dimple starts appearing at $\bar{t} = 0.13$.

While the film thickness is continuously decreasing in case B, the minimum film thickness in case C ($h_{m,min}^C = 175\ nm$) is reached at $\bar{t} = 0.372$. The time it takes to reach the minimum value of h_m^C (when transient effects are considered) is 18.6 times greater than the time it takes to reach the minimum value of h_m^A. Moreover, the value of the minimum film thickness is higher in case C, with $h_{m,min}^C / h_{m,min}^A = 2.35$.

As can be seen in Figure 4.4-1, the sudden stop in the loading process (at $\bar{t} = 1$) induces a sudden change of the variation of h_m^C. Indeed, at the instant the final load is attained, the transient term in Reynolds equation (eq. 2.1-8) becomes very close to zero, although not nil since the film thickness is still varying at that instant. From there, only the transient aspects of the thermal equilibrium comes into play, and the steady state is reached at $\bar{t} = 1.368$. This corresponds to approximately five times the characteristic thermal time after the final load is reached ($1 + 5 * \bar{t_T} = 1.35$).

This reference case shows how the squeeze and the viscosity wedge effects are complementary to ensure a separation of the solids involved in a load impact under ZEV condition. The squeeze effect provides an initial but temporary load bearing capacity, delaying the otherwise rapid drop to very small film thicknesses at small loads. This dampening is similar to the one observed by Vichard[97]. At moderate loads, temperature gradients start appearing in the contact, which leads to the emergence of a viscosity wedge effect. Because the strength of both effects may differ, the effect of the loading time (for a given thermal characteristic time) will be analysed in the next section.

4.4.2 Influence of the characteristic thermal-transient ratio

The variation of the minimum film thickness with the dimensionless time $\bar{t}$ is represented in Figure 4.4-2, Figure 4.4-4 and Figure 4.4-3 for various thermal-transient ratios. The value of the minimum film thickness ratio $h_{m,min}^C / h_{m,min}^A$ are reported in Figure 4.4-5 for all values of $\bar{t_T} = t_T / t_{Loading}$.

Slow loading

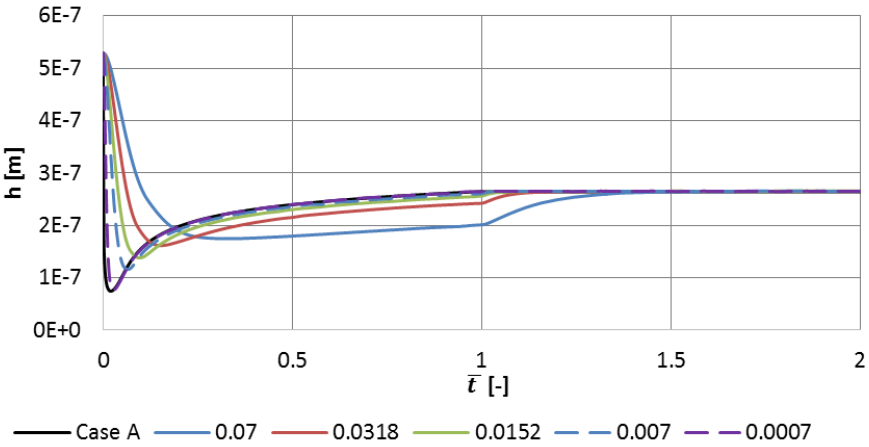

Figure 4.4-2 – Variation of the minimum film thickness in case A and case C, for $\bar{t_T} = \{0.0007, 0.007, 0.0152, 0.0318, 0.07\}$*, as a function of the dimensionless time* $\bar{t}$*.*

For extremely slow loadings ($t_{Loading} = \{10, 100\}\, ms$ which corresponds to $\bar{t_T} < 0.007$), the thermal time is extremely small compared to the loading time ($\bar{t_T} = 0.0007 \ll 1$ for $t_{Loading} = 100\, ms$), which means that the thermal state of the transient contact quickly becomes close to the stationary contact (case A, see section 4.2). As was seen in section 4.3.2, when the loading time is high, the film thickness decreases at a relatively faster rate. This means that in the early stages of the loading process, the values of minimum film thicknesses closely follows the equivalent stationary case. As such, $h^C_{m,min}$ tends towards the value $h^A_{m,min} = 74\, nm$ for greater loading times.

For slow loadings ($t_{Loading} = \{1, 2.2, 4.6\}\, ms$ which corresponds to $\bar{t_T} = \{0.0152, 0.0318, 0.07\}$), the squeeze effect enables a higher film thickness for a longer relative time during the loading process. This means that during the initial state (small loads), the minimum film thickness is well over the value of the stationary case ($h^C_m > h^A_m$). From then, the behaviour of the contact is similar to the stationary case, similarly to what was described in the previous section. As the characteristic thermal-transient ratio increases, the relative time needed to reach the stationary state (after the loading ramp) increases.

Fast loading

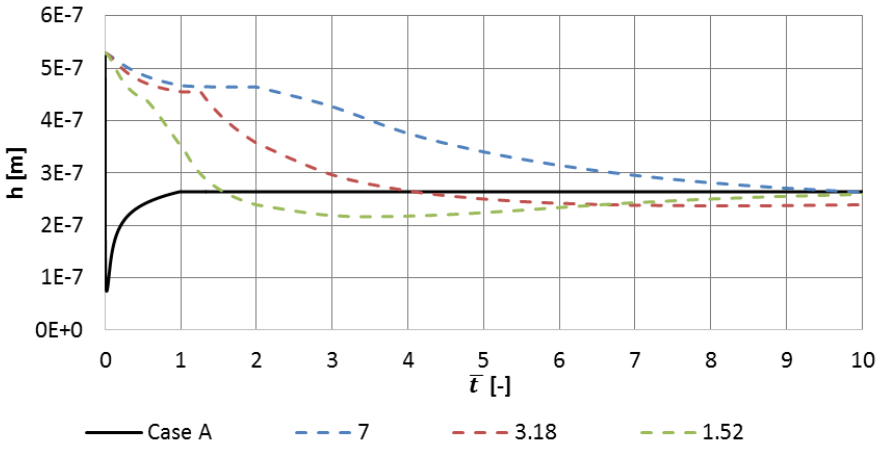

Figure 4.4-3 – Variation of the minimum film thickness in case A and case C, for $\bar{t_T} = \{1.52, 3.18, 7\}$, as a function of the dimensionless time $\bar{t}$.

For fast loadings on the other hand ($t_{Loading} = \{0.01, 0.022, 0.046\}\, ms$ which corresponds to $\bar{t_T} > 1.52$), the transient effect is so strong that the minimum film thickness in case C is greater than in case A at least until the maximum load is reached. The minimum film thickness continues to decrease even after the maximum load is reached. For $t_{Loading} = 0.046\, ms$, the characteristic thermal-transient ratio is high ($\bar{t_T} = 1.52$) and the minimum value of h_m^C is obtained when the thermal effects have established at $\bar{t} = 3.96$. The steady state is reached at $\bar{t} = 10.82$. In these extremely fast cases, $h_{m,min}^C / h_{m,min}^A > 2.5$. The discontinuities observed at the beginning of the loading process correspond to the moment the minimum film thickness becomes separate from the central film thickness.

Intermediate loading

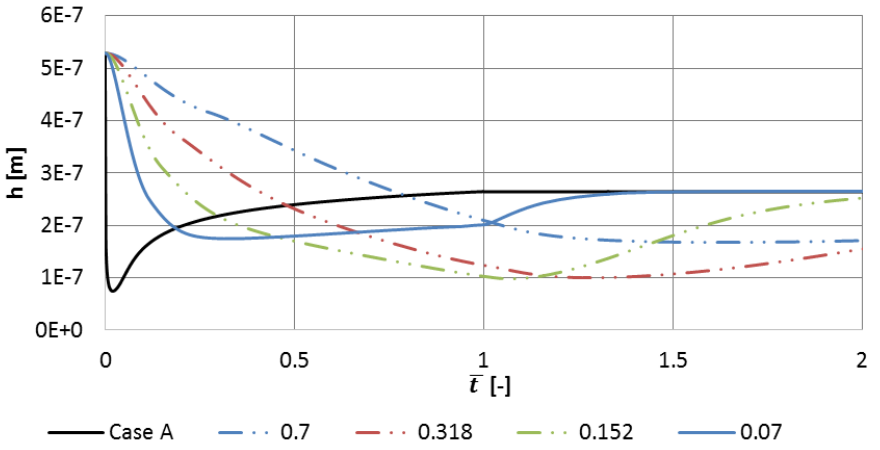

Figure 4.4-4 – Variation of the minimum film thickness in case A and case C, for $\bar{t_T} = \{0.07, 0.152, 0.318, 0.7\}$, as a function of the dimensionless time $\bar{t}$.

For intermediate loadings ($t_{Loading} = \{0.1, 0.22, 0.46\}\, ms$ which corresponds to $\bar{t_T} \in \{0.152, 0.318, 0.7\}$), the squeeze effect is still visible, but the minimum film thickness in case

C is below the one in case A before the end of the ramp. For $t_{Loading} = 0.22\ ms$ and $0.46\ ms$, $h^C_{m,min}/h^A_{m,min} \approx 1$. In that case, the thermal effects are able to separate the solids only after the loading ramp. This situation corresponds to a minimum for $h^C_{m,min}$ where neither the squeeze effect nor the thermal effect can guaranty a significantly high film thickness when the maximum load is reached ($\bar{t} = 1$).

Figure 4.4-5 shows the ratio of the minimum value of the film thickness in case C over the one in case A, for each value of the characteristic thermal-transient ratio. The three regions previously studied are easily identified.

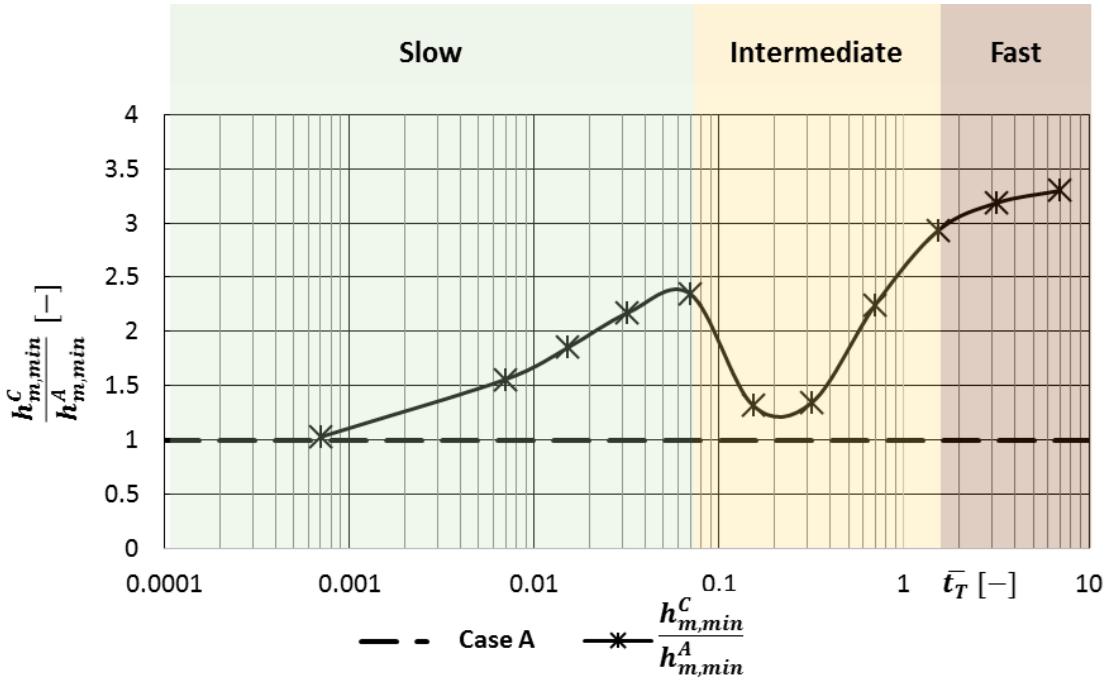

Figure 4.4-5 – Ratio of the minimum value of the minimum film thickness in case C over the value in case A, as a function of the characteristic thermal-transient ratio. The horizontal dotted line marks the value of the stationary case A.

4.5 Conclusion

In this chapter, the dynamic loading of a contact under ZEV condition is studied with the numerical model in order to identify the relative impact of the squeeze and thermal effects. In the first section, the modelling choices related to the loading process are introduced. The load is linearly varied before attaining a maximum value.

In the second part, the effect of load variations is studied in a stationary framework as a continuation of the results shown in Chapter 3. Two regimes are identified depending on the load. For lower values, the lack of elastic surface displacement is an indication of a hydrodynamic regime, mostly dominated by the variation of the rigid body separation. For high values, the contact behaves similarly to what was described in Chapter 3, in the EHL regime. The prediction formula that was provided earlier is fitted to the current problem

(different radius of contact) and shows a good ability to predict the film thickness in stationary conditions.

In the third part of this chapter, the transient isothermal contact is studied, using the literature as a reference. Overall, a decrease of the central and minimum film thicknesses is observed. For faster loadings, the squeeze effect is stronger, which leads to a higher film thickness for a relatively longer time. The semi-analytical formula developed by Wang et al.[32] is able to predict the value of the central film thickness when the maximum load is reached.

The last part of this chapter focusses on the full problem where both thermal and squeeze effects are considered.

On the one hand, a reference configuration is studied. At the beginning of the loading process, the squeeze effect is required for the film thickness to stay relatively high during the entire loading ramp as low loads imply low film thicknesses in stationary thermal conditions. As the load continues to increase, the squeeze effect vanishes while the thermal effect appears. This leads to an increase of the film thickness with the load (and time) until the maximum load is reached. From there, the steady state is reached with a delay that is associated with the final formation of the temperature field.

On the other hand, the influence of the characteristic thermal-transient ratio on the behaviour of the contact is shown. Three types of loading times are identified. For slow loadings, the thermal time is negligible before the loading time, which means that the contact closely follows the stationary reference. In this range, the faster the loading, the stronger the initial squeeze effects, which increases the minimum film thickness observed. For fast loadings, the contacts are subjected to transient effects that support high film thicknesses well after the maximum load is reached. This leaves enough time for the thermal effects to appear. As such, the minimum film thickness stays relatively high during the whole process. Finally, for contacts under intermediate loadings, the initial separation provided by the transient effect is greater than at slower loadings. The squeeze effect still fades out before the maximum load is reached. Meanwhile, it takes relatively more time for thermal effects to appear. This leads to low values of the minimum film thickness.

Conclusion and perspectives

Conclusion

This thesis focuses on highly loaded lubricated contacts in the case of zero entrainment velocity. This situation is found for example in full complement bearings (without a cage), where two successive rolling elements are in direct contact. Three phenomena other than the classical hydrodynamic lift can explain the existence of a separating film between the surfaces. First, the wall slip (also known as boundary slip) can change the effective entrainment velocity of the fluid, thus enabling a hydrodynamic lift. Wall slip is not likely to prevail when both contacting surfaces are made out of steel, which corresponds to industrial applications. Consequently, this phenomenon is not taken into account in the rest of the manuscript. Second, the thermal effect known as the viscosity wedge, stemming from the high shear heating happening in the fluid, leads to temperature and viscosity gradients across the lubricant thickness that are responsible for the generation of a load bearing capacity. Though clearly identified in the literature, the film thickness build-up was yet to be quantified. Third, the transient effect known as the squeeze effect is present when the two surfaces are suddenly pressed together. In such a configuration, a high pressure is generated at the center of the contact, which elastically displaces the surfaces, provoking a fluid entrapment. This phenomenon is time-dependant, and can only provide a temporary film thickness. The viscosity wedge and the squeeze effect are studied as an attempt to explain and quantify the film thickness build-up in the context of wide ZEV EHL contacts.

In Chapter 2, the numerical and experimental tools employed in the thesis are presented. The finite element model enables the simultaneous calculation of fluid pressure, elastic surface displacement and temperature in a time dependent environment. An experimental validation of the model is conducted on the barrel on disc tribometer Jerotrib, equipped with a sapphire disc to enable optical film thickness measurements. The hypotheses regarding the choice of material and the simplifications of the model are discussed. First, sapphire on steel contacts represent steel on steel contacts due to the thermal similarity between sapphire and steel. Second, numerical simulations of cylinder-on-plane ZEV contacts lead to very close minimum film thickness predictions with respect to experimental wide point contacts.

In Chapter 3, the viscosity wedge phenomenon is investigated in stationary thermoelastohydrodynamic contacts under ZEV condition. The dual experimental/numerical approach is able to provide a detailed understanding of the influence of the velocity, load and external temperature on the minimum film thickness. An increase of the velocity leads to an increase of the minimum film thickness up to a limit value. An increase of the load also leads to an increase of the minimum film thickness in the EHL regime. Finally, an increase of the external temperature leads to a drastic decrease of the minimum film thickness. A first

tentative film thickness prediction formula is proposed on a range of loads and velocities, for a given geometry, set of materials and external temperature. It shows a very good qualitative and quantitative agreement with all calculated and measured values.

The respective influences of the viscosity wedge and squeeze effects are compared in Chapter 4, in which the load is linearly varied from a low to a high value. The influence of the load on the film thickness is first studied in stationary thermal conditions. For extremely low loads, a hydrodynamic regime causes a strong decrease of the minimum film thickness with the load. The transition to the elastohydrodynamic regime (already studied in Chapter 3) is therefore marked by the minimum value of the minimum film thickness, from which the film thickness continuously increases with the load. In transient isothermal conditions, the squeeze effect shows an ability to support the film temporarily, tending towards zero film thickness overtime. When both the viscosity wedge and the squeeze effects are considered, they are able to compensate for one another. In the early stages of the loading process, the squeeze effect delays the decrease of the film thickness with the load. When the squeeze effect fades out, the thermal state of the contact allows the viscosity wedge to separate the surfaces in the EHL regime. The influence of the loading time is characterised by three different behaviours, corresponding to different values of the characteristic thermal-transient ratio. First, for high loading times (characterised by a low value of the characteristic thermal-transient ratio), the transient effect fades out quickly, so that the contact behaves similarly to the stationary one, with the thermal effect coming into play. In this case, slightly faster loading processes are beneficial as they increase the squeeze effect. Second, for low loading times (corresponding to characteristic thermal-transient ratios higher than one), the squeeze effect is beneficial for a longer time than the loading time, which gives time for the thermal effect to appear, even after the maximum load is reached. Third, for intermediate loading processes (characteristic thermal-transient ratios slightly lower than one), the squeeze effect fades out before the thermal effect can contribute to the separation of the surfaces, which leads to low minimum values of the minimum film thickness overtime.

This work provides three key results that will pave the way for future studies on contacts under ZEV condition, such as those found in full complement bearings. In a global context where improving component life expectancy is wanted, it is necessary to understand the behaviour of such applications in order to better predict them. First, the dual experimental/numerical approach completes the literature basis and confirms the ability for the viscosity wedge to support the applied load in stationary conditions. Second, this study also provides a first semi-analytical model that can be used for a given range of parameters (velocities and normal load) to predict the minimum film thickness separating the solids under stationary conditions (for given materials, geometry and external temperature). This is a first attempt to guide the design of components subjected to ZEV contacts, such as full-complement bearings. It also serves as a proper base that can initiate the research for a complete semi-analytical model. Third, the synergies between the transient (squeeze) and thermal effects are shown to be useful to ensure satisfactory film thicknesses during an impact under ZEV condition. As such, it is possible to appreciate the minimum film thickness occurring overtime by using the

prediction of the squeeze and viscosity wedge effects and by considering the characteristic thermal-transient ratio.

Recommendations for future work

The present work could be extended in two directions:

- In this thesis, the results presented are rooted in experimental contributions either provided by the literature, or specifically conducted during the project. This enables a quantitative validation of the model in stationary and transient conditions separately. A first attempt at predicting the values of the minimum film thickness under ZEV condition is developed. However, the experiments are conducted with only one mineral oil, one geometry and two couples of materials. Further experimental studies could provide the necessary data for a numerical prediction in a wider range of parameters. Furthermore, while based on the aforementioned experimental validation of the numerical model, the transient thermal study is here purely numerical. As such a transient experimental validation under ZEV condition, though technically more difficult to conduct, would complement the knowledge on ZEV contacts.
- The analysis made on the influence of both the viscosity wedge and the squeeze effects is a first attempt at describing the behaviour of contacts occurring between rolling elements in full complement bearings. The contact is studied assuming zero entrainment velocity during the entire loading process. In full complement bearings, the kinematic behaviour may induce a small entrainment velocity in the contact. In addition, the variation of the load is assumed linear, and the mass of the contacting bodies is ignored. Another way to improve the knowledge of such bearings should integrate their full dynamic description, using the results presented here as a baseline for the prediction of the roller-to-roller contact.

Bibliography

[1] Y. Wang, Q. J. Wang, C. Lin, and F. Shi, **Development of a Set of Stribeck Curves for Conformal Contacts of Rough Surfaces**, *Tribol. Trans.*, vol. 49, no. 4, pp. 526–535, Dec. 2006.

[2] H. M. Martin, **Lubrication of gear teeth**, *Engineering*, vol. 102, pp. 119–121, 1916.

[3] L. Gümbel, **Über geschmierte Arbeitsräder**, *Z. f. d. ges. Turbinenwes.*, vol. 13, p. 357, 1916.

[4] A. M. Ertel, **In Russian (Hydrodynamic Lubrication Based on New Principles)**, *Nauk SSSR Prikadnaya Math. i Mekhanika*, vol. 3, no. 2, pp. 41–52, 1939.

[5] A. N. Grubin and I. E. Vinogradova, **In Russian (Investigation of the contact of machine components)**, *Cent. Sci. Res. Inst. Technol. Mech. Eng.*, vol. 30, 1949.

[6] B. J. Hamrock and D. Dowson, **Isothermal Elastohydrodynamic Lubrication of Point Contacts - I - Theorectical Formulation**, *J. Lubr. Tech*, vol. 98, no. 2, pp. 223–228, 1976.

[7] B. J. Hamrock and D. Dowson, **Isothermal Elastohydrodynamic Lubrication of Point Contacts - III - Fully Flooded Results**, *J. Lubr. Tech*, vol. 99, no. 2, pp. 264–275, 1977.

[8] B. J. Hamrock and D. Dowson, **Isothermal Elastohydrodynamic Lubrication of Point Contacts - IV - Starvation Results**, *J. Lubr. Tech*, vol. 99, no. 1, pp. 15–23, 1977.

[9] H. Moes, **Optimum similarity analysis with applications to elastohydrodynamic lubrication**, *Wear*, vol. 159, no. 1, pp. 57–66, 1992.

[10] R. J. Chittenden, D. Dowson, J. F. Dunn, and C. M. Taylor, **A Theoretical Analysis of the Isothermal Elastohydrodynamic Lubrication of Concentrated Contacts. I. Direction of Lubricant Entrainment Coincident with the Major Axis of the Hertzian Contact Ellipse**, *Proc. R. Soc. A Math. Phys. Eng. Sci.*, vol. 397, no. 1813, pp. 245–269, 1985.

[11] H. P. Evans, **The Isothermal Elastohydrodynamic Lubrication of Spheres**, *J. Tribol.*, vol. 103, no. 4, p. 547, Oct. 1980.

[12] C.H.Venner, **Multilevel solution of the EHL line and point contact problems**, p. 340, 1991.

[13] W. R. J. Jones, B. A. Shogrin, and E. P. Kingsbury, **Long term performance of a retainerless bearing cartridge with an oozing flow lubricator for spacecraft applications**, *NASA TM-107492*. 1997.

[14] B. A. Shogrin, W. R. Jones, E. P. P. Kingsbury, M. J. Jansen, and J. M. Prahl, **Experimental Study of Load Carrying Capacity of Point Contacts at Zero Entrainment Velocity**, *NASA TM-208650*. 1998.

[15] B. A. Shogrin, W. R. Jones, E. P. Kingsbury, and J. M. Prahl, **Experimental determination of load carrying capacity of point contacts at zero entrainment velocity**, *NASA TM-208848*. 1999.

[16] P. Thompson, **The effect of sliding speed on film thickness and pressure supporting ability of a point contact under zero entrainment velocity conditions**, *NASA TM-210566*, 2000.

[17] A. Cameron, **The Viscosity Wedge**, *A S L E Trans.*, vol. 1, no. 2, pp. 248–253, Jan. 1958.

[18] D. F. Moore, **A review of squeeze films**, *Wear*, vol. 8, no. 4, pp. 245–263, Jul. 1965.

[19] C. Neto, D. R. Evans, E. Bonaccurso, H. J. Butt, and V. S. J. Craig, **Boundary slip in Newtonian liquids: A review of experimental studies**, *Reports Prog. Phys.*, vol. 68, no. 12, pp. 2859–2897, 2005.

[20] J. Raisin, N. Fillot, D. Dureisseix, P. Vergne, and V. Lacour, **Characteristic times in transient thermal elastohydrodynamic line contacts**, *Tribol. Int.*, vol. 82, no. PB, pp. 472–483, Feb. 2015.

[21] J.-D. Wheeler, N. Fillot, P. Vergne, D. Philippon, and G. Morales Espejel, **On the crucial role of ellipticity on elastohydrodynamic film thickness and friction**, *Proc. Inst. Mech. Eng. Part J J. Eng. Tribol.*, vol. 230, no. 12, pp. 1503–1515, Dec. 2016.

[22] F. D. Murnaghan, **The Compressibility of Media under Extreme Pressures**, *Proc. Natl. Acad. Sci.*, vol. 30, no. 9, pp. 244–247, Sep. 1944.

[23] S. Bair, C. Mary, N. Bouscharain, and P. Vergne, **An improved Yasutomi correlation for viscosity at high pressure**, *Proc. Inst. Mech. Eng. Part J J. Eng. Tribol.*, vol. 227, no. 9, pp. 1056–1060, Sep. 2013.

[24] S. Bair, **A Rough Shear-Thinning Correction for EHD Film Thickness**, *Tribol. Trans.*, vol. 47, no. 3, pp. 361–365, Jul. 2004.

[25] J. Molimard, M. Querry, and P. Vergne, **New tools for the experimental study of EHD and limit lubrications**, *Proc. 25th Leeds-Lyon Symp. Tribol.*, vol. 36, pp. 717–726, 1999.

[26] J.-D. Wheeler, J. Molimard, N. Devaux, D. Philippon, N. Fillot, P. Vergne, and G. E. Morales-Espejel, **A Generalized Differential Colorimetric Interferometry Method: Extension to the Film Thickness Measurement of Any Point Contact Geometry**, *Tribol. Trans.*, vol. 61, no. 4, pp. 648–660, Jul. 2018.

[27] S.-N. Ndiaye, L. Martinie, D. Philippon, N. Devaux, and P. Vergne, **A Quantitative Friction-Based Approach of the Limiting Shear Stress Pressure and Temperature Dependence**, *Tribol. Lett.*, vol. 65, no. 4, p. 149, Dec. 2017.

[28] T. Doki-Thonon, N. Fillot, P. Vergne, and G. E. Morales Espejel, **Numerical insight into heat transfer and power losses in spinning EHD non-Newtonian point contacts**, *Proc. Inst. Mech. Eng. Part J J. Eng. Tribol.*, vol. 226, no. 1, pp. 23–35, 2012.

[29] J. Molimard, **Etude expérimentale du régime de lubrification en film mince :**

application aux fluides de laminage, PhD thesis, INSA de Lyon, 1999.

[30] G. Nijenbanning, C. H. Venner, and H. Moes, **Film thickness in elastohydrodynamically lubricated elliptic contacts**, *Wear*, vol. 176, no. 2, pp. 217–229, Aug. 1994.

[31] D. Dowson and D. Wang, **Impact elastohydrodynamics**, *Tribol. Ser.*, vol. 30, pp. 565–582, 1995.

[32] J. Wang, C. H. Venner, and A. A. Lubrecht, **Central film thickness prediction for line contacts under pure impact**, *Tribol. Int.*, vol. 66, pp. 203–207, 2013.

[33] S. Bair, **Correlations for the Temperature and Pressure and Composition Dependence of Low-Shear Viscosity**, in *High Pressure Rheology for Quantitative Elastohydrodynamics*, Elsevier, 2019, pp. 135–182.

[34] J. Pohl, K.-E. Rydberg, and P. Krus, **Thermal Aspects in Lubrication System Design for Internal Combustion Engines**, *Int. Conf. Therm. Process Model. Comput. Simul.*, no. 1, pp. 332–341, 2000.

[35] M. H. Knapp and M. Freifeld, **The use of synthetic lubricants in compressors**, *Int. Compress. Eng. Conf. Sch.*, pp. 480–482, 1972.

[36] G.-A. Hirn, **Sur les principaux phénomènes que présentent les frottements médiats**, *Bull. Soc. Ind. Mulhouse*, vol. 26, p. 238, 1854.

[37] R. Palazzetti and X.-T. Yan, **Study on lubrication effect on motorbike chain transmissions**, *Ind. Lubr. Tribol.*, vol. 68, no. 5, pp. 561–568, Aug. 2016.

[38] P. S. Walker, D. Dowson, M. D. Longfield, and V. Wright, **Lubrication of human joints.**, *Ann. Rheum. Dis.*, vol. 28, no. 2, pp. 194–194, Mar. 1969.

[39] T. Røn, N. J. Patil, F. Ajalloueian, S. Rishikesan, B. Zappone, I. S. Chronakis, and S. Lee, **Gastric mucus and mucuslike hydrogels: Thin film lubricating properties at soft interfaces**, *Biointerphases*, vol. 12, no. 5, pp. 051001-1-051001–10, Dec. 2017.

[40] A. D. Dimarogonas, *History of Technology I, II*. Athens: Macedonians Publications, 2001.

[41] T. Mang and W. Dresel, *Lubricants and Lubrication*. Wiley, 2006.

[42] R. Stribeck, *Die wesentlichen Eigenschaften der Gleit- und Rollenlager*. Julius Springer, 1903.

[43] N. P. Petrov, **Friction in Machines and the Effect of the Lubricant**, *Inzh. Zh., St-Peterb.*, no. 1, pp. 71–140, 1883.

[44] B. Tower, **First Report on Friction Experiments**, *Proc. Inst. Mech. Eng.*, vol. 34, no. 1, pp. 632–659, Jun. 1883.

[45] O. Reynolds, **IV. On the theory of lubrication and its application to Mr. Beauchamp tower's experiments, including an experimental determination of the viscosity of olive oil**, *Philos. Trans. R. Soc. London*, vol. 177, pp. 157–234, Jan. 1886.

[46] C. Barus, **Isothermal, Isopiestics and Isometrics relative to viscosity**, *Am. J. Sci.*, vol. 45, pp. 87–96, 1896.

[47] H. Hertz, **Ueber die Berührung fester elastischer Körper**, *J. für die reine und Angew. Math. (Crelle's Journal)*, vol. 1882, no. 92, pp. 156–171, 1882.

[48] B. J. Hamrock and D. Brewe, **Simplified Solution for Stresses and Deformations.**, *Am. Soc. Mech. Eng.*, vol. 105, no. 81, pp. 171–177, 1981.

[49] T. Doki-Thonon, N. Fillot, G. E. Morales Espejel, M. Querry, D. Philippon, N. Devaux, and P. Vergne, **A Dual Experimental/Numerical Approach for Film Thickness Analysis in TEHL Spinning Skewing Circular Contacts**, *Tribol. Lett.*, vol. 50, no. 1, pp. 115–126, Apr. 2013.

[50] K. Sathyan, K. Gopinath, S. H. Lee, and H. Y. Hsu, **Bearing Retainer Designs and Retainer Instability Failures in Spacecraft Moving Mechanical Systems**, *Tribol. Trans.*, vol. 55, no. 4, pp. 503–511, Jul. 2012.

[51] V. Bruyere, N. Fillot, G. E. Morales-Espejel, and P. Vergne, **Computational fluid dynamics and full elasticity model for sliding line thermal elastohydro dynamic contacts**, *Tribol. Int.*, vol. 46, no. 1, pp. 3–13, 2012.

[52] M. Jannesar, G. R. Jafari, S. Vasheghani Farahani, and S. Moradi, **Thin film thickness measurement by the conductivity theory in the framework of Born approximation**, *Thin Solid Films*, vol. 562, pp. 372–376, Jul. 2014.

[53] N. Marx, J. Guegan, and H. A. Spikes, **Elastohydrodynamic film thickness of soft EHL contacts using optical interferometry**, *Tribol. Int.*, vol. 99, pp. 267–277, Jul. 2016.

[54] M. T. Kirk, **Hydrodynamic Lubrication of "Perspex,"** *Nature*, vol. 194, no. 4832, pp. 965–966, Jun. 1962.

[55] J. Mayer, **Einfluss der Oberfläche und des Schmierstoffs auf das Reibungsverhalten im EHD-Kontakt**, PhD thesis, TU München, 2013.

[56] J. P. O'Donoghue and A. Cameron, **Friction and temperature in rolling sliding contacts**, *ASLE Trans.*, vol. 9, no. 2, pp. 186–194, 1966.

[57] K. Yagi, P. Vergne, and T. Nakahara, **In situ pressure measurements in dimpled elastohydrodynamic sliding contacts by Raman microspectroscopy**, *Tribol. Int.*, vol. 42, no. 5, pp. 724–730, May 2009.

[58] M. Ebner, A. Ziegltrum, T. Lohner, K. Michaelis, and K. Stahl, **Measurement of EHL temperature by thin film sensors – Thermal insulation effects**, *Tribol. Int.*, pp. 1–9, 2018.

[59] S. M. B. Albahrani *et al.*, **Quantum dots to probe temperature and pressure in highly confined liquids**, *RSC Adv.*, vol. 8, no. 41, pp. 22897–22908, 2018.

[60] L. G. Houpert and B. J. Hamrock, **Fast Approach for Calculating Film Thicknesses and Pressures in Elastohydrodynamically Lubricated Contacts at High Loads**, *J. Tribol.*, vol.

108, no. 3, p. 411, 1986.

[61] C. Roelands, **Correlational Aspects of the Viscosity-Temperature Pressure Relationship of Lubricating Oils**, PhD thesis, Technische Hogeschool Draft, 1966.

[62] V. Bruyere, **Une modélisation multi-physique et multi-phasique du contact lubrifié**, 2013.

[63] **Fourth Report of the Research Committee on Friction**, *Proc. Inst. Mech. Eng.*, vol. 42, no. 1, pp. 111–140, Jun. 1891.

[64] K. L. Johnson, **Non-Newtonian Effects in Elastohydrodynamic Lubrication**, in *Tribology Series*, vol. 25, no. C, 1993, pp. 15–26.

[65] J. Raisin, N. Fillot, P. Vergne, D. Dureisseix, and V. Lacour, **Transient Thermal Elastohydrodynamic Modeling of Cam–Follower Systems: Understanding Performance**, *Tribol. Trans.*, vol. 59, no. 4, pp. 720–732, Jul. 2016.

[66] K. Yagi, K. Kyogoku, and T. Nakahara, **Temperature measurements of oil film and surface in point contact EHL under high slip ratio condition**, *Toraibarojisuto/Journal Japanese Soc. Tribol.*, vol. 46, no. 9, pp. 725–732, 2001.

[67] K. Yagi, K. Kyogoku, and T. Nakahara, **Relationship Between Temperature Distribution in EHL Film and Dimple Formation**, *J. Tribol.*, vol. 127, no. 3, p. 658, 2005.

[68] F. Guo, P. Yang, and P. L. Wong, **On the thermal elastohydrodynamic lubrication in opposite sliding circular contacts**, *Tribol. Int.*, vol. 34, no. 7, pp. 443–452, 2001.

[69] F. Guo, P. Yang, and S. Qu, **On the Theory of Thermal Elastohydrodynamic Lubrication at High Slide-Roll Ratios—Circular Glass-Steel Contact Solution at Opposite Sliding**, *J. Tribol.*, vol. 123, no. 4, p. 816, 2001.

[70] F. Guo, P. L. Wong, P. Yang, and K. Yagi, **Film Formation in EHL Point Contacts under Zero Entraining Velocity Conditions**, *Tribol. Trans.*, vol. 45, no. 4, pp. 521–530, 2002.

[71] P. Yang, S. Qu, Q. Chang, and F. Guo, **On the Theory of Thermal Elastohydrodynamic Lubrication at High Slide-Roll Ratios—Line Contact Solution**, *J. Tribol.*, vol. 123, no. 1, p. 36, 2001.

[72] B. Zhang, J. Wang, M. Omasta, and M. Kaneta, **Effect of fluid rheology on the thermal EHL under ZEV in line contact**, *Tribol. Int.*, vol. 87, pp. 40–49, Jul. 2015.

[73] B. Zhang and J. Wang, **Enhancement of thermal effect in zero entrainment velocity contact under low surface velocity**, *Proc. Inst. Mech. Eng. Part J J. Eng. Tribol.*, vol. 230, no. 12, pp. 1554–1561, Dec. 2016.

[74] B. Zhang, J. Wang, M. Omasta, and M. Kaneta, **Variation of surface dimple in point contact thermal EHL under ZEV condition**, *Tribol. Int.*, vol. 94, pp. 383–394, 2016.

[75] A. Dyson and A. R. Wilson, **Film Thicknesses in Elastohydrodynamic Lubrication at High Slide/Roll Ratios**, *Proc. Inst. Mech. Eng. Conf. Proc.*, vol. 183, no. 16, pp. 81–97, Sep.

1968.

[76] H. S. Cheng, **A Refined Solution to the Thermal-Elastohydrodynamic Lubrication of Rolling and Sliding Cylinders**, *A S L E Trans.*, vol. 8, no. 4, pp. 397–410, Jan. 1965.

[77] Y. P. Chiu and L. B. Sibley, **Contact shape and non-Newtonian effects in elastohydrodynamic point contacts**, *ASLE Lubr. Eng.*, vol. 28, pp. 48–60, 1972.

[78] A. Cameron, **Hydrodynamic Lubrication of Rotating Disks in Pure Sliding. A new Type of Oil Film Formation**, *J. Inst. Pet.*, vol. 37, no. 11, pp. 471–486, 1951.

[79] J. Stefan, **Versuche über die scheinbare Adhäsion**, *Ann. der Phys. und Chemie*, vol. 230, no. 2, pp. 316–318, 1875.

[80] W. Hardy and I. Bircumshaw, **Bakerian Lecture. Boundary Lubrication. Plane Surfaces and the Limitations of Amontons' Law**, *Proc. R. Soc. A Math. Phys. Eng. Sci.*, vol. 108, no. 745, pp. 1–27, May 1925.

[81] F. P. Bowden and D. Tabor, **The Friction and Lubrication of Solids**, Oxford University Press, 1954, p. Chapters 13 and 15.

[82] H. Christensen, **The oil film in a closing gap**, *Proc. R. Soc. London. Ser. A. Math. Phys. Sci.*, vol. 266, no. 1326, pp. 312–328, Mar. 1962.

[83] K. Herrebrugh, **Elastohydrodynamic Squeeze Films Between Two Cylinders in Normal Approach**, *J. Lubr. Technol.*, vol. 92, no. 2, p. 292, 1970.

[84] H. D. Conway, **The Rate of Change of Film Thickness in the Elastohydrodynamic Squeeze Film Process**, *J. Lubr. Technol.*, vol. 95, no. 3, p. 391, 1973.

[85] M. M. . Safa and R. Gohar, **Squeeze films in elastohydrodynamic lubrication**, *Proc. 12th Leeds-Lyon Symp. Tribol.*, vol. 10, pp. 227–233, 1985.

[86] P. Yang and S. Wen, **Pure squeeze action in an isothermal elastohydrodynamically lubricated spherical conjunction part 1. Theory and dynamic load results**, *Wear*, vol. 142, no. 1, pp. 1–16, Feb. 1991.

[87] P. Yang and S. Wen, **Pure squeeze action in an isothermal elastohydrodynamically lubricated spherical conjunction part 2. Constant speed and constant load results**, *Wear*, vol. 142, no. 1, pp. 17–30, Feb. 1991.

[88] D. Dowson and D. A. Jones, **Lubricant Entrapment between Approaching Elastic Solids**, *Nature*, vol. 214, no. 5091, pp. 947–948, May 1967.

[89] H. Nishikawa, K. Handa, K. Teshima, K. Matsuda, and M. Kaneta, **Behavior of EHL Films in Cyclic Squeeze Motion**, *JSME*, vol. 38, no. 3, pp. 577–585, 1995.

[90] F. J. Westlake and A. Cameron, **Report 12: A Study of Ultra-Thin Lubricant Films Using an Optical Technique**, *Proc. Inst. Mech. Eng. Conf. Proc.*, vol. 182, no. 7, pp. 75–78, Sep. 1967.

[91] H. D. Conway and H. C. Lee, **Impact of a Lubricated Surface by a Sphere**, *J. Lubr.*

Technol., vol. 97, no. 4, p. 613, 1975.

[92] D. Dowson and D. Wang, **An analysis of the normal bouncing of a solid elastic ball on an oily plate**, *Wear*, vol. 179, no. 1–2, pp. 29–37, 1994.

[93] F. Guo, H. Nishikawa, P. Yang, and M. Kaneta, **EHL under cyclic squeeze motion**, *Tribol. Int.*, vol. 40, no. 1, pp. 1–9, Jan. 2007.

[94] C. H. Venner, J. Wang, and A. A. Lubrecht, **Central film thickness in EHL point contacts under pure impact revisited**, *Tribol. Int.*, vol. 100, pp. 1–6, Aug. 2016.

[95] D. F. Hays, **Squeeze Films for Rectangular Plates**, *J. Basic Eng.*, vol. 85, no. 2, p. 243, 1963.

[96] D. F. Moore, **On the inclined non-inertial sinkage of a flat plate**, *J. Fluid Mech.*, vol. 20, no. 2, pp. 321–330, Oct. 1964.

[97] J. P. Vichard, **Transient Effects in the Lubrication of Hertzian Contacts**, *J. Mech. Eng. Sci.*, vol. 13, no. 3, pp. 173–189, Jun. 1971.

[98] L. Bobach, R. Beilicke, D. Bartel, and L. Deters, **Thermal elastohydrodynamic simulation of involute spur gears incorporating mixed friction**, *Tribol. Int.*, vol. 48, pp. 191–206, Apr. 2012.

[99] J. Wang and P. Yang, **A Numerical Analysis for TEHL of Eccentric-Tappet Pair Subjected to Transient Load**, *J. Tribol.*, vol. 125, no. 4, p. 770, 2003.

[100] J. Wang, N. Wang, P. Yang, M. Kaneta, and A. A. Lubrecht, **A theoretical simulation of thermal elastohydrodynamic lubrication for a Newtonian fluid in impact motion**, *Tribol. Int.*, vol. 67, pp. 116–123, Nov. 2013.

[101] J. Zhang, Q. Ni, J. Wang, and F. Guo, **Transient thermal elastohydrodynamic lubrication of point contacts subjected to normal vibration**, *Ind. Lubr. Tribol.*, vol. 68, no. 5, pp. 536–547, Aug. 2016.

[102] F. Guo, P. L. Wong, M. Geng, and M. Kaneta, **Occurrence of wall slip in elastohydrodynamic lubrication contacts**, *Tribol. Lett.*, vol. 34, no. 2, pp. 103–111, 2009.

[103] P. L. Wong, X. M. Li, and F. Guo, **Evidence of lubricant slip on steel surface in EHL contact**, *Tribol. Int.*, vol. 61, pp. 116–119, May 2013.

[104] X. M. Li, F. Guo, and P. L. Wong, **Shear rate and pressure effects on boundary slippage in highly stressed contacts**, *Tribol. Int.*, vol. 59, pp. 147–153, 2013.

[105] Y. Zhao, P. L. Wong, and J. H. Mao, **EHL film formation under zero entrainment velocity condition**, *Tribol. Int.*, vol. 124, no. August 2018, pp. 1–9, Aug. 2018.

[106] P. L. Wong, Y. Zhao, and J. Mao, **Facilitating effective hydrodynamic lubrication for zero-entrainment-velocity contacts based on boundary slip mechanism**, *Tribol. Int.*, vol. 128, pp. 89–95, 2018.

[107] W. Habchi, **A Full-System Finite Element Approach to Elastohydrodynamic Lubrication Problems : Application to Ultra-Low-Viscosity Fluids**, PhD thesis, Institut National des Sciences Appliquées de Lyon, 2008.

[108] D. Dowson, **A generalized Reynolds equation for fluid-film lubrication**, *Int. J. Mech. Sci.*, vol. 4, no. 2, pp. 159–170, Mar. 1962.

[109] S. R. Wu, **A penalty formulation and numerical approximation of the Reynolds-Hertz problem of elastohydrodynamic lubrication**, *Int. J. Eng. Sci.*, vol. 24, no. 6, pp. 1001–1013, Jan. 1986.

[110] T. J. R. Hughes, L. P. Franca, and G. M. Hulbert, **A new finite element formulation for computational fluid dynamics: VIII. The galerkin/least-squares method for advective-diffusive equations**, *Comput. Methods Appl. Mech. Eng.*, vol. 73, no. 2, pp. 173–189, May 1989.

[111] O. C. Zienkiewicz and F. Emeritus, *The Finite Element Method for Fluid Dynamics*, vol. 3. Butterworth & Heinmann, 2000.

[112] T. Reddyhoff, A. Schmidt, and H. Spikes, **Thermal Conductivity and Flash Temperature**, *Tribol. Lett.*, vol. 67, no. 1, p. 22, Mar. 2019.

[113] J. Raisin, N. Fillot, P. Vergne, and D. Dureisseix, **Numerical simulation of lubricated DLC-coated point contacts under infinite sliding conditions**, *Tribol. Int.*, vol. 133, pp. 136–151, May 2019.

[114] J. Liu, Y. Chen, Z. He, and S. Yang, **A fast compound direct iterative algorithm for solving transient line contact elastohydrodynamic lubrication problems**, *Front. Mech. Eng.*, vol. 9, no. 2, pp. 156–167, 2014.

[115] D. (Duncan) Dowson and G. R. Higginson, **Elasto-hydrodynamic lubrication : the fundamentals of roller and gear lubrication**. Pergamon Press, Oxford; New York, 1966.

[116] B. Meziane, P. Vergne, N. Devaux, L. Lafarge, G. E. Morales-Espejel, and N. Fillot, **Film thickness build-up in zero entrainment velocity wide point contacts**, *Tribol. Int.*, vol. 141, p. 105897, Jan. 2020.

[117] M. Kaneta, H. Nishikawa, M. Mizui, and F. Guo, **Impact Elastohydrodynamics in Point Contacts**, *Proc. Inst. Mech. Eng. Part J J. Eng. Tribol.*, vol. 225, no. 1, pp. 1–12, Jan. 2011.

[118] M. Kaneta, J. Wang, F. Guo, I. Krupka, and M. Hartl, **Effects of loading process and contact shape on point impact elastohydrodynamics**, *Tribol. Trans.*, vol. 55, no. 6, pp. 772–781, 2012.

[119] R. Larsson and E. Höglund, **Elastohydrodynamic lubrication at pure squeeze motion**, *Wear*, vol. 179, no. 1–2, pp. 39–43, Dec. 1994.

[120] H. A. Lorentz, **Ueber die Beziehung zwischen der Fortpflanzungsgeschwindigkeit des Lichtes und der Körperdichte**, *Ann. der Phys. und Chemie*, vol. 245, no. 4, pp. 641–665, 1880.

[121] L. Lorenz, **Ueber die Refractionsconstante**, *Ann. der Phys. und Chemie*, vol. 247, no. 9, pp. 70–103, 1880.

[122] C. Saubade, **Indice de réfraction de l'eau pure aux basses températures, pour la longueur d'onde de 5 893 Å**, *J. Phys.*, vol. 42, no. 2, pp. 359–366, 1981.

Appendix A. Stationary ZEV contact with a glass disc

In most of this manuscript, steel/steel and steel/sapphire contacts are studied. For the former, the antisymmetry of the contact is ensured. For the latter, the thermal similarity of steel with sapphire limits the asymmetries (see Chapter 2, section 2.3.4). In both cases, a dimpled film thickness profile is observed in the EHL regime. The case of glass on steel contact is investigated in this Appendix. The material properties of glass are reported in Table A-1.

Experiments were conducted with a glass disc, for a velocity $\mathrm{u} = 5\ \mathrm{m/s}$, a load of $\mathrm{w^{2D}} = 50\ \mathrm{N}$ and an external temperature $\mathrm{T_0} = 293.15\ \mathrm{K}$. An interferogram for the steel/glass contact is shown in Figure A-1 alongside the interferogram for the steel/sapphire contact; which corresponds to the analysis made in Chapter 2, section 2.3.4. The film thickness along the x-axis is plotted in Figure A-2.

	Glass
$E\ [Pa]$	72×10^9
υ	0.23
$\rho\ [kg.m^{-3}]$	2530
$C_p\ [J.kg^{-1}.K^{-1}]$	880
$k\ [W.m^{-1}.K^{-1}]$	0.937

Table A-1 – Material properties of glass([26]*).*

The film thickness distribution of the steel/glass (Figure A-1 and Figure A-2) is extremely different from the steel/sapphire one (see Figure 2.3-4). Indeed, the film thickness with a glass disc is extremely asymmetrical. As such, the description of the film thickness profile made in Chapter 2 does not apply to a glass disc. Indeed, with a glass disc, only a small dimple is present on the left side. This means that only one local minimum film thickness is observed. The value of this minimum film thickness is also a lot smaller than with the sapphire disc (Experimentally, $h_m = 43\ nm$).

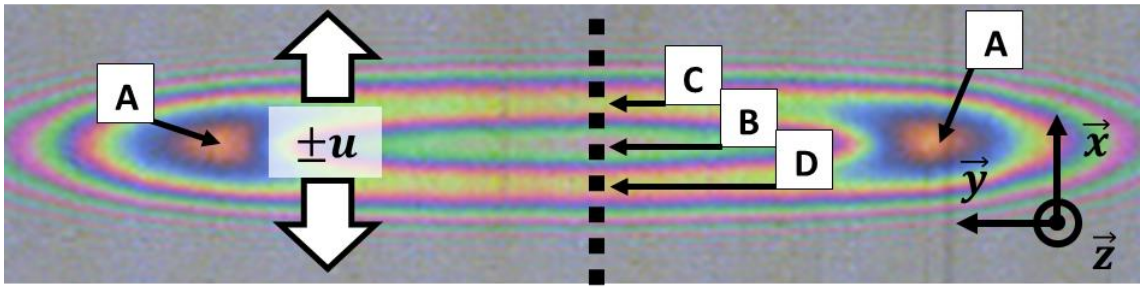

(a)

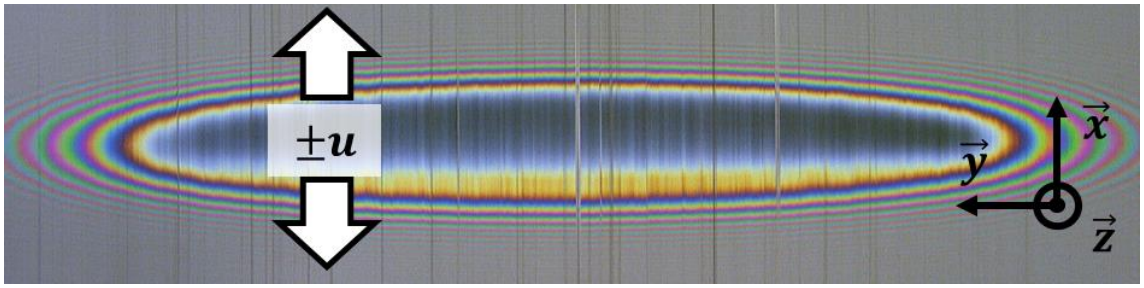

(b)

Figure A-1 – (a) Interferogram obtained with a sapphire disc (Magnification $\times 10$). (b) Interferogram obtained with a glass disc (Magnification $\times 5$). Both interferograms were captured on for a velocity $u = 5\ m/s$, a load of $w^{2D} = 50\ N$ and an external temperature $T_0 = 293.15\ K$.

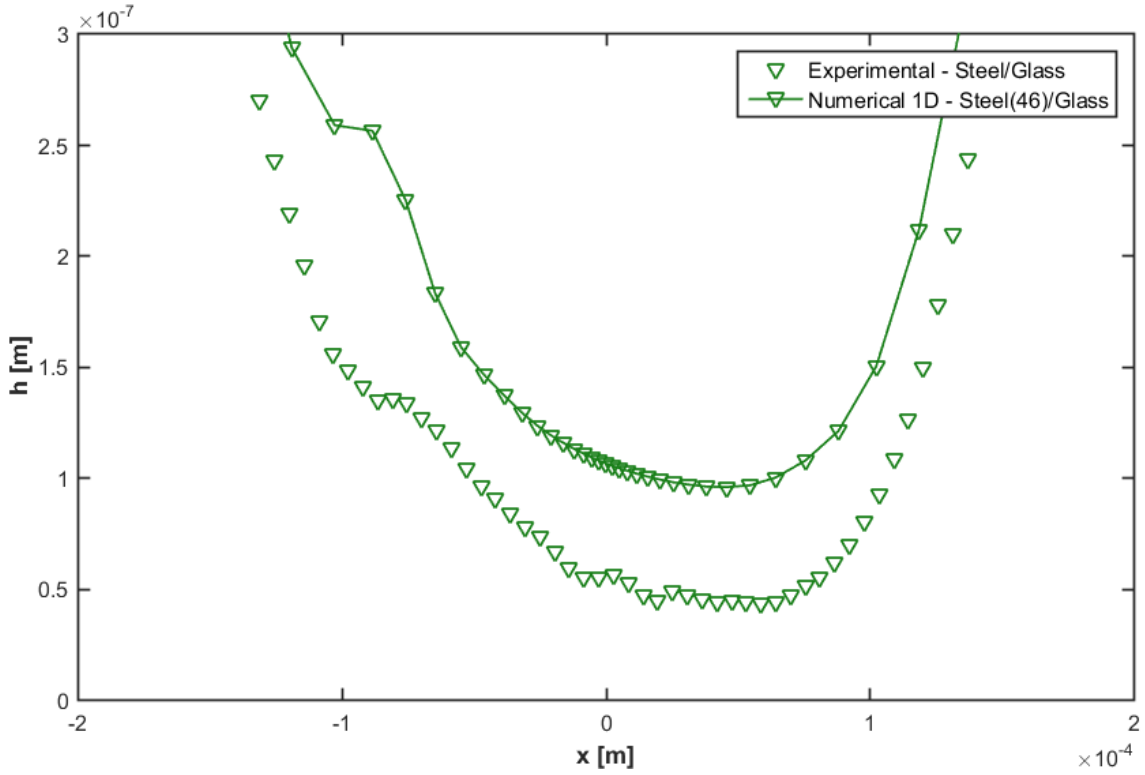

Figure A-2 – Film thickness between a glass disc and a steel barrel, measured in the experiments and calculated with the 1D model, for a velocity $u = 5\ m/s$, a load of $w^{1D} = 4.6 \times 10^4\ N.m^{-1}$ and an external temperature $T_0 = 293.15\ K$.

The heat evacuated through the glass surface is $2168.2\ W.m^{-1}$ while it is $11760\ W.m^{-1}$ through the steel surface. This means that the thermal dissimilarity between steel and glass is high. In Figure A-3, the temperature distribution in the steel/glass contact is very asymmetrical. The temperature in the steel surface goes up to $350\ K$ while the glass surface

only goes up to $325\ K$. In Figure A-4, the corresponding temperature differences between the two surfaces is plotted alongside the pressure profile. Both profiles exhibit the same asymmetries. The pressure profile presents a bump at $x = -0.9\ mm$, which is associated with a small and eccentric dimple in the film thickness profile.

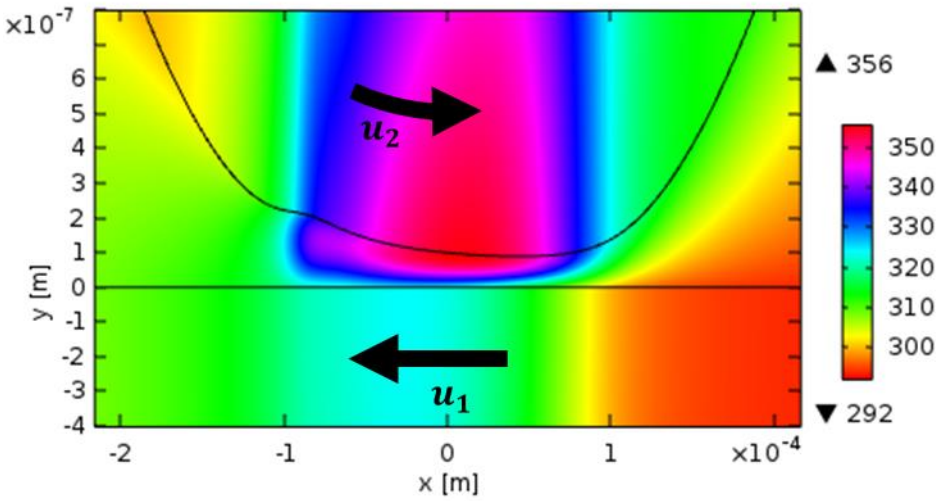

Figure A-3 – Temperature variation in the fluid and solids with ($u = 5\ m/s$, $w^{1D} = 4.36 \times 10^4\ N.m^{-1}$ and $T_0 = 293.15\ K$). The equivalent body displacement is assigned to the top solid (steel). The bottom solid (glass) is considered rigid.

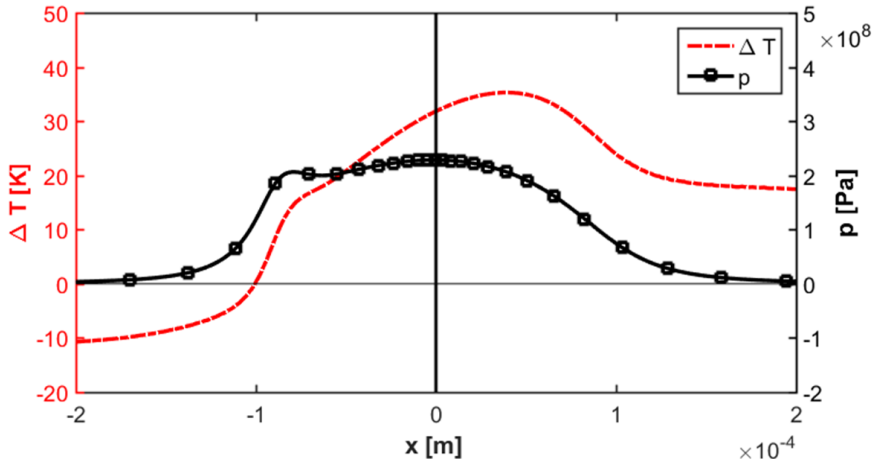

Figure A-4 – Pressure profile and numerical temperature differences between the barrel/fluid interface and the fluid/disc interface ($u = 5\ m/s$, $w^{1D} = 4.36 \times 10^4\ N.m^{-1}$ and $T_0 = 293.15\ K$), for a steel on glass contact.

These results are reminiscent of the ones shown by Raisin et al.[113]. They studied ZEV point contacts where the solids in the contact were either steel or steel coated with Diamond-Like Carbon (DLC). Three duets were therefore studied: steel/steel, DLC coated steel/steel and DLC coated steel/DLC coated steel. They noted that when one or both surfaces are DLC coated, the film thickness profiles were significantly lower than when the contact were steel/steel, the worst case being the asymmetrical steel/DLC coated steel.

To conclude, the presence of two thermally dissimilar surfaces (such as steel/glass or steel/DLC coated steel) in contacts under ZEV condition leads to asymmetrical temperature differences. The corresponding pressure profile is therefore stronger on one side of the contact, which leads to a small eccentric dimple. On the other side, the minimum film thickness becomes very small due to the low pressure.

Appendix B. Refraction index of the lubricant

For the experimental results presented in Chapter 2 and Chapter 3, the refraction index is approximated assuming that the pressure distribution follows a Hertz profile and that the external temperature is uniform in the contact. The refraction index normally varies with the pressure and temperature. A more precise correction can therefore be applied to the results obtained. Because the information on pressure and temperature is taken from the model and because the model is validated with the experiments, this new correction is only proposed as a proof of concept.

For each contact in the experiments, a set of static calibration curves is obtained. The resulting bijection between the colour map and the film thickness is based on the interference fringes outside the static contact area. The fluid in those locations is therefore under reference pressure and external temperature, which means that the refraction index is at a constant value $n_{ref}(p_{ref}, T_{ref})$. In the dynamic measurements, the refraction index varies in the contact area, with p and T. At each location of the contact along the x-axis, an average value of the refraction index can be calculated, as in eq. B-1:

$$\overline{n_{exp}(x)} = \frac{1}{h(x)} \int_0^h n_{exp}(x,z)\, dz \qquad \textit{eq. B-1}$$

where $n_{exp}(x,z) = n_{exp}(p(x,z), T(x,z))$ is the local value of the refraction index. The corrected value of film thickness is then calculated from the measured values as in eq. B-2:

$$h_{corrected}(x) = h_{measured}(x) \times \frac{\overline{n_{exp}(x)}}{n_{ref}} \qquad \textit{eq. B-2}$$

For $T_{ref} = 293.15\ K$, it is possible to use the law of Lorentz-Lorenz([120][121]) to link $\overline{n_{exp}(x)}$ with n_{ref} and $\rho_{ref} = \rho(p_{ref}, T_{ref})$ and the local average value of the density ($\overline{\rho_{exp}(x)} = \rho_e/h$) as in eq. B-3:

$$\frac{\overline{n_{exp}(x)}^2 - 1}{\overline{n_{exp}(x)}^2 + 2} = \underbrace{\frac{\overline{\rho_{exp}(x)}}{\rho(p_{ref}, T_{ref})} \times \frac{{n_{ref}}^2 - 1}{{n_{ref}}^2 + 2}}_{\Phi} \qquad \textit{eq. B-3}$$

Φ is used to simplify the next expression.

This method, developed by Saubade[122], gives all the necessary values to calculate $\overline{n_{exp}(x)}$ as in eq. B-4:

$$\overline{n_{exp}(x)} = \left(\frac{1+2\Phi}{1-\Phi}\right)^{1/2} \qquad \textit{eq. B-4}$$

Using this correction in the validation case in Chapter 2 (steel on sapphire, $T_0 = 293.15\ K$, $u = 5\ m.s^{-1}$ and $w^{2D} = 50\ N$), the experimental minimum film thickness varies by less than 1% (due to the fact that the minimum film thickness is found in a low-pressure zone) and the corrected central film thickness is decreased by 5.6% from $h_{c,measured}(x) = 498\ nm$ to $h_{c,corrected}(x) = 470\ nm$. With this correction, the relative difference between the experimental value and the numerical value (1D variant) goes down from $28.3\ \%$ to 24.3%. The variation of the refraction index with the temperature and pressure is not enough to explain the differences of central film thickness obtained experimentally and numerically (1D variant), although it still makes the results more coherent.

Appendix C. Local quantities in a high velocity contact under ZEV condition

In section 3.2.1, it was noted that for high velocities, the 1D model gave similar values of the central and minimum film thicknesses. This was an indication that the dimple disappeared in such conditions. To understand this phenomenon, a calculation was conducted with steel surfaces (Table 2.2-1). The lubricant chosen is the Shell T9. It follows the Murnaghan[22] (eq. 2.1-9) density law, the modified WLF[23] (eq. 2.1-11) pressure/temperature viscosity correlation and the non-Newtonian formulation by Carreau-Yasuda[24] (eq. 2.1-12). The solid and fluid properties are found in Table 2.2-1 and Table 2.2-2 respectively. The external temperature is $T_0 = 293.15\ \mathrm{K}$, the equivalent contact radius $R^{1D} = 0.0128\ m$, the velocity $u = 15\ m.s^{-1}$ and the normal load per unit length $w^{1D} = 58198\ N.m^{-1}$.

Table C-1 contains the information on the relative load bearing capacity as defined by eq. 2.1-10 (with the same definition for $\Omega_{p,p}$) and eq. 3.1-5. The information contained in Table 3.1-1 is replicated for comparison. The main information is that at high velocities, an important portion of the load bearing capacity is found outside of the contact area, with $\Omega_{p,o} = 12.4\%$ in the present case which is higher than the value obtained at $2\ m.s^{-1}$ ($\Omega_{p,o} = 2.0\%$). As such, the lack of a dimple is associated with a wider and flatter pressure distribution than the one in section 3.1.

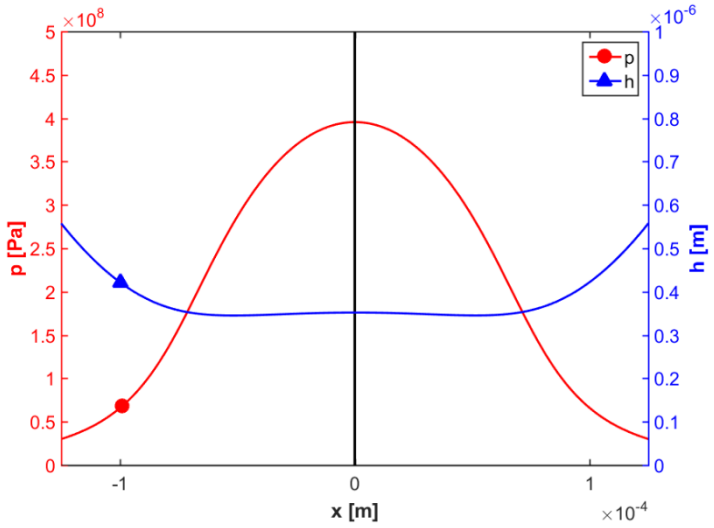

Figure C-1 – Pressure and film thickness profiles at $15\ m.s^{-1}$.

		Region		
		$\Omega_{p,o}$	$\Omega_{p,p}$	$\Omega_{p,i}$
Pressure distribution	Hertz	0%	50.4%	49.6%
	ZEV 2 $m.s^{-1}$	2.0%	22.1%	75.9%
	ZEV 13 $m.s^{-1}$	12.4%	40.6%	47.0%

Table C-1 – Relative contribution to the load bearing capacity $\bar{c}|_{\Omega}$ for the pressure distribution as defined by Hertz[47] and the one calculated under ZEV condition for two different velocities.

Heat is mainly generated along the horizontal central line of the contact, as seen in Figure C-3(a) and (b). With a maximum shear heat source of $1.18 \times 10^{15}\ W.m^{-3}$ and a total heat dissipation of $32290\ W.m^{-1}$, the amount of total heat source per unit length generated in the fluid is extremely high when compared to cases at $2\ m.s^{-1}$ ($7568.8\ W.m^{-1}$).
Figure C-3(c) shows how this heat generation leads to impressive temperature rises, up to $125\ K$ at the center of the contact. Similarly to the shear heat source, there is a horizontal band of very high temperature fluid for $z = h/2$. However, this band is quite wide, with temperature rises reaching $40\ K$ outside of the contact. This is due to the increase in the convection term with the velocity in the energy equation as well as the increase in shear heat dissipation. The temperature difference between the two solids is represented in Figure C-2. The maximum temperature difference is found at $x = \pm 0.91a^{1D}$, which is 1.75 times higher than at $2\ m.s^{-1}$.

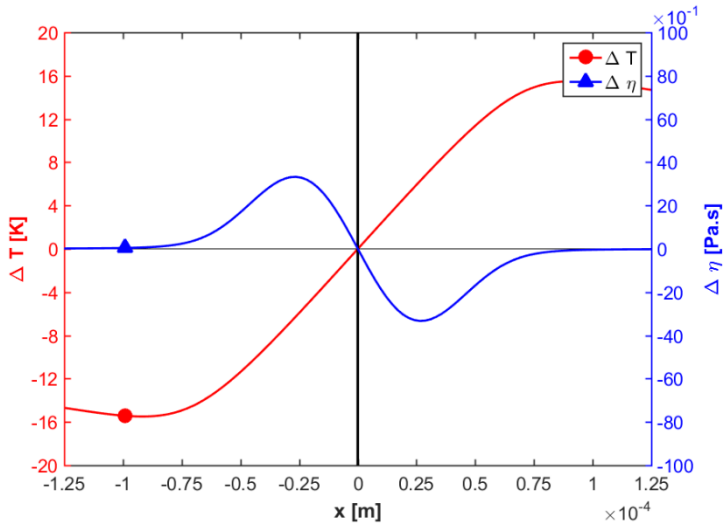

Figure C-2 – Temperature and viscosity differences between the two interfaces at $15\ m.s^{-1}$.

Because of the overall higher temperature, the viscosity is lower at $13\ \mathrm{m.s^{-1}}$ when compared to the results in section 3.1, as seen in Figure C-3(d). The viscosity differences are represented in Figure C-2. In it, the absolute differences of viscosity are quite low. However, the relative viscosity differences extend further away from the center with a maximum found at $x = \pm 0.29a^{1D}$, which is 2.71 times higher than at $2\ m.s^{-1}$. The shear stress (Figure C-3(e)) also

shows high vertical variations in a wider region than at $2\,m.s^{-1}$. This explains why the pressure profile is wider for higher velocities.

To summarise, for high enough values of surface velocities under ZEV condition, the maximum temperature and viscosity differences are found so far away from the contact center that the resulting pressure profile becomes wider. As such, the central pressure becomes lower and lower, which ultimately leads to small central displacement and by extension to no dimple.

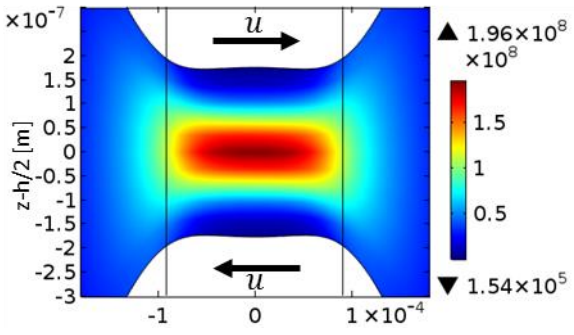

(a) $-\dot{\gamma}\ [s^{-1}]$

Figure C-3 – Profiles of various dependent variables in the contact at $13\ m.s^{-1}$. *(a) Shear rate. (b) Shear heat source. (c) Temperature. (d) Viscosity. (e) Shear stress. The vertical lines mark the location of* a^{1D}.

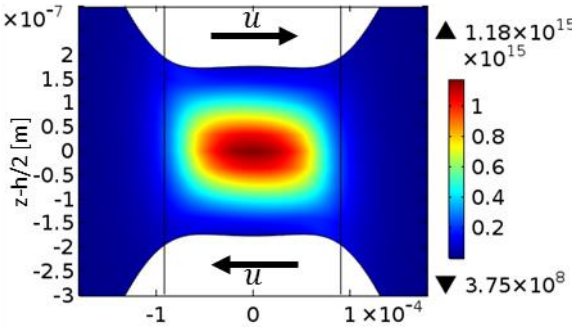

(b) $-Q_s\ [W.m^{-3}]$

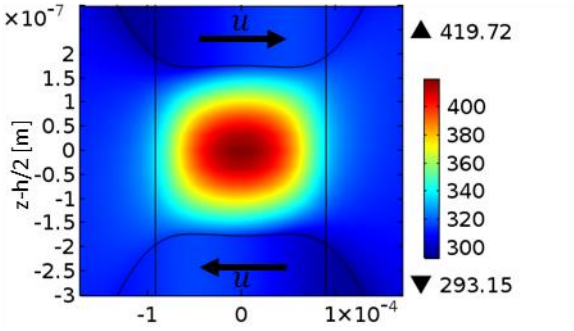

(c) $-T\ [K]$

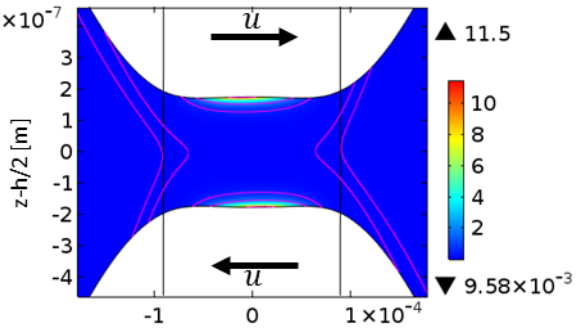

(d) $-\eta\ [Pa.s]$ – Isovalues $\{0.02\ 0.05\ 0.5\ 2\ 10\ 50\ 200\ 1000\}\ Pa.s$

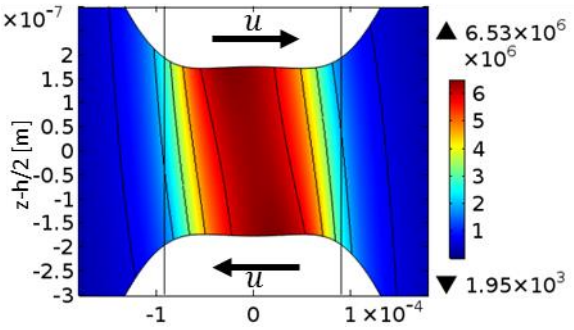

(e) $-\tau_{zx}\ [Pa]$ – 5 Isovalues in black

Appendix D. Local quantities in a low load contact under ZEV condition

In rolling lubrication theory, when very low loads (and contact pressures) are applied, high film thicknesses are observed([4]–[11]). The displacement of the solids may even become negligible before the film thickness, which can put those contacts in the hydrodynamic regime (see Chapter 4). In ZEV condition, the literature on the subject is often restricted to high contact pressures, in which case the film thickness increases with the load. It is interesting to understand what happens in ZEV contacts for low loads.

As such, a calculation was conducted with steel surfaces(Table 2.2-1), the non-Newtonian lubricant defined in Chapter 2, a load per unit width $w^{1D} = 67\ N.m^{-1}$ and a velocity $u = 3\ m.s^{-1}$. This corresponds to the initial state studied in Chapter 4. The corresponding pressure and film thickness profiles are represented in Figure D-1, along with a curve representing the film thickness minus the displacement. As could be expected, the maximum pressure in the contact is very low compared to previous studies, with a value of $0.37\ MPa$. The corresponding central displacement δ is negligible compared to the film thickness.

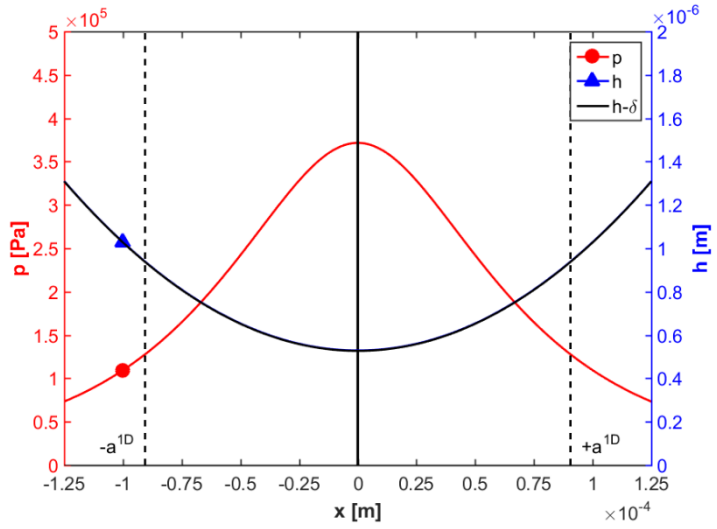

Figure D-1 – Pressure and film thickness profiles at $3\ m.s^{-1}$ and $w^{1D} = 67\ N.m^{-1}$. A complementary curve of the film thickness minus the displacement is also plotted.

In this configuration a small quantity of heat source per unit length ($43.4\ W.m^{-1}$) generated in the contact due to the low load. Therefore, only small variations of the temperature are observed, with a maximum temperature increase of $1.1\ K$. This means that the temperature and viscosity gradients (represented in Figure D-2) between the two contacting bodies have far lower maxima ($0.30\ K$ and $2.8 \times 10^{-4}\ Pa.s$ respectively) than in the cases studied in Chapter 3. The shape of the viscosity difference closely follows the inverse of the shape of the temperature difference. This is an indication that the viscosity is mainly dominated by the temperature, which is not surprising given the extremely low contact pressures. The maximum

for both quantities is found extremely far away from the center of the contact, with the maximum temperature difference and the maximum viscosity difference being found at $x = \pm 1.97 a^{1D}$. The direct consequence is that the pressure generation is extremely wide, which corresponds to the low central pressure.

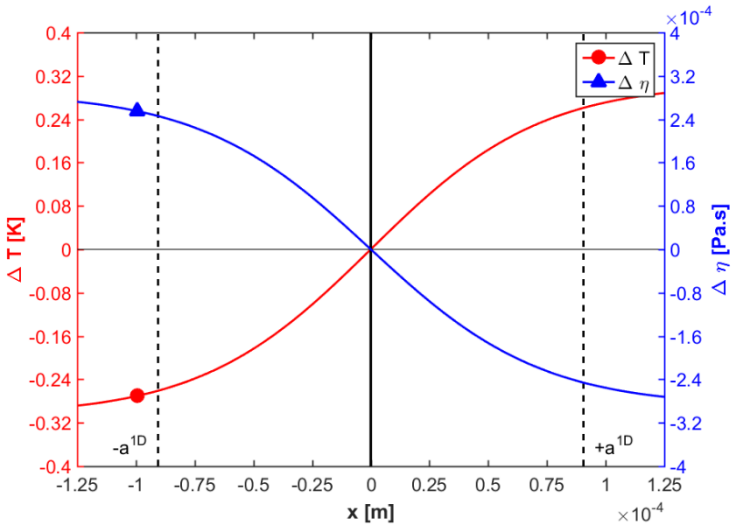

Figure D-2 – Temperature and viscosity differences between the two interfaces at $3\ m.s^{-1}$ *and* $w^{1D} = 67\ N.m^{-1}$.

To conclude, the behaviour of ZEV contact at extremely low loads is reminiscent of the one seen in rolling HL contacts. Small displacements are accompanied by high film thicknesses. However, the existence of temperature differences between the two contacting surfaces is still required to sustain the film, even though the variation of temperature in the fluid is small.

Résumé

Génération d'épaisseurs de films dans les contacts lubrifiés hautement chargés soumis à une condition de Vitesse d'Entrainement Nulle

Les contacts lubrifiés sous forte charge sont souvent étudiés dans des conditions de roulement/glissement. Dans ces cas, l'entrainement du lubrifiant dans un coin d'huile explique la présence d'un film séparateur. Cependant, il existe un certain nombre d'applications dans lesquelles les surfaces en contact ont des vitesses égales et opposées. Cela correspond à une vitesse d'entrainement (définie comme la moyenne des vitesses des deux surfaces) nulle. Dans ce cas, les modèles prédictifs de la littérature ne peuvent plus s'appliquer. Dans ce mémoire de thèse, les phénomènes physiques conduisant à une génération de film séparateur à vitesse d'entrainement nulle sont étudiés. Un modèle éléments finis prenant en compte les aspects thermiques et transitoires est mis en œuvre pour mesurer les quantités locales. En régime stationnaire, les résultats numériques sont comparés avec un très bon accord à un jeu de données issu d'une campagne d'expérimentations dédiée. Cette approche duale permet de quantifier l'influence de la charge, de la vitesse des surfaces et de la température externe sur l'épaisseur de film à vitesse d'entrainement nulle. Les contacts sont ensuite étudiés sous une charge variable, ce qui montre l'influence relative des phénomènes thermiques et transitoires pouvant générer une épaisseur de film. En fonction du ratio entre le temps caractéristique de chargement et le temps caractéristique d'échauffement, ces effets peuvent montrer une synergie bénéfique pour le contact.

Mots-clés : Lubrification TEHD, Vitesse d'Entrainement Nulle, *squeeze*, *viscosity wedge*

Abstract

Film thickness build-up in highly loaded lubricated contacts under Zero Entrainment Velocity condition

Highly loaded lubricated contacts are often studied in rolling/sliding conditions. In those cases, the entrainment of lubricant in a so-called "oil wedge" explains the existence of a separating film thickness. However, in a number of industrial applications, the contact is subjected to opposite surface velocities. In such cases, there is a Zero Entrainment Velocity (defined as the average velocity of the two surfaces) of the fluid. The film thickness prediction formulae developed in the literature for rolling contacts are unusable. In this thesis, the physical phenomena leading to a film build-up under Zero Entrainment Velocity condition are elucidated. A finite element model is used in order to facilitate in-situ measurements. It aims to describe the behaviour of the contact in thermal and transient conditions. In the stationary regime, the numerical values are compared with a very good agreement to a set of results obtained via a tailored experimental campaign. This dual approach enables a quantitative description of the influence of the contact load, surface velocities and external temperature on the film thickness under ZEV condition. Then, the relative influence of the thermal and squeeze effects is studied. Depending on the ratio between the characteristic loading time and the characteristic thermal time, these two effects can show a beneficial synergy for the contact.

Keywords: TEHL, ZEV, Squeeze, Viscosity wedge

FOLIO ADMINISTRATIF

THESE DE L'UNIVERSITE DE LYON OPEREE AU SEIN DE L'INSA LYON

NOM : MEZIANE DATE de SOUTENANCE : 06/02/2020

Prénoms : Bilel

TITRE : Film thickness build-up in highly loaded lubricated contacts under Zero Entrainment Velocity condition

NATURE : Doctorat Numéro d'ordre : 2020LYSEI005

Ecole doctorale : Mécanique, Energétique, Génie Civil, Acoustique (MEGA)

Spécialité : Mécanique

RESUME :

Les contacts lubrifiés sous forte charge sont souvent étudiés dans des conditions de roulement/glissement. Dans ces cas, l'entrainement du lubrifiant dans un coin d'huile explique la présence d'un film séparateur. Cependant, il existe un certain nombre d'applications dans lesquelles les surfaces en contact ont des vitesses égales et opposées. Cela correspond à une vitesse d'entrainement (définie comme la moyenne des vitesses des deux surfaces) nulle. Dans ce cas, les modèles prédictifs de la littérature ne peuvent plus s'appliquer. Dans ce mémoire de thèse, les phénomènes physiques conduisant à une génération de film séparateur à vitesse d'entrainement nulle sont étudiés. Un modèle éléments finis prenant en compte les aspects thermiques et transitoires est mis en œuvre pour mesurer les quantités locales. En régime stationnaire, les résultats numériques sont comparés avec un très bon accord à un jeu de données issu d'une campagne d'expérimentations dédiée. Cette approche duale permet de quantifier l'influence de la charge, de la vitesse des surfaces et de la température externe sur l'épaisseur de film à vitesse d'entrainement nulle. Les contacts sont ensuite étudiés sous une charge variable, ce qui montre l'influence relative des phénomènes thermiques et transitoires pouvant générer une épaisseur de film. En fonction du ratio entre le temps caractéristique de chargement et le temps caractéristique d'échauffement, ces effets peuvent montrer une synergie bénéfique pour le contact.

MOTS-CLÉS : Lubrification TEHD, Vitesse d'Entrainement Nulle, Effet squeeze, Effet viscosity wedge

Laboratoire (s) de recherche : LaMCoS

Directeur de thèse : Nicolas Fillot

Président de jury : Cayer-Barrioz, Juliette

Composition du jury : Seemann, Wolfgang ; Brunetière, Noël ; Morales-Espejel, Guillermo ; Cayer-Barrioz, Juliette ; Fillot, Nicolas ; Raisin, Jonathan